A Comprehensive Study of Vortex Breakdown F1low Mechanisms:

Computational Investigation and Preliminary Control

William Frederick Johnson III

A thesis submitted in partial fulfillment of the

requirements for the degree of

Master of Science in Aeronautics and Astronautics

University of Washington

2004

Program Authorized to Offer Degree:

Department of Aeronautics and Astronautics

	Report Documentation Page		*Form Approved* *OMB No. 0704-0188*

Public reporting burden for the collection of information is estimated to average 1 hour per response, including the time for reviewing instructions, searching existing data sources, gathering and maintaining the data needed, and completing and reviewing the collection of information. Send comments regarding this burden estimate or any other aspect of this collection of information, including suggestions for reducing this burden, to Washington Headquarters Services, Directorate for Information Operations and Reports, 1215 Jefferson Davis Highway, Suite 1204, Arlington VA 22202-4302. Respondents should be aware that notwithstanding any other provision of law, no person shall be subject to a penalty for failing to comply with a collection of information if it does not display a currently valid OMB control number.

1. REPORT DATE **15 MAR 2004**	2. REPORT TYPE **N/A**	3. DATES COVERED **-**

4. TITLE AND SUBTITLE **A Comprehensive Study of Vortex Breakdown F1low Mechanisms: Computational Investigation and Preliminary Control**	5a. CONTRACT NUMBER
	5b. GRANT NUMBER
	5c. PROGRAM ELEMENT NUMBER
6. AUTHOR(S)	5d. PROJECT NUMBER
	5e. TASK NUMBER
	5f. WORK UNIT NUMBER
7. PERFORMING ORGANIZATION NAME(S) AND ADDRESS(ES) **Washington University**	8. PERFORMING ORGANIZATION REPORT NUMBER
9. SPONSORING/MONITORING AGENCY NAME(S) AND ADDRESS(ES)	10. SPONSOR/MONITOR'S ACRONYM(S)
	11. SPONSOR/MONITOR'S REPORT NUMBER(S)

12. DISTRIBUTION/AVAILABILITY STATEMENT **Approved for public release, distribution unlimited**

13. SUPPLEMENTARY NOTES **See also ADM001662., The original document contains color images.**

14. ABSTRACT

15. SUBJECT TERMS

16. SECURITY CLASSIFICATION OF:			17. LIMITATION OF ABSTRACT **UU**	18. NUMBER OF PAGES **169**	19a. NAME OF RESPONSIBLE PERSON
a. REPORT **unclassified**	b. ABSTRACT **unclassified**	c. THIS PAGE **unclassified**			

Standard Form 298 (Rev. 8-98)
Prescribed by ANSI Std Z39-18

University of Washington

Graduate School

This is to certify that I have examined this copy of a master's thesis by

William F. Johnson III

and have found that it is complete and satisfactory in all respects,
and that any and all revisions required by the final
examining committee have been made.

Committee Members:

_____

Mitsuru Kurosaka

_____

Dana Dabiri

Date: _____

In presenting this thesis in partial fulfillment of the requirements for a Master's degree at the University of Washington, I agree that the Library shall make its copies freely available for inspection. I further agree that extensive copying of this thesis is allowable only for scholarly purposes, consistent with "fair use" as prescribed in the U.S. Copyright Law. Any other reproduction for any purposes or by any means shall not be allowed without my written permission.

Signature_____

Date_____

University of Washington

Abstract

A Comprehensive Study of Vortex Breakdown Flow Mechanisms:
Computational Investigation and Preliminary Control

by William F. Johnson III

Chairperson of the Supervisory Committee

Professor Mitsuru Kurosaka
Department of Aeronautics and Astronautics

A modified vortex filament method is used to simulate the evolution of the transient formation of vortex breakdown. The method supports previous studies, illustrating that vortex breakdown is initiated by a negative vorticity gradient which triggers an inviscid self-induction feedback mechanism and when subsequently subjected to viscous effects, results in steady state vortex breakdown. The results of the method are first validated experimentally with numerous past dye flow visualization and particle image velocimetry investigations, and then used to qualitatively investigate the self-induction flow mechanisms during the formative stages of transient breakdown. As a complement to the qualitative investigation, a quantitative analysis is performed, which yields a local and dynamical relationship relating the azimuthal vorticity gradient at a particular location to the curvature of the instantaneous streamline, projected onto the meridional plane, at the same location. This relationship further shows that once radial expansion commences in the region of negative azimuthal vorticity, it continues to expand such that the meridional streamline becomes more curved with time, supporting that the negative vorticity gradient not only initiates the radial expansion, but also, feeds its subsequent growth. On the contrary, in the region of a positive gradient, the streamline continues to flatten fostering radial contraction of the vortex tube, which provides a closure to expansion. In attempt to suppress breakdown in two preliminary control simulations, this positive azimuthal vorticity gradient is then introduced to the

vortex flow just prior to breakdown.   Results from these control simulations illustrated a temporal and spatial delay in breakdown as well as exhibiting flow behavior associated with complete elimination of breakdown.

TABLE OF CONTENTS

LIST OF FIGURES

LIST OF TABLES

ACKNOWLEGEMENTS

DISCLAIMER

1   Introduction

1.1   Introduction to Vortex Flow

Vortex flows are regions of swirling fluid which can occur in any type of medium. Examples of vortex flows are apparent in our everyday lives, from complex weather phenomena, such as violent tornadoes to the simple swirling water pattern formed when draining a sink.   Whether one is driving behind a tractor trailer or piloting a high performance aircraft, one can not escape the presence of these vortex flows.

In the area of aerodynamics, vortex flows are also commonly found emanating from and around aircraft, specifically aircraft marked by large wing sweep and leading edge extensions. Figure 1-1 illustrates an F/A-18 aircraft with a leading edge extension generated vortex while Figure 1-2 illustrates the structure of a similar wing-tip vortex.

Figure 1-1: Vortex flows over F/A-18 (*ref.* 1)

Leading edge vortices such as the one illustrated over the F/A-18 are sources of high-energy, relatively high vorticity flow which generate a strong component of axial velocity along the core of the vortex. The local static pressure, which in general becomes lower

toward the vortex core, is further reduced in the vicinity of the strong axial velocity and near the leading edges.

Figure 1-2: Wingtip generated vortex (*ref.* 2)

This reduction in pressure creates a strong suction on the top surface near the leading edges, enhancing the lift while energizing the flow in the boundary layer to help delay separation. For this reason, the lift coefficient curve for a delta wing exhibits an increase in lift coefficient for angles of attack at which conventional wing configurations would be stalled (*ref.* 3). Unfortunately, this increase in lift performance comes at the price of increased drag and required thrust.

At very large angles of attack, however, these vortex flows experience a dramatic form of flow disruption referred to as vortex breakdown. This phenomenon is characterized by reversal of axial flow and the sudden explosion of the vortex core (*ref.* 4). The breakdown poses severe limitations on the performance of an aircraft due to the sudden degradation in aerodynamic forces and moments.   Moreover, the rapid fluctuations within the turbulent breakdown region can cause buffeting and structural damage through high-cycle fatigue, especially on the empennage structure located immediately downstream of the breakdown region. This effect is prevalent in many aircraft, such as in the case of the F/A-18, seen in Figure 1-1.

Over the past few decades, vortex breakdown has been a subject of rigorous theoretical and experimental study. During this period, a great deal of effort has been spent in the hopes of understanding the flow mechanisms of vortex flow and predicting its occurrence. These efforts have included an assortment of experimental investigation methods such as flow visualization, small-scale model tests in wind tunnels, as well as full-scale aircraft flight tests. In addition to the vast experimental work, a great deal of numerical techniques has also been employed which include an array of grid dependent Euler-base numerical methods and more comprehensive Navier-Stokes code analysis. Despite some progress in predicting the occurrence of vortex breakdown, the aforementioned studies, along with current initiatives, continue to fail to grasp the underlying flow physics of the swirling flow   As a result, a universal and general understanding into the complex flow mechanisms that affect vortex flow and the physical process governing its breakdown still has not been reached (*ref.* 5).

The purpose of this research is to investigate the flow mechanisms which occur in the formative stages of vortex breakdown with the goal of eventually using these associated flow behaviors to employ methods to suppress, delay, or weaken vortex breakdown. This is the first and most crucial step in the over-all effort to eventually suppress the negative effects of vortex breakdown while maintaining and enhancing the positive attributes associated with vortex flow.

1.2   *Vortex Methods*

An alternative to the grid-dependent Euler and Navier-Stokes numerical methods is vortex methods which simulate the fluid flow under an assumption of non-linear dynamics of vorticity (*ref.* 5). In this method, the inviscid motion of vorticity is determined by the local fluid velocity, which in turn is kinematically calculated from the prescribed vorticity field. In addition to the robust and simple nature of vortex methods, another strong benefit of such methods is the ability to simulate the real time dependent build-up of the vortex flow. Unlike the many other numerical methods, the vortex method is able to model the flow from the very beginning and further track the continual

development of the swirling flow in its formative stages, without requiring the initial introduction of prescribed vorticity.

The most promising and robust vortex method is the vortex-filament method. One of the first attempts at utilizing the vortex-filament method to model the phenomenon of vortex breakdown was carried out by Nakamura, Leonard, & Spalart (*ref.* 6). In the current investigation a modified version of the vortex-filament method initially developed by Cain (*ref.* 7) will be used to simulate the complex vortex flow.

Cain's vortex filament method allows one to look at the temporal evolution of the transient formation of vortex breakdown with the use of the Biot-Savart law to calculate the motion of fluid. The Biot-Savart law is based on the induced velocities associated with a specified vorticity distribution. Therefore, if the law is modified such that it includes only the induced velocity profile of the vortex core and the effects of vortex stretching, we can limit the governing mechanisms of the vortex flow to those parameters associated specifically with induced velocities, the vortex core velocity profile, and vortex stretching. With this in mind, let us now explain how the filament method is employed to model a vortex tube.

1.3   Cain's Vortex Filament Method

Although modifications will be made to Cain's original vortex filament method, the discretization and initialization process of the modeled vortex tube will remain unchanged. Therefore, in order to aid in the discussion in the following chapters, a quick overview of the vortex filament method is necessary. For a complete and detailed explanation of the method, please refer to Cain (*ref.* 7)

1.3.1   Brief method overview

A vortex tube is composed of many vortex lines. These vortex lines are always aligned with the vorticity vector associated with the fluid motion, as seen below in Figure 1-3. In essence these vortex lines are nothing more than the simple vortex filaments which will be used in the simulation.
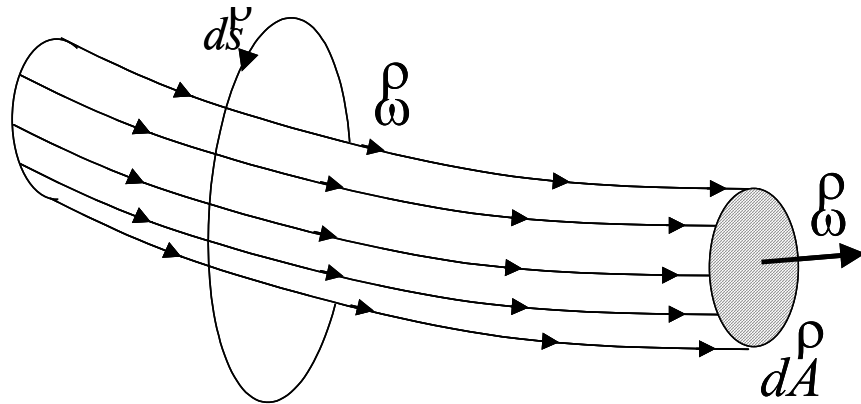
Figure 1-3: Vortex tube (*ref.* 7)

Using the Biot-Savart law, one can calculate the velocity induced by the vorticity of one vortex line on another nearby vortex line. In doing such, we can determine the movement of the vortex lines relative to each other. Helmhotz vortex theorem states that the vorticity associated with a fluid will move with the fluid line. Therefore, as induced velocities cause movement in the fluid elements, they likewise cause movement in the associated vorticity elements. With this idea in mind, we can calculate the induced velocities of the vortex lines at a given time, multiply those velocities by the time step, and ultimately calculate the movement of the vortex lines relative to each other. Repeating this process at every time step offers us the ability to track the temporal evolution of the vortex lines.   Therefore, by representing a real vortex tube with a group of vortex lines, prescribed with a given vorticity distribution, the vortex filament method can model the motion of a real vortex.

1.3.2   *Discretizing the vortex tube*

To use the vortex filament method, we need to discretize a vortex tube into an appropriate number of vortex filaments. In order to appropriately discretize the simulated vortex tube, the vortex lines are prescribed such that their sum occupy the same cross sectional area as the vortex tube. Each vortex line, at a given vortex line radius, is assigned the same Gaussian distribution of vorticity, similar to that of the overall vorticity value of the tube. These lines are then packed densely enough to assure that there is no empty space inside the discretized tube. Additionally, in order to maintain a smooth

distribution of vorticity within the tube, the cross-section of vortex lines overlaps. A
sketch of the discretized vortex tube is illustrated in Figure 1-4.
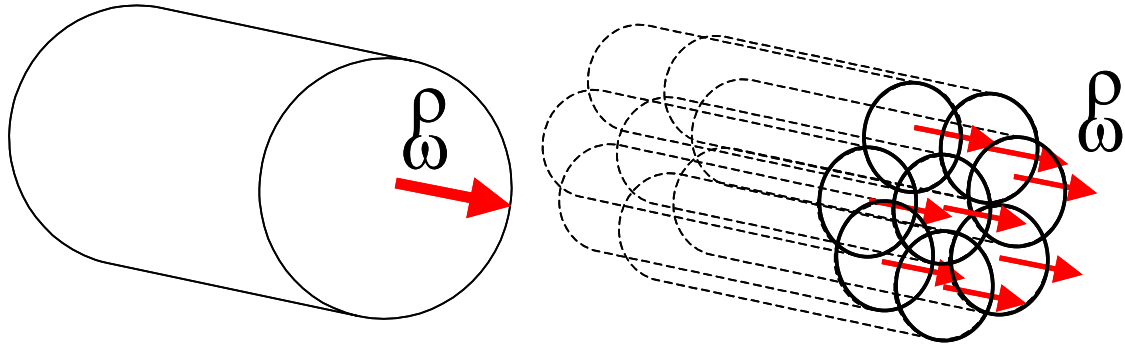
Figure 1-4: Vortex tube discretization (*ref.* 7)

Now that the vortex tube is discretized into many overlapping vortex lines, it is
further discretized individually along those lines. To do this, the vortex lines are broken
up into smaller vortex filament segments, illustrated below in Figure 1-5.
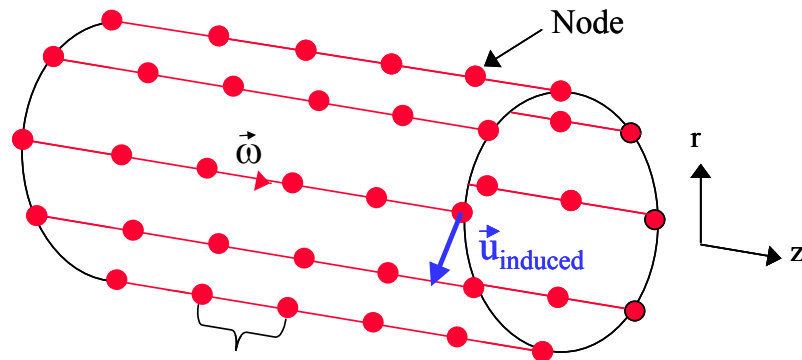
Figure 1-5: Vortex filament segments (*ref.* 7)

The endpoints of each vortex filament segment are referred to as nodes and mark the
location at which the induced velocity associated with each respective filament is
calculated. In short, the movement of the filaments is modeled by tracking the temporal
evolution of nodal position.

The simulated tube is discretized into nine concentric cylinders. These cylinders
have radii of 0.42, 0.36, 0.30, 0.24, 0.18, 0.12, 0.08, 0.06 and 0.03. Each cylinder is then
further discretized into sixteen vortex filaments, which are even spaced along the

circumference of the cylinder. Additionally, a tracking filament is also specified along the centerline of the vortex tube, r=0, which contains no vorticity.

1.3.3   Initializing the vortex tube

Once the vortex tubes are specified in the radial direction, the next step is to initialize them in the axial direction. In this step, the starting axial location of all vortex filament segments is defined by specifying the endpoint node locations of each filament segment. For this investigation, the initial axial filament length of 0.1 was chosen. Therefore, at a given radius, all the nodes are equally spaced axially along the vortex centerline at a value of dz=0.1.

After the initial location of the vortex filaments has been specified and given a core radius, vorticity is then assigned to each vortex filament segment. Each individual vortex filament segment is assigned a vorticity value by prescribing to each segment a value of circulation, $\Gamma_{i,j}$, such that the total circulation of all of the concentric cylinders at an axial location is equal to the total circulation value of the vortex tube, at that same axial location.

Since vorticity remains constant along a vortex line, each vortex filament along a specified radius will have the same value of vorticity. On the contrary, the vorticity distribution among differing radii will be assigned such to match that of an ideal vortex created by unbounded swirling flow. The circumferential velocity and the axial vorticity of this ideal flow are defined by Equations (1-1) and (1-2) respectively.

$$u_\theta = \frac{C\left(1 - e^{-br^2}\right)}{2\pi r} \qquad (1\text{-}1)$$

$$\omega_z = \frac{1}{r}\frac{d}{dr}\left(r \cdot u_\theta\right) = \frac{C \cdot b \cdot e^{-br^2}}{\pi} \qquad (1\text{-}2)$$

To match experimental data, Cain choose a value of $b = 10.9$. In the above equations C is defined as the total circulation value at a given axial location and is the sum of the circulation, $\Gamma_{i,j}$. Figure 1-6 shows the circulation in each concentric ring of filaments as well as the total circulation of the discretized vortex tube.

Total Vortex Circulation: Ideal Verses Discretized Case
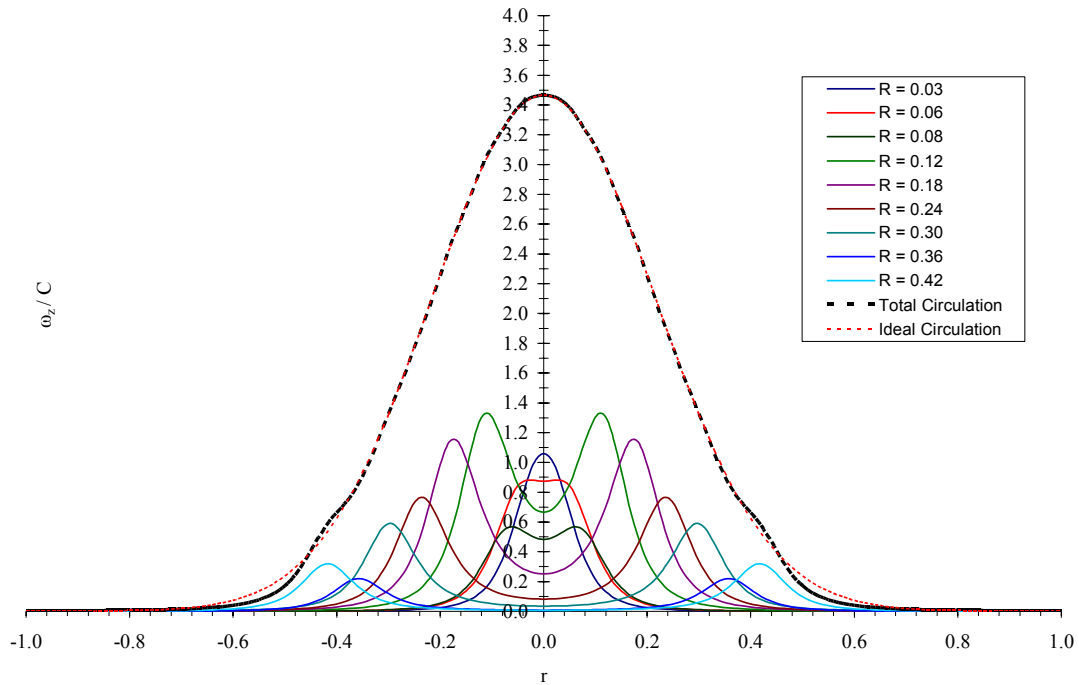
Figure 1-6: Ideal vs. discretized circulation

The series of small amplitude colored lines illustrates the sum of the circulation from the
sixteen vortex filaments in each of the nine concentric rings. The sum of circulation of
all vortex filaments (all nine rings) within the vortex tube is represented by the dashed
black line, and is further compared to the total circulation distribution of the ideal case,
shown by the dashed red line. From the data offered in Figure 1-6, a Gaussian
distribution can be obtained to approximate the distribution of vorticity in each vortex
filament core. This approximation is denoted by Equation (1-3).

$$C \cdot \omega_j = C \cdot \overline{\Gamma}_j \frac{2 \alpha \sigma_j r_j \left(r_j^2 + r^2 + \alpha \sigma_j^2 \right)}{\left\{ \left(r_j + r \right)^2 + \alpha \sigma_j^2 \right] \left[\left(r_j - r \right)^2 + \alpha \sigma_j^2 \right\}^{3/2}} , \text{ for } j = 1 \text{ to } 9 \qquad (1\text{-}3)$$

In Equation (1-3) the j subscripted values refer to the value of the quantities for an entire
concentric ring. To best match a Gaussian distribution, we choose $\alpha = 0.413$.   More
specifically, $C \cdot \overline{\Gamma}_j$ is the circulation in the entire j^{th} ring of vortex filaments, and since

each concentric ring is made up of sixteen filaments, the circulation of an individual

filament in that ring is $\dfrac{2\pi \cdot C \cdot \overline{\Gamma}_j}{16}$.

1.3.4   Prescribed Vorticity Gradient

In his investigation of transient vortex breakdown, Cain concluded that vortex breakdown was brought about through a self-induction caused by a negative vorticity gradient in the vortex core. With the use of his vortex filament method, he showed that this negative vorticity gradient, with azimuthal vorticity in the vortex tube increasing in the upstream direction, was an important initiator of the vortex breakdown mechanism.   For this reason, we also want to highlight this negative vorticity gradient in our model and will do so by causing a change in circulation in the vortex tube. In order to create this negative vorticity gradient case (vorticity in the vortex tube increasing upstream), the circulation profile in the vortex tube coming out of the vorticity source as a function of time will be linearly increased from an initial and minimum value to a final and maximum value.

1.3.5   General Algorithm

Figure 1-7 shows a brief flow chart outlining the general algorithm of the vortex filament model.   The complete and modified simulation code, written in C++ is located in Appendix D.

Initialize simulation
- *Specify vortex filament locations*
- *Initialize vortex filaments core radius*
- *Assign vorticity to each filament*

Main program loop

Output
- *vortex filament location*
- *vortex filament core radius*
- *vorticity of vortex filament*

Calculate node velocity

Filament location z > 0?

$t = t + \Delta t$

Update vortex filament core radius

$$\vec{r}_{node}(t + \Delta t) = \vec{r}_{node}(t) + \vec{u}_{node,total} \cdot \Delta t$$

Update vortex filament node location

no

$$\vec{u}_{total,node} = U_\infty \vec{e}_z$$

yes

Calculate $\vec{u}_{induced,node}$

$$\vec{u}_{total,node} = \vec{u}_{induced,node} + U_\infty \vec{e}_z$$

Figure 1-7: General algorithm (*ref.* 7)

2   Preliminary Modifications

The self-induction theory of vortex breakdown and the vortex filament method, offered by Cain (*ref.* 7), have given much insight into the formative stages of transient vortex breakdown. However, in attempt to better model the flow conditions of axisymmetric spiraling flow and the many features of vortex breakdown, additional modifications must be made to Cain's original code. This section will present these modifications as well as the justification and/or rationale for their employment.

2.1   *Upstream Boundary Conditions*

One major difficulty with any numerical simulation lies in specifying and matching appropriate boundary conditions within the numerical domain.   These difficulties have been well documented and the past works of Nakamura et al (*ref.* 6), Leonard (*ref.* 8), and Garbowski & Berger (*ref.* 9) have offered guidance for many subsequent numerical methods.

In Cain's simulation, all flow properties along the boundary of the flow domain, with the exception of axial vorticity at the vorticity source, are set to a zero value. Such conditions are reasonable for the radial boundaries conditions, provided that the boundaries are a significant distance away from vortex core. Computational studies by Brown & Lopez (*ref.* 10) and experimental studies by Harvey (*ref.* 11) concluded that a radial boundary should be placed at a radius of at least two core diameters from the center of the vortex (centerline).   In Cain's simulation, this boundary is approximately four vortex core radii from the centerline and therefore, appropriate. The downstream boundary condition, similar to the radial boundary, is also reasonable so long as the boundary is located well downstream of the transient vortex filaments and their respective induced velocity effect. However, the upstream boundary condition, in this case the $z = 0$ wall, is critical in calculating the velocity and vorticity fields within the flow domain. Cain elected to set all induced flow properties at the wall to zero. This condition is unsatisfactory because the filaments have very distinct non-zero velocities when emerging from the wall. As a result, the effect of this boundary condition taints the interpolated velocity and vorticity fields of the domain near the upstream wall position.

This inaccuracy is clearly visible in Cain's vorticity field plots, shown in Figure2-1 and Figure 2-2.
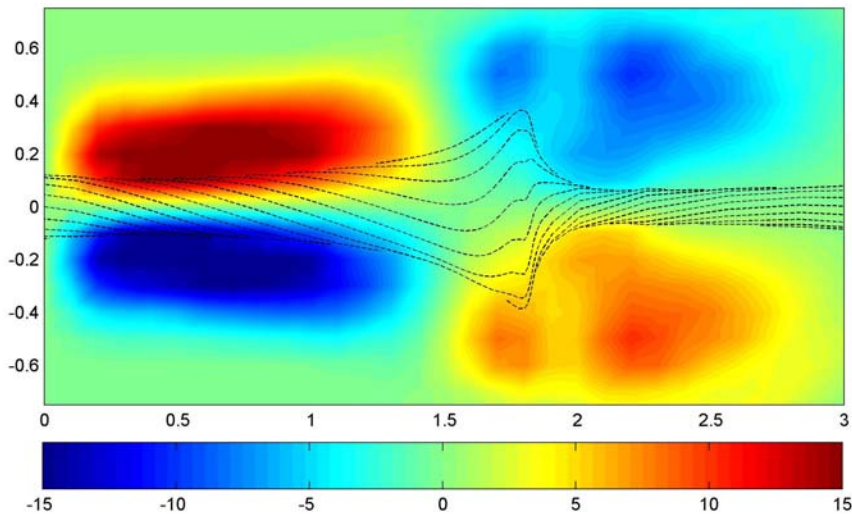
Figure 2-1: Azimuthal vorticity sign switch, meridional plane, T = 1.2 (*ref. 7*)

Figure 2-1 illustrates the azimuthal vorticity field of the domain. Notice that all along the upstream boundary, z = 0, the azimuthal vorticity is zero. As previously mentioned, this inaccurate condition is the cause of the discontinuity in the flow field aft of the upstream boundary, z=0. This inaccuracy is also illustrated in the axial vorticity plot, shown in Figure 2-2. At the time shown above the maximum circulation value has been reach and thus the vorticity field immediately aft of the wall should be constant with time (not radius) and clearly non-zero.
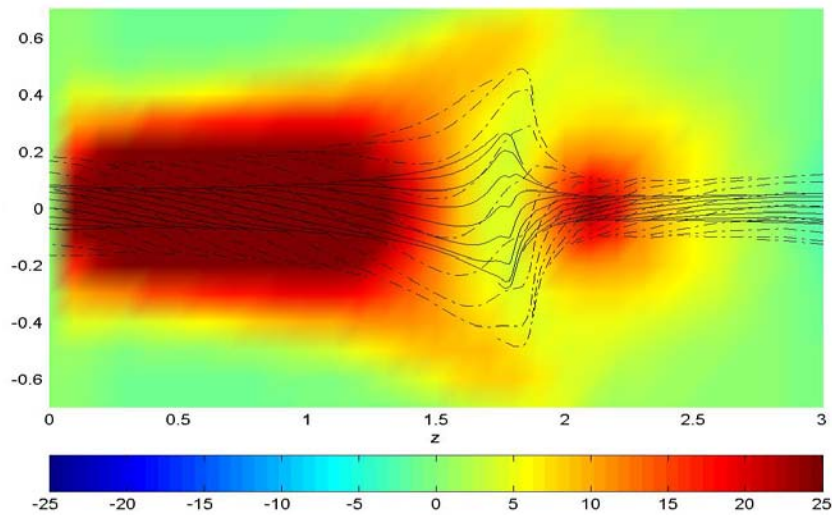
Figure 2-2: Axial vorticity, meridional plane, T = 1.2 (*ref. 7*)

If the individual properties values are not calculated at the upstream boundary condition, as in Cain's case, three such options exist to correct the inaccurate region, referred to as Region II. The first would require placing the upstream boundary at some location downstream of the z=0. This method was initially utilized by Nakamura et al. (*ref.* 6) in their past numerical simulations. However, Brown & Lopez (*ref.* 10) is quick to point out that doing such requires the assumption that the flow at the upstream boundary is locally independent of the rest of the flow field throughout the evolution of the swirling flow. Clearly this does not hold true, since the flow field in this region varies during the circulation and velocity ramp-up. The second option would be to remove or 'crop' the inaccurate portion of the flow field from the data range. This investigation, however, is interested in the eventual control of vortex breakdown within the flow. These controls may include the 'near-wall' flow, which may be nestled within Region II. If this investigation were concerned with only the far downstream structure of the vortex, this crop option would be suitable.

The third option, the new modified numerical simulation allows for the calculations of the wall property values as a function of time; specifically those of the azimuthal component of vorticity. Therefore the inaccurate region can be eliminated by applying the values directly to wall boundary condition at each time step. Velocity properties at the wall can be extrapolated directly from the data, but the vorticity properties, in general, and the azimuthal vorticity data at the upstream boundary in particular, requires additional calculations.

The Helmhotz vortex theorem states that the vorticity moves with the motion of a material fluid line. This asserts that as the induced velocities trigger the fluid elements to move, they additionally move the vorticity associated with the fluid elements. This does not mean, however, that the vorticity vector and velocity vector are necessarily aligned.
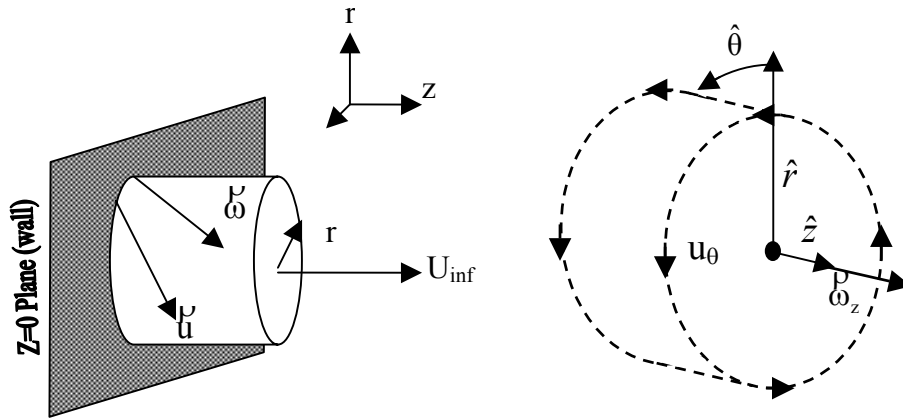
Figure 2-3: Vortex tube orientation

The velocity and vorticity vectors can be decomposed into components and the angles between the respective vector components can be calculated. These angles, Φ_u and Φ_ω, referred to as the helical angles of the velocity and vorticity, respectively, are shown in Figure 2-4.
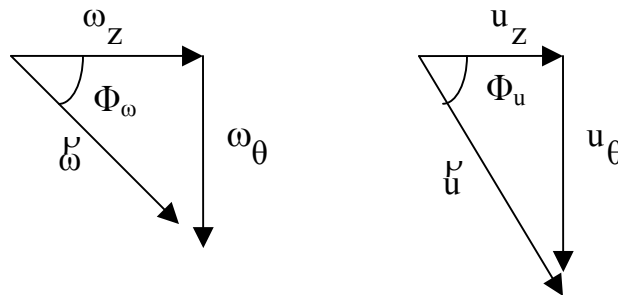
Figure 2-4: Velocity and vorticity vector components

To be consistent with past studies, this investigation will utilize the α_o and β_o parameters, proposed by Brown & Lopez (*ref.* 10). These parameters are the tangents of the helix angle for the velocity and vorticity, respectively. The values of α and β are related to Φ_u and Φ_w by

$$\alpha_0 = \tan(\Phi_u) = \frac{u_{\theta_0}}{u_{Z_0}} \tag{2-1}$$

$$\beta_0 = \tan(\Phi_w) = \frac{\varpi_{\theta_0}}{\varpi_{Z_0}} \tag{2-2}$$

We can solve for the tangent of the helical angle of velocity at the wall, α_o, using the Equation (2-3). Note that α_o is only a function of time and radial position.

$$\alpha_o = \tan(\Phi_u) = \frac{u_{\theta_0}}{u_{Z_0}} = \frac{C(t, r, z = 0)}{U(t) \cdot 2\pi r} \tag{2-3}$$

where, C is the sum of all circulation contained within the jth concentric ring of vortex filaments and U(t) is simply the free stream velocity. As previously mentioned the total circulation of the vortex tube is discretized into nine (9) concentric rings, each composed of 16 filaments, using a Gaussian distribution. Therefore, the total circulation within the jth ring is simply the sum of all the distribution constants, Γ_i, multiplied by the total circulation, C_∞.

$$C(t, r_j, z = 0) = \sum_{j=1}^{j} 2\pi r_j C_\infty \Gamma_j \tag{2-4}$$

Similarly, since we are modeling the case of unbounded swirling flow, the axial vorticity at z=0 is defined by Equation (2-5).

$$\omega_z = \frac{C_\infty \cdot b \cdot e^{-br^2}}{\pi} \tag{2-5}$$

To match experimental data, we again choose $b = 10.9$ (*ref. 7*). C_∞ is specified, as it is the total circulation at a given axial location.

Stream surface studies by Brown & Lopez (*ref.* 10) have shown that in order to produce a negative azimuthal vorticity gradient, the ratio of α_o to β_o must be greater than one. Since the essential feature of vortex breakdown is the generation of negative azimuthal vorticity, a ratio greater than one must be used; in this case $\frac{\alpha_o}{\beta_o}$ of 1.5 is chosen.

Given the above expression for the axial vorticity at the boundary condition, $\omega_{z,}$ from (2-5), α_o from (2-3), and the proportional relationship between α_o and β_o, the following expression for the azimuthal vorticity at the wall can be determined.

$$\omega_\theta = \frac{\beta_o}{\alpha_o}\, \alpha_o\, \omega_z \qquad\qquad (2\text{-}6)$$

The azimuthal vorticity is a function of both time and radius. Therefore, the upstream boundary conditions vary depending on the radial distance from the vortex core, as well as in time. Figure (2-5) shows the velocity and vorticity distribution along the modified vorticity source as a function of the radial distance from the centerline. Similarly, Figure 2-6 shows the "jet-like" axial velocity profile of the upstream boundary condition as a function of time.
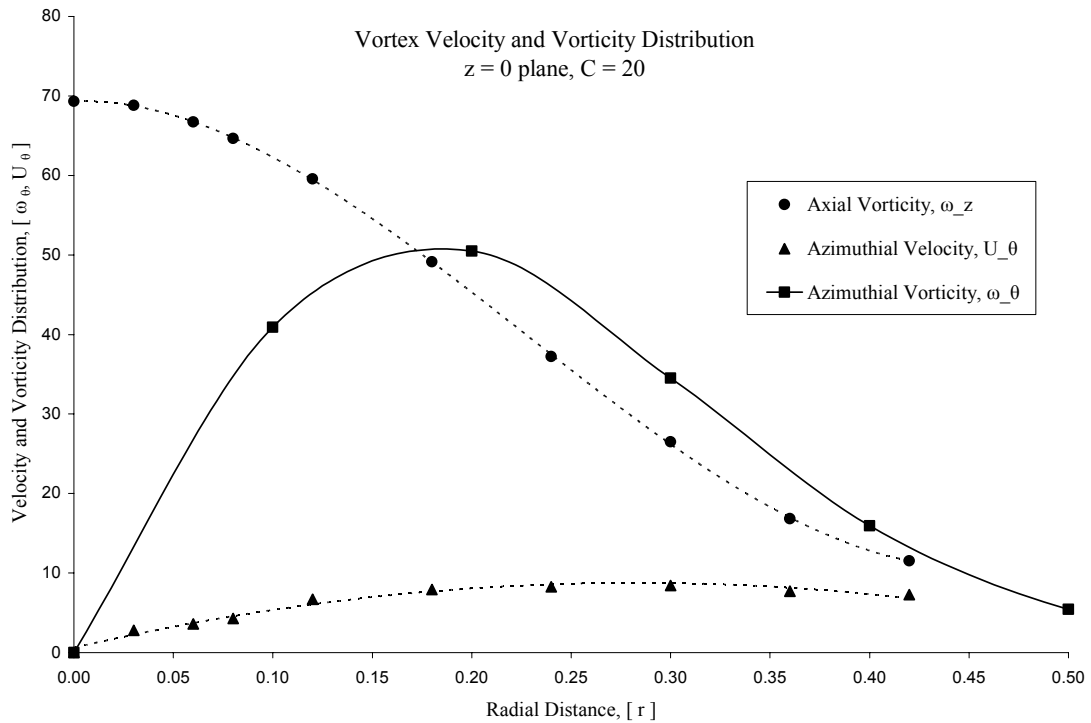
Figure 2-5: Vortex velocity and vorticity distribution at z = 0

Figure (2-5) gives insight into the solid body and irrotational regions of the vortex. As with all real vortices, the boundary between the solid body region and irrotational region occurs at the radius of maximum azimuthal velocity. This radius location is said to be the edge of the vortex core. Similar to Cain's simulation, the modified simulation has a core radius size of 0.30.

Axial Velocity as a Function of Radial Distance
Along z = 0 Plane
$\tau = 0.2$ sec $C_{max} = 20$ $U_{max} = 5$
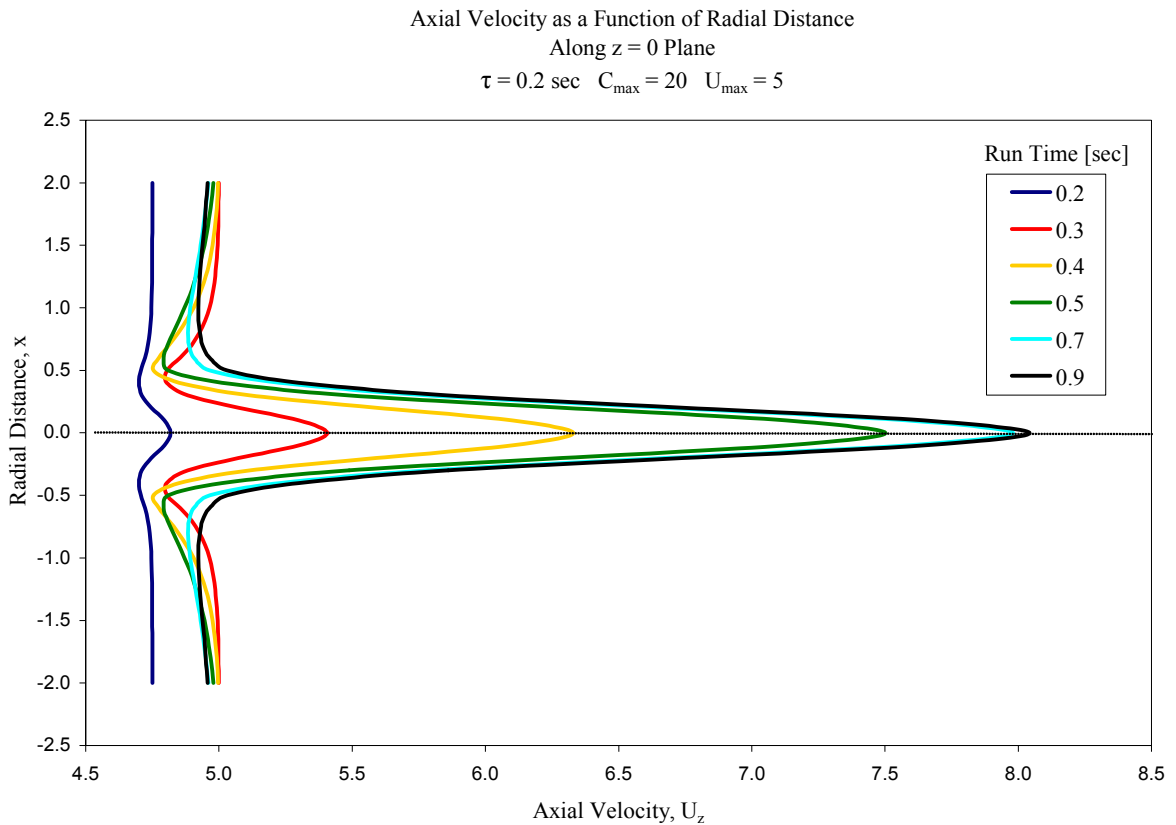
Figure 2-6: Axial velocity profile as a function of time at z = 0

Figure 2-6 illustrates the development of "jet-like" axial velocity profile at the upstream boundary condition, offered by the modified simulation. At T=0.9 the profile is established, with an axial velocity at the center of the vortex core of almost twice the freestream value. It is important to note that steady vortex breakdown LDA experiments by Escudier (*ref.* 12) and Faler & Leibovich (*ref.* 13) have demonstrated that the axial jet profile is already well established upstream prior to breakdown. However, since the simulation models transient vortex flow, a period of time is required in order to fully develop this profile.

In theory, the boundary conditions would constitute a continuous function. However, in order to implement these conditions, numerically, the values are discretized radially along the boundary such that the values align geometrically with the outputted flow domain data.   The benefit of such alignment is that no additional modifications to

the interpolation subroutines, structured within the numerical code, are needed. An example of this alignment is demonstrated in Figure 2-7.
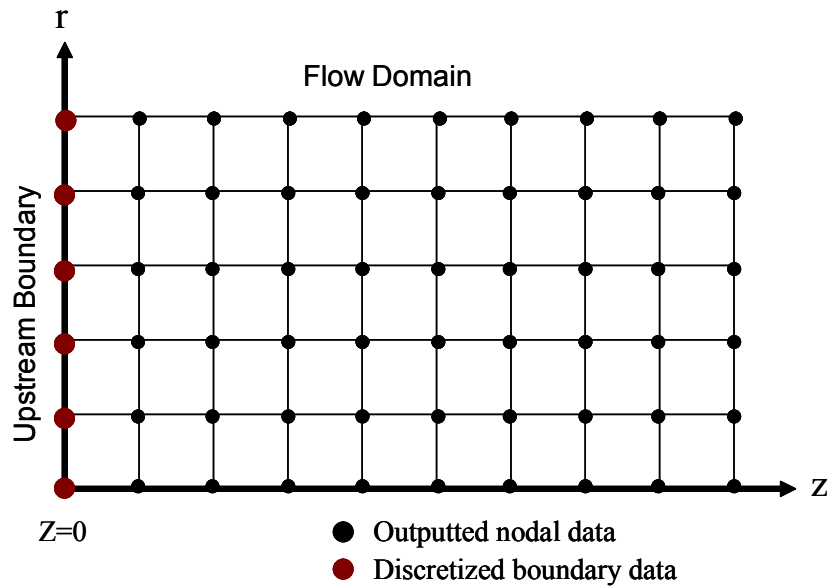
Figure 2-7: Alignment of upstream boundary discretized conditions

The hope is that the ability to better capture the flow immediately aft of the vorticity source will not only offer further insight into the flow mechanisms but will present a more accurate numerical model.

2.2   *Convective Velocity Pitch-Up*

The second modification to Cain's original code is the introduction of a non-constant, time dependent convective velocity profile. This convective velocity is defined as the velocity at which the fluid mass is advected through the domain and does not include induced velocity. Cain's original code fixed the axial velocity, at which the filaments emerged from the vorticity source and moved downstream, to a constant value. Simple dimensional analysis can show that circulation is simply a function of angle of attack (or vane angle), velocity, and an appropriate length scale, whether chord length or radius of the vortex core. If, in transient test, the angle of attack and length scale are held constant, such as in delta wing or bounded pipe flow investigations, circulation then becomes only a function of velocity. With this in mind, the goal is to model the

convective velocity proportionally with that of the established 'pitch up and hold' circulation profile.

A preliminary attempt to alter Cain's constant free-stream velocity was performed by Wimer (*ref.* 14). Wimer introduced a spatially decreasing convective velocity profile in hopes of modeling the velocity profile associated with vortex breakdown over a delta wing. The axial fluid velocity over a delta wing reaches a maximum near the vorticity source and soon then rapidly falls towards the trailing edge. However, Wimer was quick to point out that this measured axial profile over such a delta wing is a result of steady state condition, a condition that Cain was not able to achieve. Additionally, he notes the difficultly and uncertainty in separating the convection velocity component caused by the pressure gradient from the vortex induced velocity. Despite these concerns, he enabled the filaments at the vorticity source to convect at a high velocity and then slow down with increasing z-position.

Unlike Wimer's spatially dependent convective velocity profile, the present modification prescribes the convective velocity as a function of time, which enables the convective and induced velocities to remain separate. Under this condition, all flow within the domain at a given time step is assigned the same convective velocity. A qualitative representation of this condition is illustrated in Figure (2-5). This condition maintains continuity and better models the flow behavior of bounded spiraling flow, such as in the case of pipe flow (*ref.* 12).
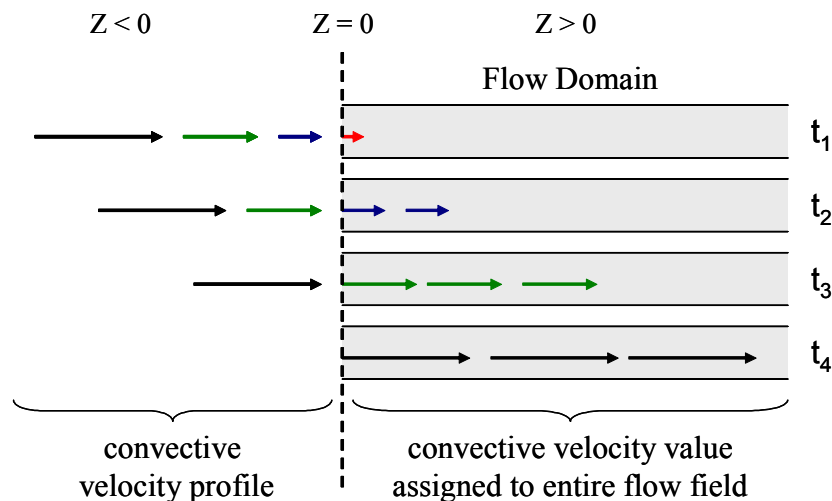
Figure 2-8: Convective velocity assignment to flow field

Owing to the aforementioned proportional relationship between velocity and circulation, a baseline velocity profile similar to the circulation profile was chosen, which can be seen in Figure (2-6). Some experimentation was done in arriving at the present proportional constant of one-fourth (¼). In keeping with Cain's color designation scheme, this investigation will continue to use the color red to indicate a region of changing circulation.
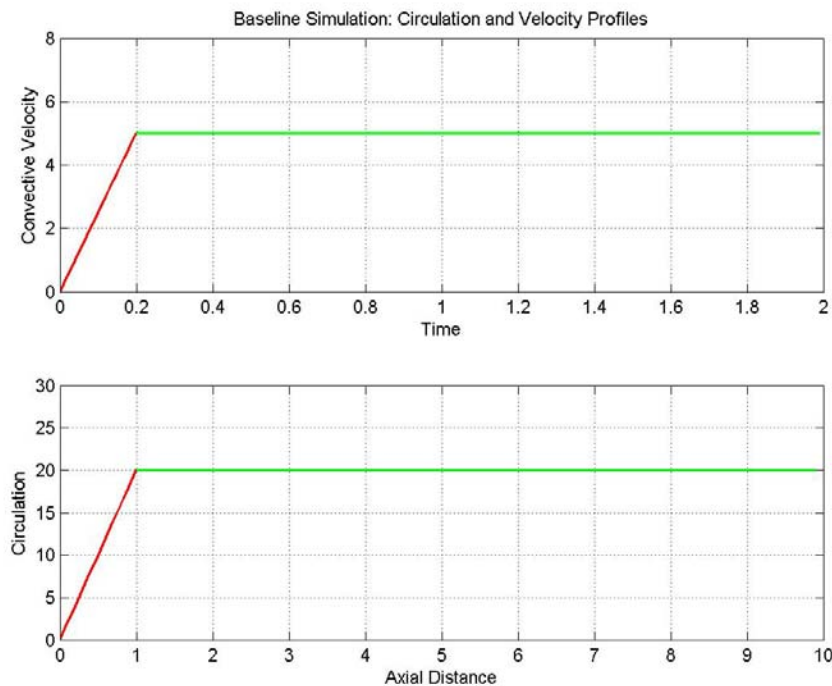
Figure 2-9: Baseline simulation: circulation and velocity profiles

2.3 Induction Turn-off Zone

Another modification made to Cain's original simulation is the creation of an induction switch off zone. For reasons which will be further explained later in this investigation, this switch allows for the induction on the vortex filaments within a specified region ,immediately aft of the vorticity source, to be turned off. This turn-off means that the entering filaments no longer receive any induced velocities from the other filaments in the flow, but merely convect downstream according to the current convective

velocity. These filaments, however, do continue to induce velocities on all remaining filaments downstream of the turn-off region. As the simulation progresses and new filaments are emitted from the source, they too are turned off as well. Under this condition, the turned-off filaments come out of the vorticity source axially aligned and continue to stay straight until they leave the induction turn-off region. The size of this turn-off region is variable and user specified. This switch also sets the stage for forced filament bending. In this case, the filaments in this region are set to a user-defined tilt or helical angle. This scenario will be later employed.

2.4   Removal of Blue Region

Cain's original simulation divides the vortex tube into three regions – green, blue and red. The green shaded filaments indicate regions of the high, final circulation. The blue region indicates the area of low circulation whereas the red region indicates the area that circulation is increasing. However, preliminary studies by Cain (2001), and later studies performed by Wimer, showed that the formative features of breakdown, including the turning point, stagnation point, and azimuthal vorticity sign switch location, occur in the red and green regions only. These mechanisms are not influenced by nor affected by the nature of the blue region. Therefore, in order to reduce computational run-time and ease memory storage requirements, the blue region of constant low circulation is removed. As a result, the linear velocity and circulation pitch-up begins immediately at the start of the simulation.

2.5   Variable Pitch-Up Time

One of the key features studied in this investigation is the effect of the velocity and circulation ramp-up time on the formative features and locations of breakdown. In order to do such, the simulation was modified to allow for varying ramp-up time values.

3   Simulation Overview & Results

        Having modified the vortex-filament method simulation, this section will present results in both qualitative and quantitative form. Furthermore, the improvements and differences from the findings offered by Cain (*ref.* 7) will be addressed.   A discussion of the simulation results is also presented along with how the new findings provide further evidence for the inviscid mechanism of the self-induction theory of vortex breakdown. Finally, this section will also offer proof that the modified simulation better represents actual vortex flow by comparing the results with past swirling flow experiments.

3.1   Vortex Streakline Representation

        The solid surface rendition will be presented first and compared with Cain's results. In these results, such as the example in Figure 3-1, the vortex lines starting initially as are rendered as surfaces in order to create a solid shape rather than a tangled assortment of all the vortex filaments, seen in Figure 3-2.   These vortex lines are, in fact, streaklines in that they represent the many vortex filaments segments released successively from the fixed vorticty source, at one instant in time. Since these vortex filaments segments are comparable to fluid particles, this representation offers a valid comparison to dye streaks used in past flow visualization experiments.
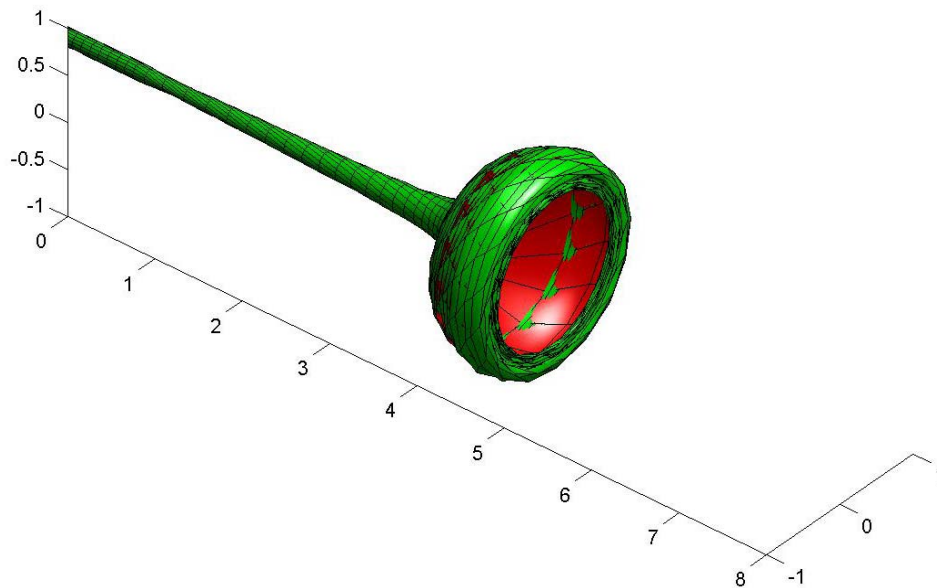
Figure 3-1: Solid representation, r = 0.08, perspective view

Streaklines, Tau : 0.20, Time : 1.75
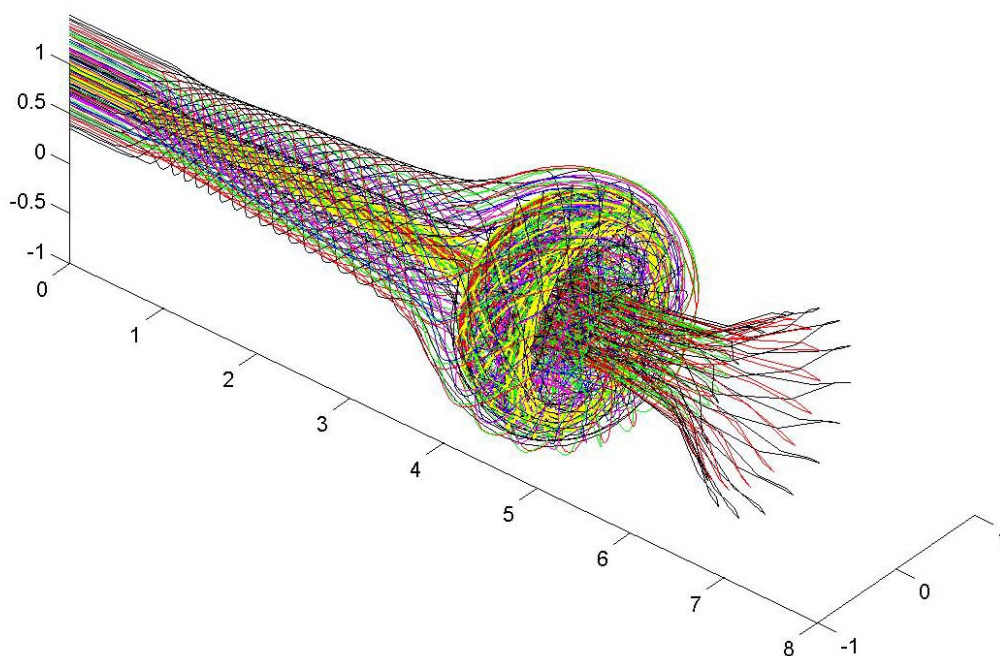
Figure 3-2: All vortex filaments, perspective view

The only slight shortcoming in the solid representation is that only one of the six radii can be shown at one particular time. This restraint, however, is comparable to flow visualization, in that the dye gets entrained into, and remains in, a single radial layer of the vortex as it moves with the fluid. In comparison, this minor shortcoming is a small price to pay for the many additional intrinsic benefits in visualizing the vortex filaments.

As pointed out by Cain (ref 7), one such benefit to the vortex filament method is the ability to infer induced velocities by simply looking at the vortex filaments orientation relative to each other. Since the vorticity vector is aligned with the vortex filaments, the induced velocity from any one particular filament on the flow field can be determined using the right hand rule. This principle benefit affords insight into the formative stages of vortex breakdown which many past numerical simulation techniques could not offer.

Three different sets of the modified simulation results are plotted. The parameters of the baseline simulation are shown in Table 3-1.   The first set, shown in Figure 3-3,

shows the solid representation of the vortex from a side view. The vortex filaments in this figure emerge from the vorticity source at r = 0.24.

Table 3-1: Baseline simulation parameters

Parameter	Value	Units
Initial filament length, Δz	0.1	[length]
Simulation time step, Δt	0.01	[time]
$C_{initial}$	0.0	$[length]^2$ / [time]
C_{final}	20	$[length]^2$ / [time]
$U_{initial}$	0.0	[length] / [time]
U_{final}	5	[length] / [time]
$\tau_{velocity}$	0.20	[time]
$\tau_{circulation}$	0.20	[time]

Figure 3-3 also shows the associated radial spokes. These radial spokes occur in the region of changing circulation and are needed in order to adhere to the third part of the Helmholtz theorem, which requires the emergence of radial vorticity to satisfy the solenoidal property. Refer to Cain (*ref.* 7) for a more detailed explanation. As the radial spokes emerge from the vorticity source, they are branched off with circulation equal to ΔC and then sent all the way far-field. Although the branches emerge from the vorticity source straight, subsequently they do not remain purely in the radial direction due to mutual induction. For simplicity, the results are presented in time intervals of t = 0.25.
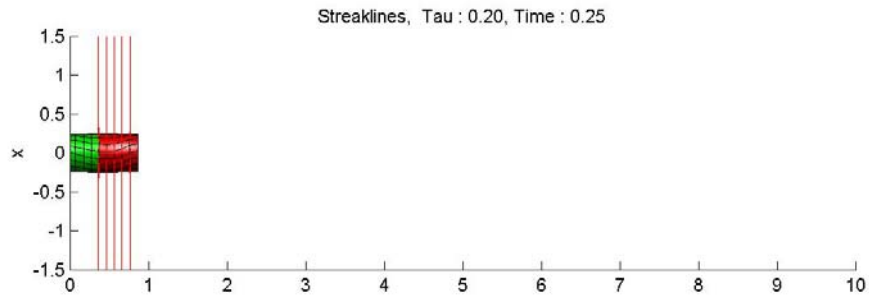
Figure 3-3: Modified simulation results with radial spokes, r = 0.24
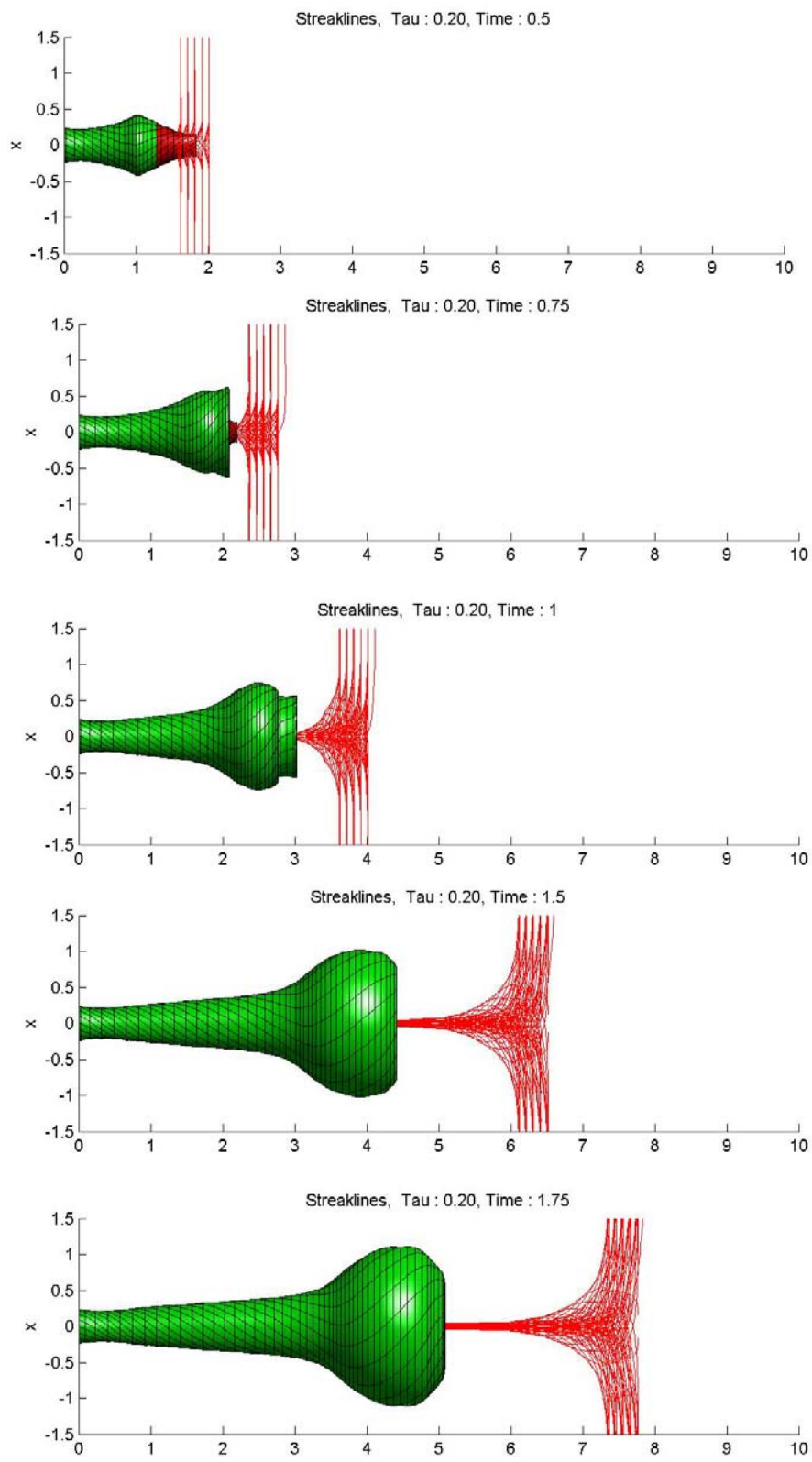
Figure 3-3 (cont)
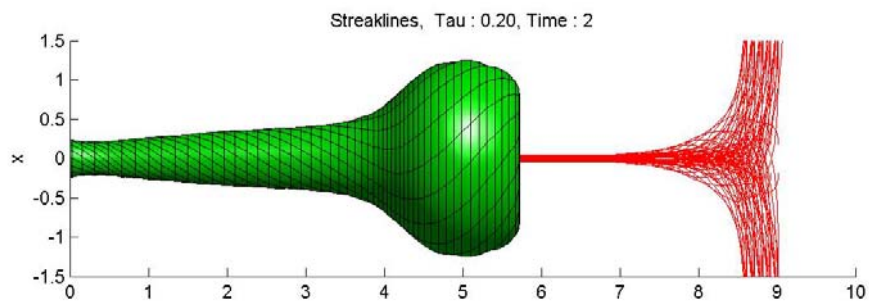
Figure 3-3 (cont)

The general structure and evolution of the vortex in our modified case is very similar to the results shown by Cain. In comparing our results to those of Cain, it is important to keep in mind that our modified simulation does not include the low circulation blue region used by Cain. In Cain's simulation, the ramp-up region (red region) emerged from the vorticity source immediately after the blue region, at T = 0.6. However, with no blue region, the ramp-up region (red) in our modified simulation begins immediately at T = 0. In short, the start of our modified simulation corresponds to Cain's simulation at T = 0.6.

The second set, shown in Figure 3-4, shows the same view of the solid representation but with r = 0.03, the inner most vortex filaments.
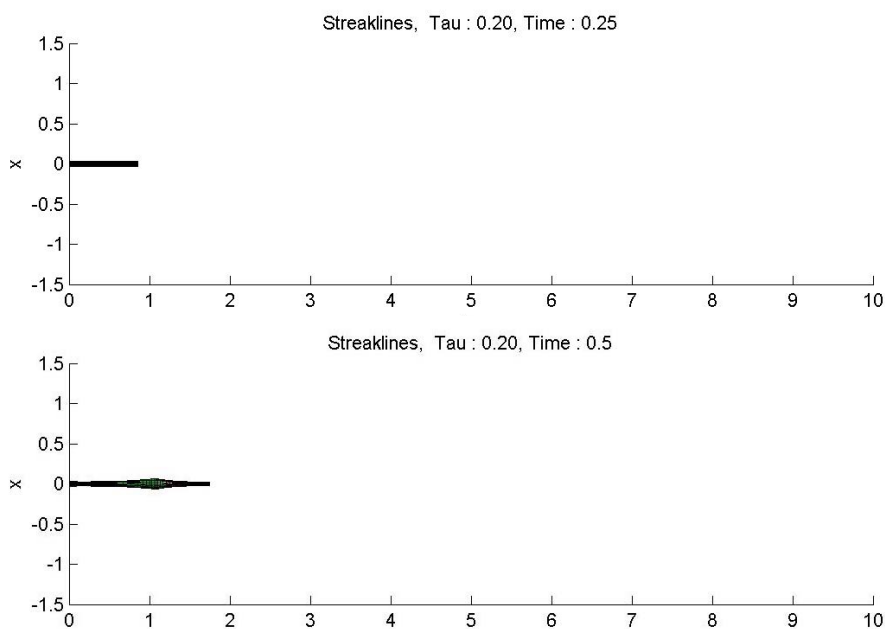
Figure 3-4: Modified simulation results, r = 0.03, τ = 0.20
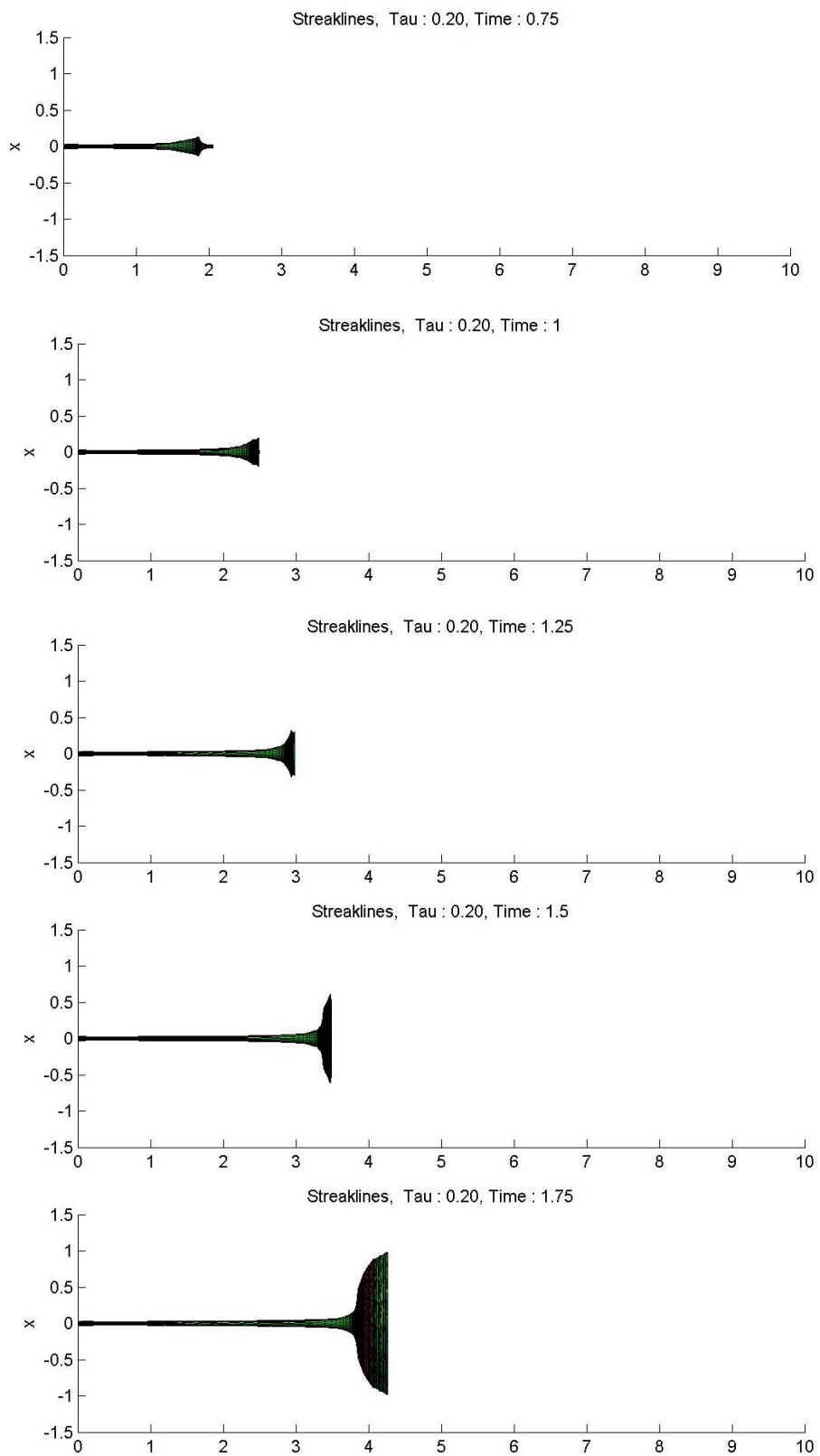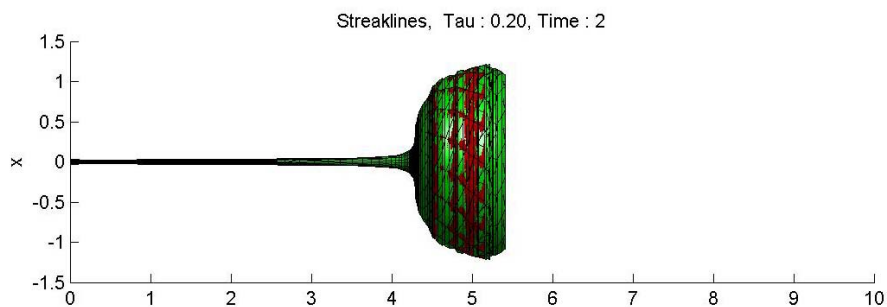
Figure 3-4 (cont.)

Figure 3-4 (cont.)

Unlike the r = 0.24 results, the r = 0.03 results are different than those offered by Cain.
The early development of the vortex, up to T = 1.0, matches that of Cain's results but
thereafter soon differ. In Cain's simulation, the streaklines of the inner most radii do not
suddenly explode into the recirculation bubble seen at T=2.0; instead, the behavior of the
streaklines is less dramatic as the initial tube is gradually expanded to form a more
streamline-shaped recirculation region. A side-by-side comparison of this is illustrated
below in Figure 3-5.
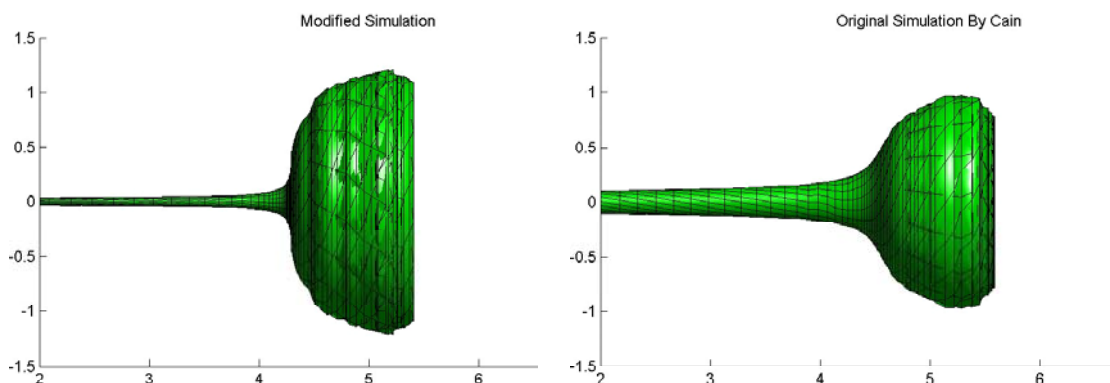
Figure 3-5: Comparison of inner radius streamlines with Cain

The third set of plots illustrates the interaction between the inner most radius,
r = 0.03, and the outer most radius, r = 0.42. The outside filaments are rendered
transparent in order to see inside of the vortex tube and visualize the inner most
filaments, shown in red. It should be noticed that the both the inner and outer radii
filaments initially expanded at the same time and axial location. As the vortex begin to
convect downstream, their respective expanding regions, or bulges, move together.
However, as the vortex tube expands further, the axial velocity of the inner filaments
decreases due to the increasing presence of backflow. This decrease in velocity causes

the inner filaments to lag . Furthermore, as the backflow increases, the inner most filaments wrap around the opposing reversed flow forming the core of recirculation bubble. Since it is primarily the initial explosion of the inner core which feeds the development of the recirculation bubble, we will choose to view the inner most filaments in determining the point of vortex breakdown.
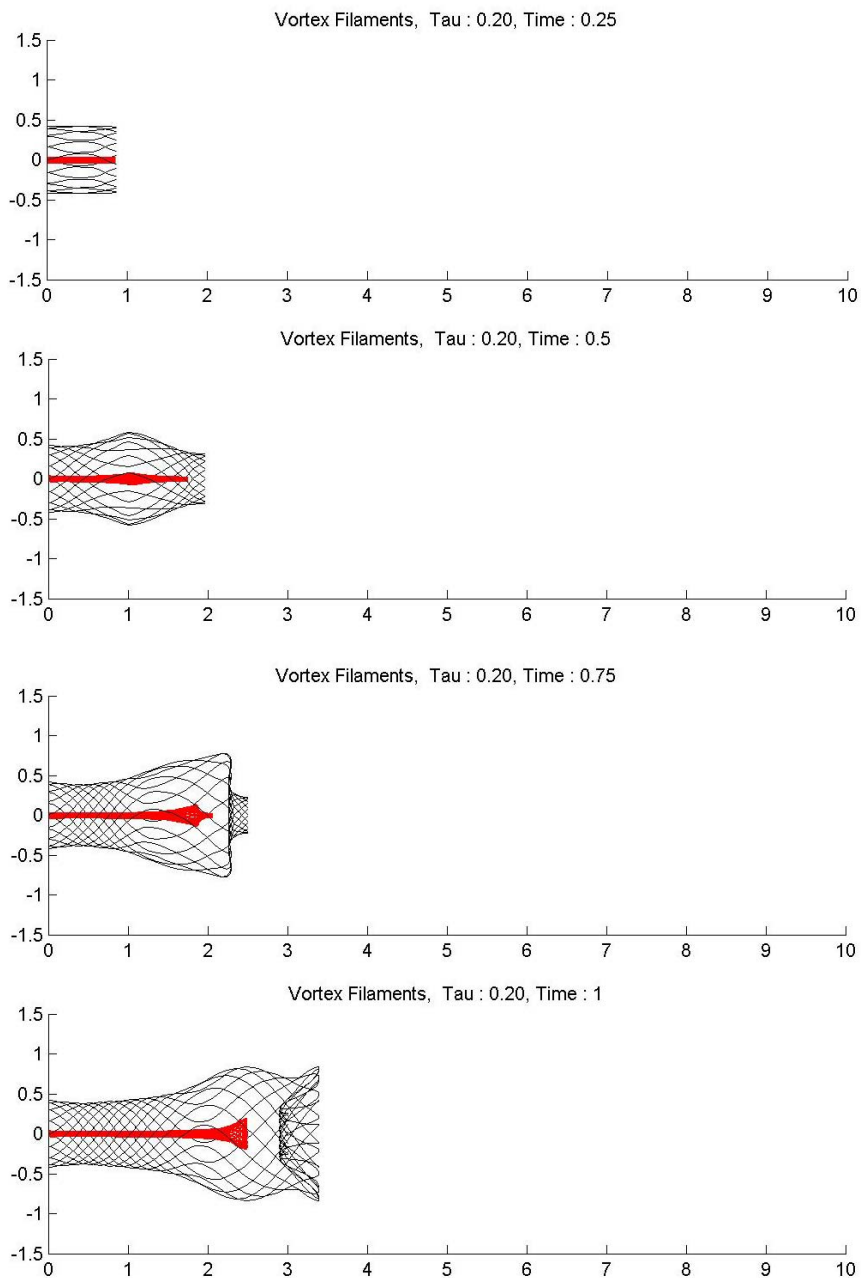
Figure 3-6: Vortex Filaments, r = 0.03, r = 0.42, τ = 0.20
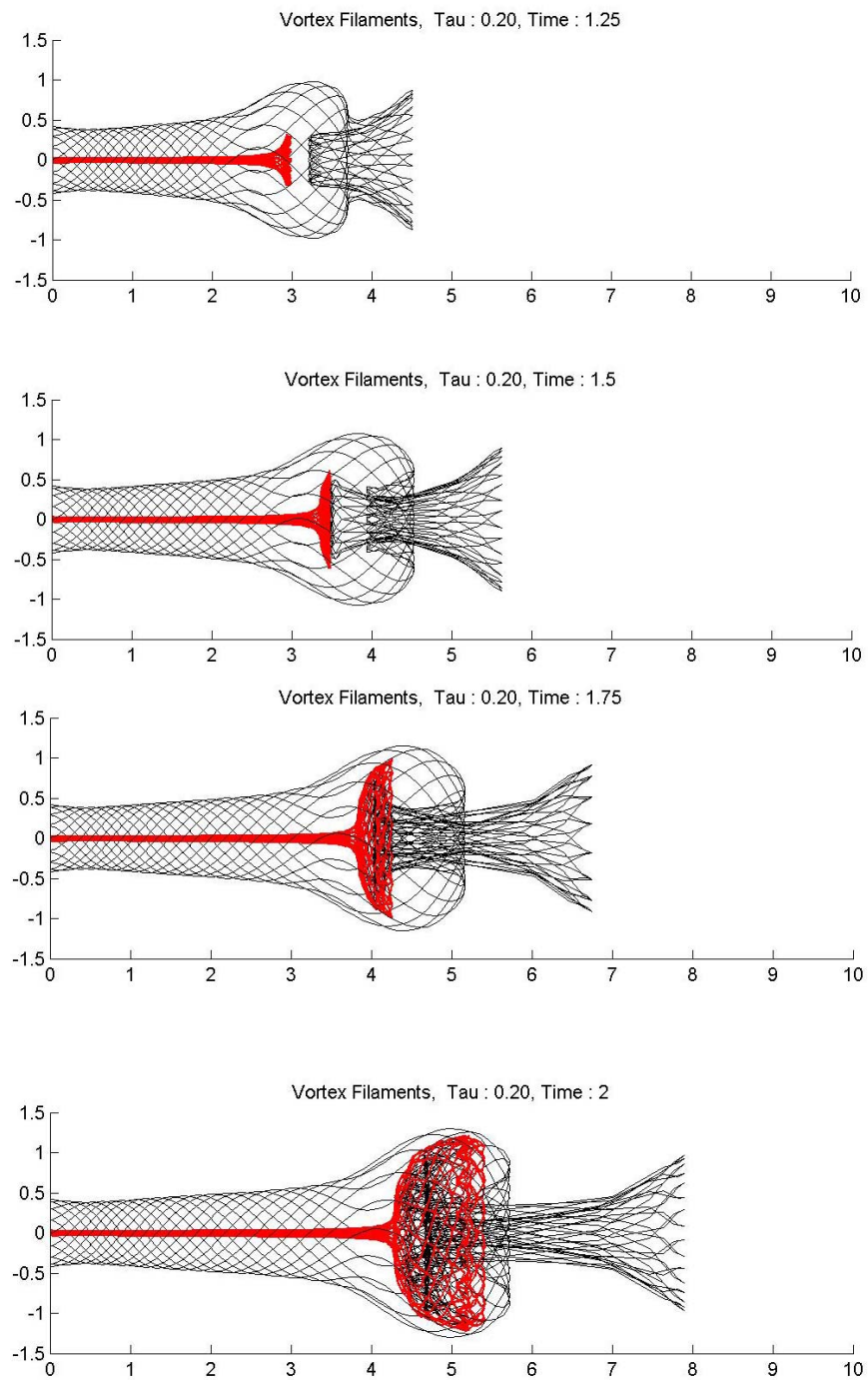
Figure 3-6 (cont.)

The behavior of the streaklines and the development of the recirculation bubble, at the inner most radius in particular, as offered by our modified simulation models the breakdown phenomenon better than Cain. This improvement can be seen when

comparing our streakline results to that of past flow visualization studies. Such a comparison is illustrated in Figure 3-7.
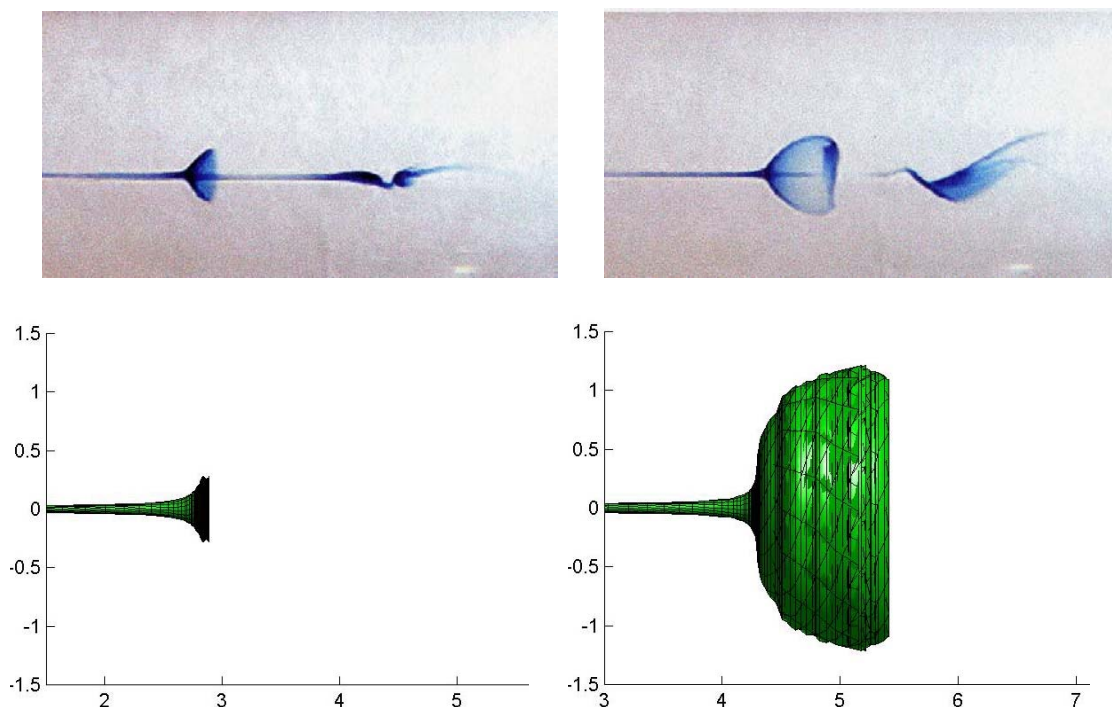
Figure 3-7: Vortex simulation comparison to experimental investigation (*ref.* 15)

The flow visualization pictures in the top half of Figure 3-7 are from a transient vortex breakdown study performed by Hamada (*ref.* 15). In his experiment, a needle valve located downstream of the test section is suddenly opened to initiate the vortex breakdown in a transient manner. It is this transient behavior which makes the results by Hamada an ideal source for comparison.   The simulation results match well with the flow visualization. One slight difference, though, is that the outer edge of both the initial and final bubble in the flow visualization is smoother than those of the simulation. It is important to remember that this is an inviscid simulation, and the smoothing effects of viscosity are not present. This inviscid nature is the reason for the jaggedness of the simulated bubbles. Similarly, it is the lack of viscosity which does not allow the recirculation bubble to reach a final stationary position in our simulation. In real flow, filaments with equal but opposite vorticity would cancel due to viscosity effects. However the simulation is not able to achieve this annihilating effect, and as a result, continues to impose undiminished induction from the filaments on the rest of the field;

this continuing mutual induction of filaments from within the recirculation bubble causes the bubble to convect downstream. Conversely, in real flow, the smoothing effect of viscosity would cancel out inflowing filaments, allowing the bubble to attain equilibrium position in the final state.

3.2 *Velocity and Vorticity Fields*

In this section, we present the azimuthal vorticity and radial and axial velocity as calculated along the meridional plane of the vortex tube. To aid visualizing the instantaneous vortex shape, vortex filaments at r = 0.12 and r = 0.42 are superposed onto the plots. All three sets of plots show much improvement over Cain's results immediately aft of the vorticity source, z = 0 boundary. One example of this improvement can be in the radial velocity plots. Cain's results showed a relatively large region of radial contraction immediately aft of the vorticity source. We will refer to this contraction behavior as the "necking effect." The modified simulation, with its improved upstream boundary conditions, is able to greatly reduce the necking effect, both in magnitude and in duration. Another improvement can be seen in the plots of azimuthal vorticity. Similar to the radial velocity case, the modified simulation is able to correct for inaccuracy of Cain's results immediately aft of the vorticity source; the azimuthal vorticity no longer approaches a zero value at the upstream boundary. These improvements are not only required to better model vortex behavior but are critical to the projected streamline study, which will be presented in the subsequent chapters.

3.2.1 *Color contour azimuthal vorticity plots*
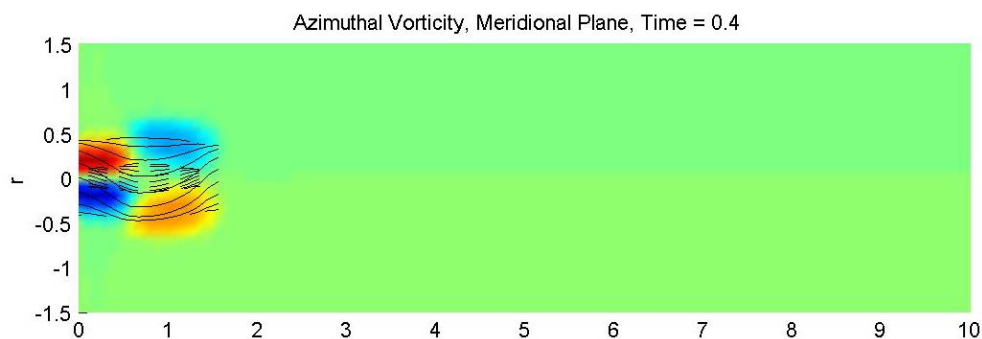
Figure 3-8: Azimuthal vorticity color contour plots
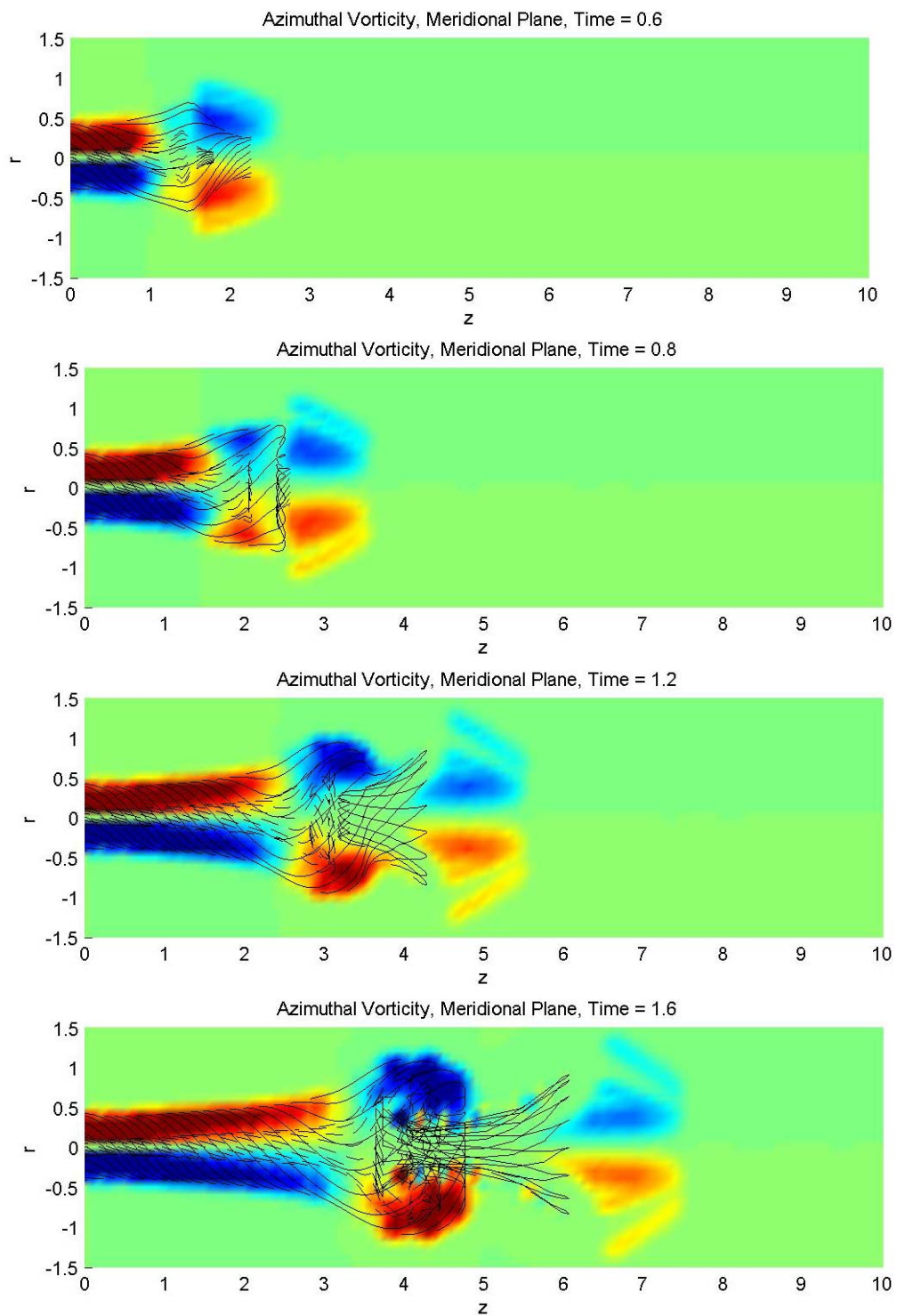
Figure 3-8 (cont.)

Figure 3-8 (cont.)
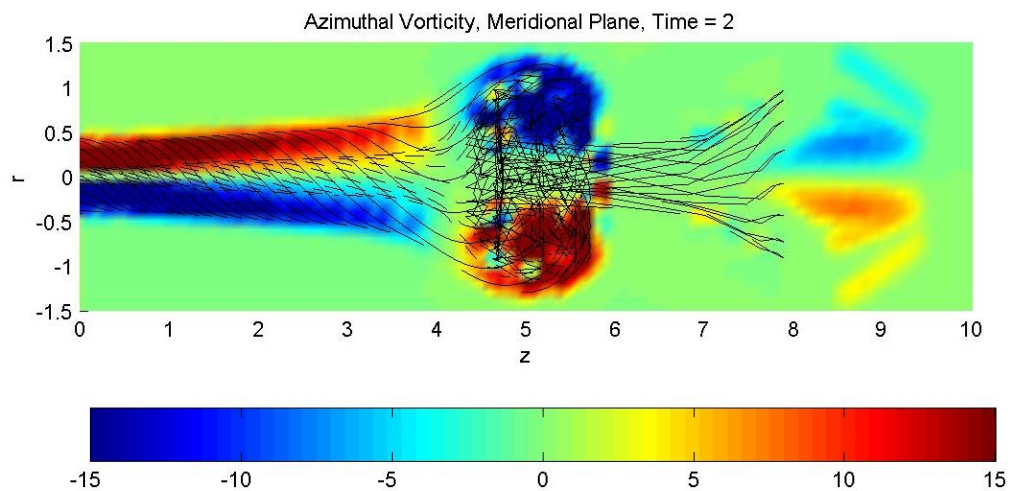
3.2.2   Color contour radial velocity plots
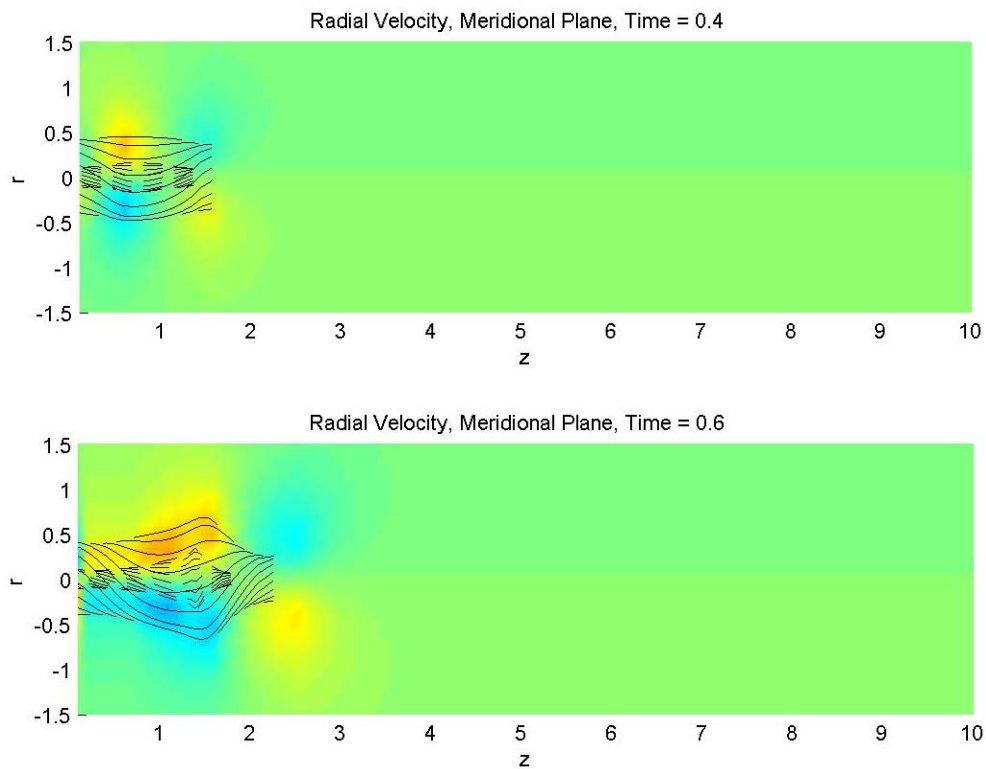
Figure 3-9: Radial velocity color contour plots
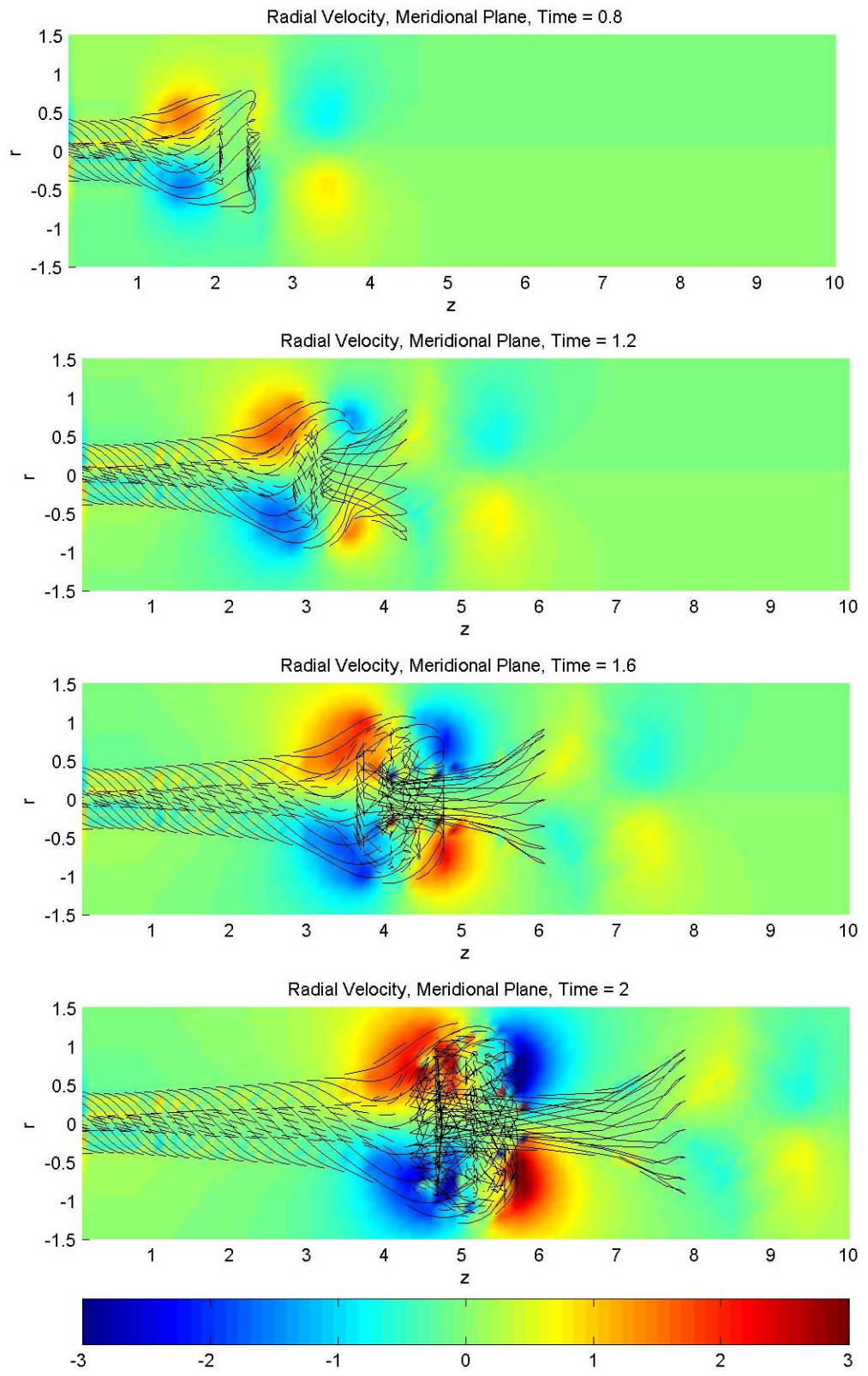
Figure 3-9 (cont.)

3.2.3   Color contour axial velocity plots
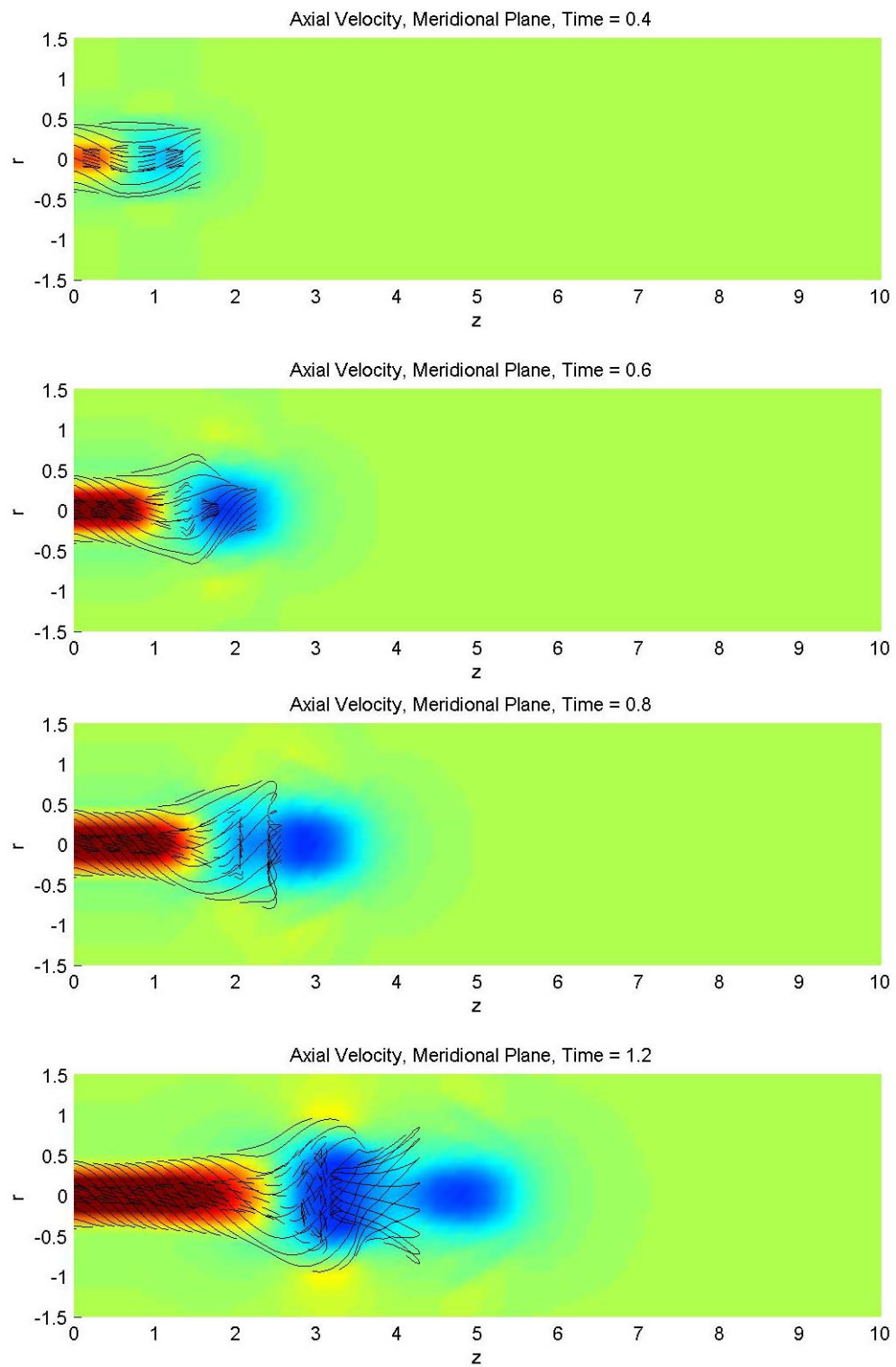
Figure 3-10: Axial velocity color contour plots
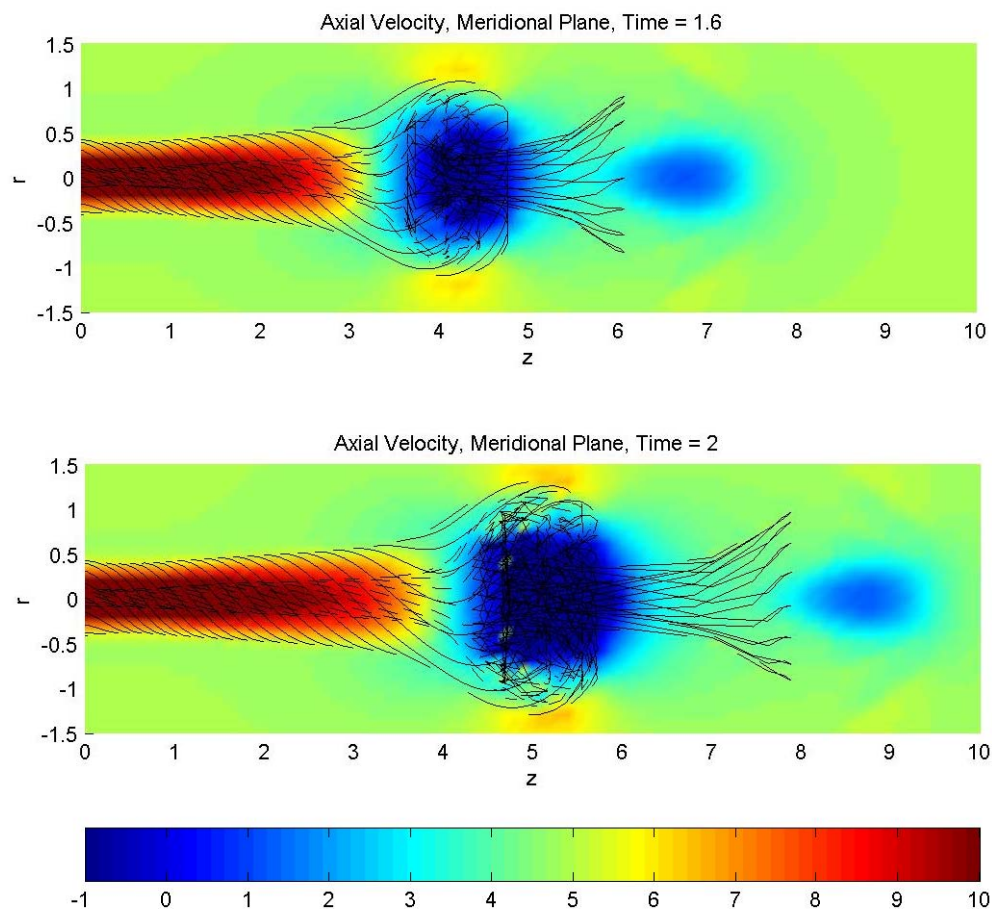
Figure 3-10 (cont.)

3.3   Validation of Breakdown Features

Past investigations have highlighted four principle flow features associated with breakdown: axial pile-up, radial expansion and contraction, a vorticity sign-switch and a flow turning point. Cain's simulation gave evidence to the argument that all four of these features are interlinked result of the self-induced, inviscid feedback mechanism of vortex breakdown. This section offers brief explanations of the four properties and gives evidence to their respective manifestation in the modified simulation results.

3.3.1   Radial expansion

Past studies have clearly shown that radial expansion arises directly from an azimuthal vorticity gradient. In order to offer an explanation for radial expansion, it is

best to present this azimuthal vorticity as a meridional cut of discretized vortices. This meridional cut is illustrated in Figure 3-11. The azimuthal vorticity of equal strength upstream decreases towards downstream and no vorticity exists beyond. At the first vortex, where there is no preceding vortex in the downstream direction, all the induction are additive such that the resultant is a radially outward velocity. As you move upstream, where the vorticity is of equal magnitude, the radially outward and inward induction by neighboring vortices cancel out. Extending this to a 3-D case, the induced radial velocity, produced by the azimuthal vorticity gradient, causes the vortex tube to expand in the downstream direction; once the azimuthal disappears, the radial size of the vortex remains the same, as seen in the radial velocity plots in chapter 3.2.3 near z=0.
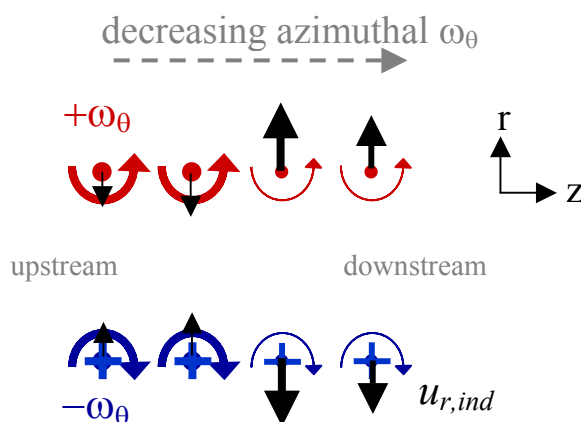
Figure 3-11:   Radial expansion (*ref.* 7)

3.3.2   *Axial pile-up*

The effect of the radial expansion, discussed in the previous section, also leads to axial pile-up. As noted by Cain, pile-up refers to the axial contraction of the vortex tube. Similar to radial expansion, pile-up is also a result of an azimuthal vorticity gradient. As with the previous section, we can use a meridional cut of discretized vortices, shown in Figure 3-12, to illustrate the creation of pile-up.
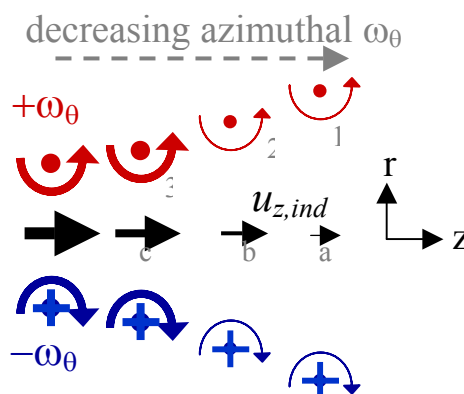
Figure 3-12: Axial pile-up (*ref.* 7)

Since the axially induced velocity at the center of the vortex is induced symmetrically, we can further simplify our example by considering the effects of only the top or bottom half row of vortices. In this case, we will look at the top row. The induced axial velocity at point (a) is generated only from all the upstream vortices; however, the greater part of the contribution comes from only a few neighboring upstream vortices. As you move further upstream, at point (c), the contributing pool of neighboring vortices include those downstream as well as upstream. As a result, induction comes from not only vortex (3) but from (2) and (1) as well. The additive induced velocities from both (2) and (1) cause the net induced axial velocity at (c) to be greater than either (b) and (a). As you move upstream and further away from the effects of vortex (1) and vortex (2), the induced axial velocity approaches a constant value. In the case of our simulation, this constant condition is established as the region of circulation change moves well downstream. Such constant axial velocity is illustrated in the previous contour plots of axial velocity. Observe also that the radial profile of the axial velocity reaches maximum at centerline, a jet-like profile. This is also analogous to the jet profile which develops at the leading edge of a delta wing vortex. Contrary to this case, a positive vorticity gradient would cause the induced velocities to be reversed. These reversed radial velocities would lead to axial acceleration and a contraction at the downstream edge.

The axial velocity gradient, illustrated in Figure 3-12, causes the axial components of the vortex filaments to contract. This axial contraction leads to the

increase in the cross sectional of the vortex segment. Since the local circulation around the vortex segment remains constant, this leads to decrease vorticity, thereafter, to a corresponding decrease in azimuthal vorticity. This decrease in turns creates a stronger azimuthal vorticity gradient and more pile-up. Therefore, once pile-up begins, this endless feedback cycle causes the effect of pile-up to dramatically increase with time.

3.3.3   *Vorticity sign-switch*

As previously noted in the explanation of axial pile-up, there is a decrease in vorticity in the location of a vorticity gradient. Hence, we would similarly expect a decrease in azimuthal vorticity in the regions of radial expansion and pile-up. Cain (2001) also noted that the azimuthal velocity gradient causes tilting in the vortex filaments in the region of radial expansion and pile-up. Due to this tilting behavior, the vector decomposition of the vortex filament will illustrate a reverse in azimuthal vorticity, referred to as the sign-switch. This tilting behavior is illustrated in Figure 3-13.
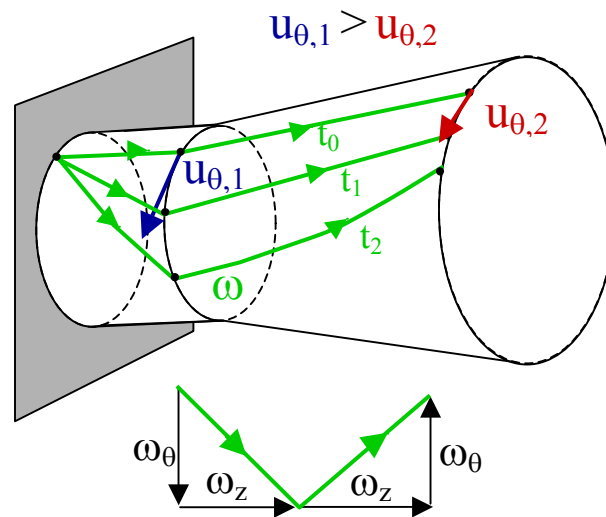
Figure 3-13: Azimuthal vorticity sign-switch (*ref.* 7)

As you can see in Figure 3-13, the azimuthal velocity at the downstream location has decreased from that of the upstream location due to the radial expansion and subsequent axial pile-up. If we then decompose the vector components of the vortex filament, we soon uncover the azimuthal vorticity sign-switch. Again, we can decompose the vorticity

vector because of the fact that the vector is always aligned with the vortex filament. This vortex tilting is furthered observed in our simulation results, as shown in Figure 3-14.
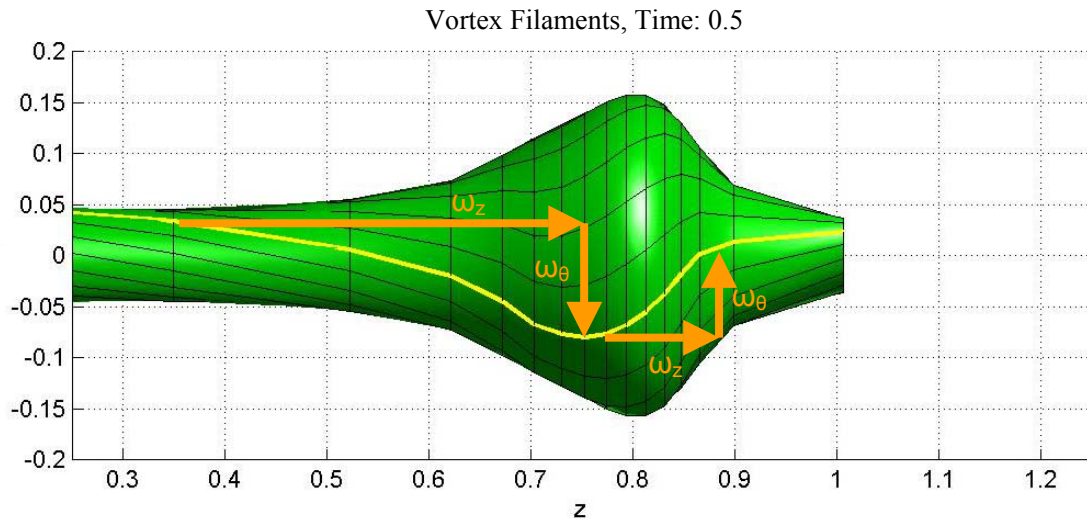
Figure 3-14: Azimuthal vorticity sign-switch, simulation results

Figure 3-14 illustrates the vortex filaments at $T = 0.5$ as well as the vorticity components projected along the meridional plane.

3.3.4 Turning point

The turning point is the location where the vortex filaments have turned inward on themselves. This culminating location is marked by a region of radial contraction and reversed axial flow inside of the vortex tube (backflow).   These two properties are both resultants of the induced velocities triggered by the azimuthal sign switch. The turning point can further be defined as the location where the axial vorticity is zero, such that the axial vorticity upstream of this point is positive and the velocity downstream along the filament is negative. This distinct point of separation manifests itself, in the vortex filament simulation, as the point where the vortex filament is vertical relative to the z-axis.

3.3.5   Property snap-shot

As supported by Cain (2001), vortex breakdown can be initiated and defined through the entirely inviscid mechanism of pile-up, radial expansion and contraction, and vorticity sign switching. The intertwining of these three behaviors, all of which are caused by a simple azimuthal vorticty gradient, culminates in the turning point. Once the turning point has been formed, the downstream region forms a dissipative, turbulent flow that leads to a steady state vortex breakdown. Similarly, the flow immediately upstream of the turning point continues to turn in on itself, creating a recirculation region. Within this region, the counter rotating flow further interacts with the upstream flow, leading to viscous activity. It is the dissipative viscous activity, along with the reversed axial flow, which leads to both the stagnation of the recirculation region and establishment of steady vortex breakdown.   Visualizations of the dissipative viscous activity within a nearly axisymmetric recirculation region are offered by Sarpkaya (*ref*. 16) in the Figure 3-15.
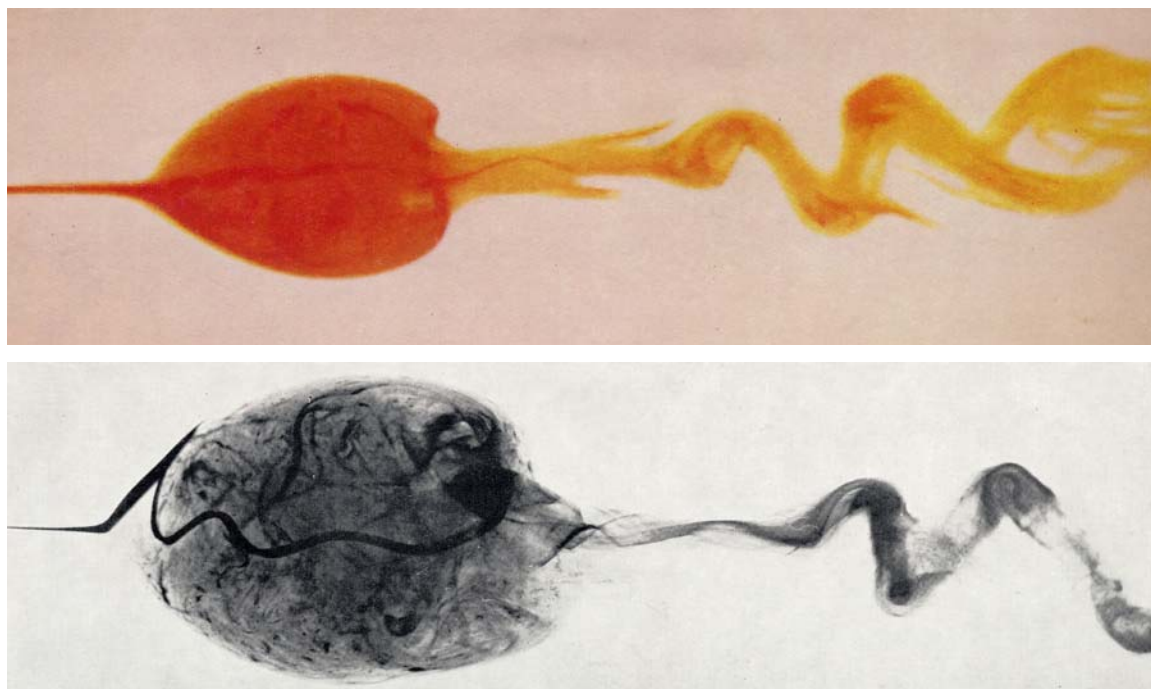
Figure 3-15: Viscous activity within an unsteady recirculation region (ref. 15)

In summary, the results of the vortex filament simulation support the notion that transient formation of vortex breakdown is not only an inviscid self-induced process but initiated by an azimuthal vorticity gradient.

The vortex filament method is a very powerful method as it enables us to see all four features of the inviscid self-induction mechanism in one simple snapshot of time. It is especially useful in illuminating the movement of the vorticity vector which soon manifests itself as the sign switch. One such snapshot is illustrated in Figure 3-16.
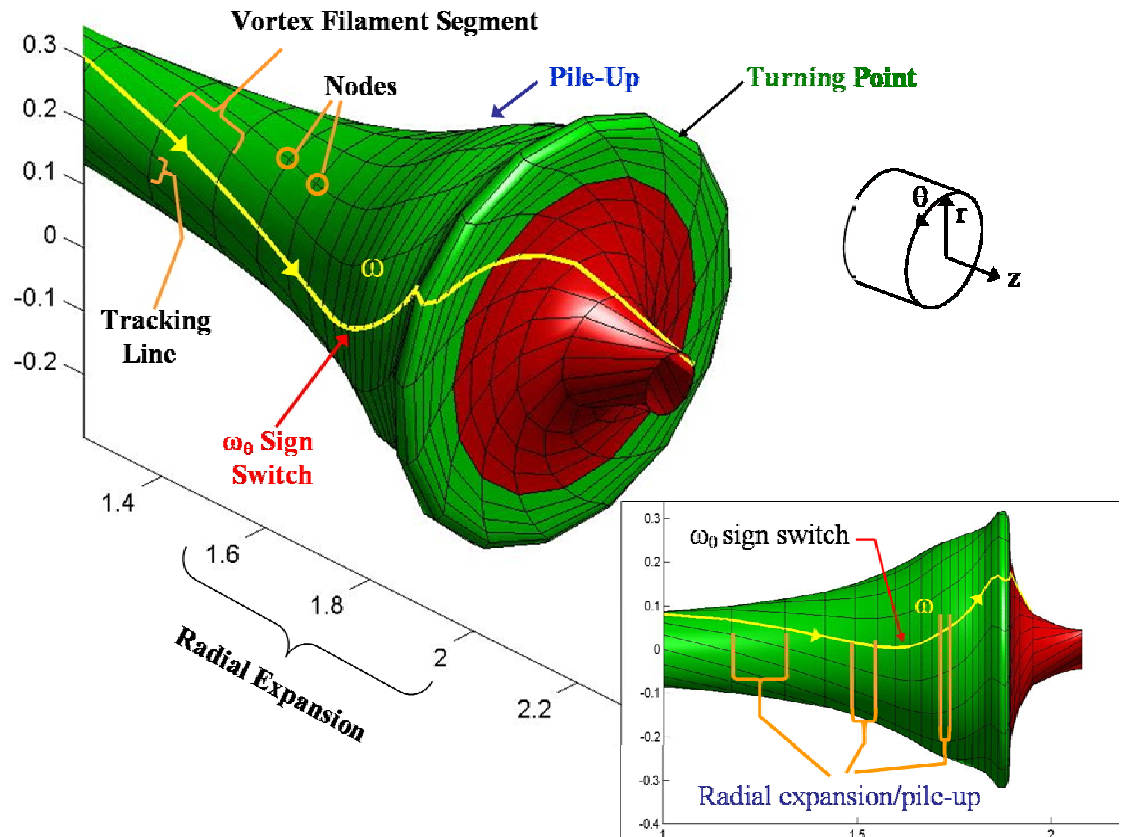
Figure 3-16: Properties of the inviscid self-induction mechanism

3.4   *Swirl Number Investigation*

Many non-dimensional parameters are considered and associated with the characterization of vortex flows have been considered. Dimensional considerations show that a global description of vortex flow must include some equivalent swirl parameter. As pointed out by Escudier (*ref.* 12), a swirl parameter can be defined in terms of numerous possible flow properties, to include axial flux and angular momentum flux. However, one such common and simple choice to define a swirl parameter is in terms of the bulk vortex velocity. By means of this velocity, the swirl parameter is expressed as

$$\Omega = \frac{C_\infty}{U_\infty \, L}$$

wherein C_∞ is the total circulation, U_∞ is the free stream velocity and L represents some length scale. This particular swirl parameter is commonly referred to as the swirl number, and has been used in many guidevane induced swirl studies. Since C_∞, which has the dimension of velocity and length, must depend on the angle of attack, or guide van angle, α, Ω is uniquely determined by α.

With this swirl number, this investigation is able to make a connection between, and further compare, the results of the vortex-filament method to those of experimental findings offered by Wimer (*ref.* 14). In his digital particle image velocimetry (DPIV) investigation of vortex breakdown, Wimer quantified flow fields of breakdown over a delta wing. With his measurements, he was able to calculate the circulation and velocity fields of the vortex flow over a delta wing at various angles of attack (AOA), in relation to the location of breakdown. By specifying the swirl number, Ω, in terms of the present simulation input parameters, and equating this Ω to corresponding experimental value we can associate the results of the vortex-filament method with his data at given a angle of attack. Figure 3-17 illustrates vortex streaklines, of r = 0.03, for various angles of attack.

Streaklines, Time : 1.7

3 deg AOA

Streaklines, Time : 1.7

15 deg AOA

Streaklines, Time : 1.7
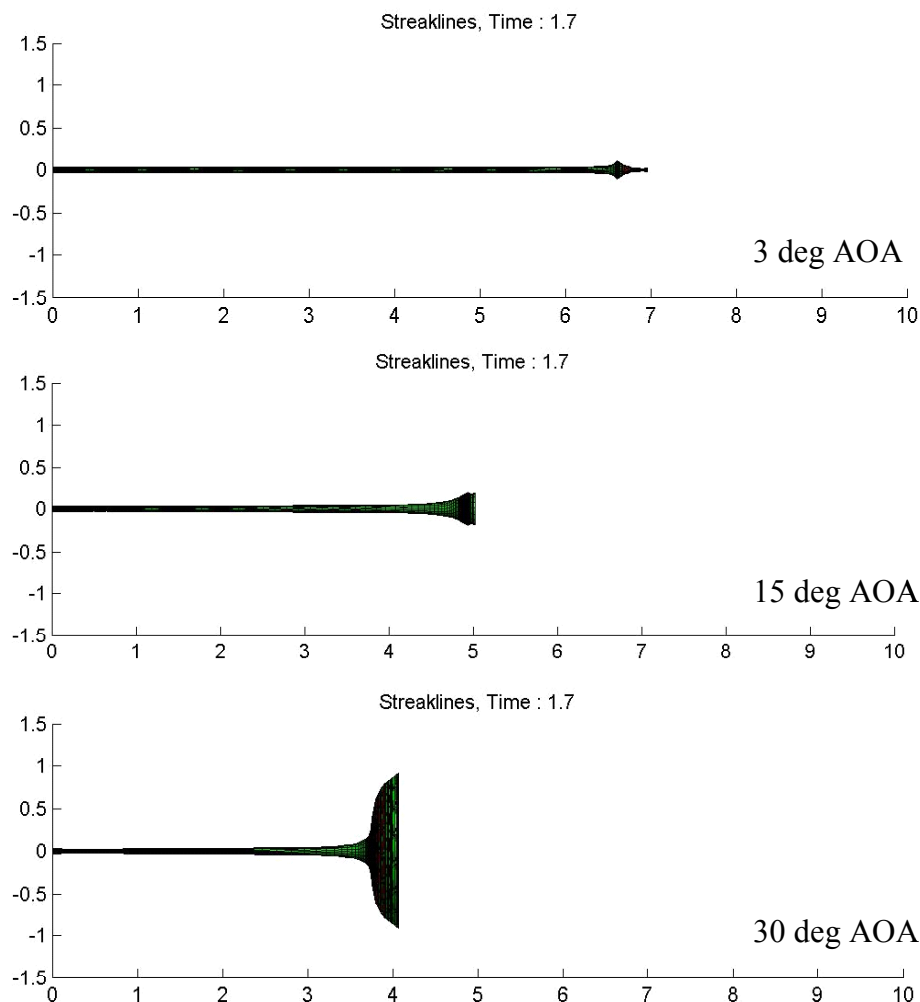
30 deg AOA

Figure 3-17: Simulation results for various equivalent angles of attack, r=0.03

As you can see from Figure 3-17, vortex breakdown has only occurred at the 30 deg angle of attack at T=1.7. The 3 deg vortex flow has translated furthest downstream because it does not experience the rigorous reverse flow phenomenon which is evident in the other two flows. Although the vortex flow in the 15 deg and 3 deg angle of attack case shows signs of radial expansion and possible reversed flow, no turning point has been observed. In fact, as time increases, the flow in both of these two cases continues to expand and transient downstream, but never reaches a stage to form a turning point. Although, we can not argue that the flow never breaks down, but rather can argue that the flow never breaks down within our established simulated domain. If we think of our domain in terms of a wing on a aircraft, the behavior represented in the 3 deg and 15 deg case would be analogous to vortex breakdown that occurs aft of the trailing edge. Our

findings hold true with Wimer, who noted that at angles less than 15 deg illustrated no breakdown occur over the delta wing surface

A point to note is that the delta wing used by Wimer has a finite chord length, whereas the only length scale in our simulation is that of the vortex core radius. However, we can use the 30 deg case as a baseline case to define the effective simulation chord length, c_{eff}, and by equating the swirl number of Wimer

$$\Omega_{Wimer} = \frac{C_{\infty max}}{U_\infty\, c}$$

to that of the present

$$\Omega_{VFM} = \frac{C_{\infty final}}{U_\infty\, c_{eff}}$$

and this c_{eff}, is used for other angles of attack. With this method we can further compare the breakdown locations of other equivalent simulations to those recorded by Wimer (*ref.* 14) and Srigrarom (*ref.* 17). The simulation for various swirl numbers is carried out by only changing the C_{final} value of Table 3-1, with the other parameters remaining unchanged. For means of comparison, the simulated location of breakdown, X_b , is defined to be the location at which the recirculation bubble has reached 95% of its maximum radial size.   These comparisons are shown in Table 3-2.

Table 3-2: Swirl Number (Ω) vs. experimental and simulated breakdown locations

Swirl Number	Equivalent Angle of Attack	Simulated Breakdown Location, X_b	X_b / c_{eff} (VFM)	X_b / c (Wimer)	X_b / c (Srigrarom)
Ω = 13.33	~30 deg	3.5	30%	30%	~30%
Ω = 11.11	~25 deg	5.2	45%	48%	~40%
Ω = 8.88	~20 deg	6.5	56%	60%	~70%
Ω = 6.66	~15 deg	None	-	None	None
Ω = 1.33	~3 deg	None	-	None	None

Since our simulation models an unsteady process, while steady-state is reached in experiments, the above method gives only a rough approximation of simulated vortex breakdown location. However, regardless of this fact, the data offered in Table 3-2 points out the effectiveness of the simulation to determine breakdown locations in reference to the experimentally-matched 30 deg baseline case.

One noteworthy criterion is the minimum swirl number value at which vortex breakdown first occurs within our effective domain. This threshold, referred to as the critical swirl number, $\Omega_{critical}$, was obtained by slowly narrowing down the swirl number range between $\Omega = 8.88$ and $\Omega = 6.66$. A critical swirl number of approximately 7.1 was reached. This critical value is equivalent to a 65 deg swept delta wing set at a 17 deg angle of attack.

3.5   *Ramp-up (time) Investigation*

One of the added benefits of the modified vortex-filament method is the ability to investigate the formative stages of breakdown at varying ramp-up times. The ramp-up time is the time required for the circulation and velocity profile to change from a condition at rest (C=0, U=0) to the maximum user-defined values. In physical terms, this ramp-up time is analogous to the time required for a wing to pitch-up from level flight to a specified angle of attack. All results up to this point have used a ramp-up time of $\tau = 0.20$. From experiments, we know that the resultant shape and orientation of bubble breakdown should be independent of pitch-up time, so long as the same final swirl number value is reached.   In physical terms, the breakdown over a wing does not matter how long it takes for the wing to pitch up to a specified angle of attack, so long as the same final angle of attack is reached.   Therefore, we would expect no differences in the formative stages of breakdown with varying ramp-up times; additionally, we would also expect to see all four previously discussed features of the inviscid self-induction mechanism. Figure 3-18 shows the modified simulation results of r=0.24 and r = 0.03 for the $\Omega = 13.33$ case at various ramp-up times.

One notable feature of Figure 3-18, is the difference in breakdown locations. The quicker the ramp-up (smaller the value of τ), the faster breakdown occurs. Likewise, the

quicker the ramp-up, the quicker the initial onset of radial expansion and azimuthal vorticity sign-switch.
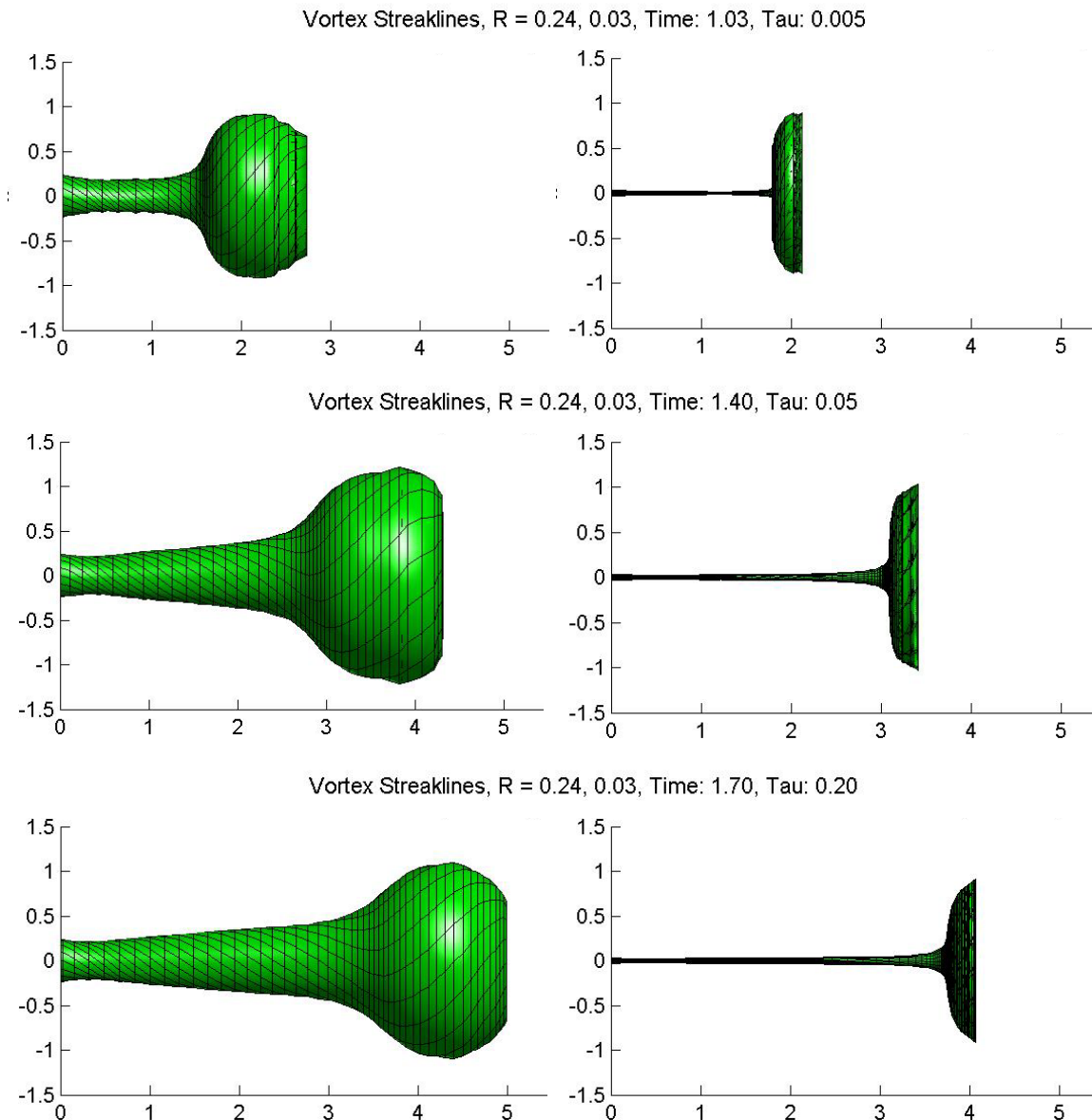
Figure 3-18: Vortex streaklines at breakdown for varying ramp-up times

In general, the smaller the τ value, the faster all aforementioned features of the inviscid self-induction mechanism are observed. This trend is attributed to the differential rate of change in circulation.   A faster differential rate of change in circulation causes a stronger vorticity gradient, which ultimately leads to faster breakdown. This trend is comparable to that of wingtip vortices on an aircraft. As an aircraft pitches up, it develops more lift

over the wings. This lift force is directly related to the circulation around the wing section. Therefore, the faster the pitch up, the larger the differential rate of change in circulation over the wing and the faster/tighter the roll-up of the wingtip vortices. In an effort to relate the onset of radial expansion to the formation of the breakdown bubble, we will introduce a new non-dimensionalized parameter, T^*. In this case, T^* is the ratio of the time at which the breakdown bubble is 95% expanded, T_B, to the initial radial expansion time of the vortex core, T_E.

$$T^* = \frac{T_B}{T_E}$$

The values of T_B, T_E and T^* for varying ramp-up times are shown below in Table 3-3. Please note that all three cases represented in the table were run with $C_{final} = 20$.

Table 3-3: Non-dimensional time (T^*) vs. ramp-up time (τ)

Ramp-up time, τ	T_E	T_B	T^*
$\tau = 0.20$	0.21	1.04	4.95
$\tau = 0.05$	0.28	1.39	4.97
$\tau = 0.005$	0.35	1.72	4.91

As you can see from the table, although the values of T_E and T_B differ for each case, the values of T^* are very similar. This fact would lead us to argue that there is a unique relationship between the time of initial expansion and the time of breakdown. Furthermore, it suggests that once the inviscid self-induction mechanism causes radial expansion, the subsequent process of breakdown is already predetermined. If this is true, then any attempt to control or manipulate breakdown must be focused not only at the far upstream position but early in the formative stages of breakdown – prior to the time of initial expansion. However, in order to further validate this argument, further simulations, at varying C_{final} values, and experiments need to be investigated.

4   Qualitative Investigation

The focus of this section will be to present a qualitative study of the shock-like behaviors exhibited in the preceding vortex filament simulation results. A discussion of these results is offered and compared with the traditional theory that breakdown behaves much like the sudden transition observed in a shock wave or hydraulic jump. Additionally, this section also gives insight into the scenario for the generation and subsequent growth of vorticity gradients, as well as their influence on radial expansion.

4.1   Elements of Shock-like Behavior

Numerous theoretical investigations with the aim of grasping the complex phenomenon of vortex breakdown have been made since the first reported observation of breakdown. Among the vast literature, many studies, Benjamin (*ref.* 18) and Keller *et al* (*ref.* 19) in particular, have considered the vortex breakdown problem from a shock-like perspective, making the analogy between a hydraulic jump and steady vortex breakdown. Although the vortex-filament method does not model the wave effects as such, the methods does provide valuable insight into the temporal evolution of flow parameters. For example, the gradual build-up of the axial velocity and vorticity, both of which commence at the onset of the simulation, culminate into a sudden jump or switch in magnitude. These sudden jumps in flow properties are manifested as the axial velocity stagnation location and sudden vorticity sign switch; both are present during breakdown.

4.1.1   Axial Pile-up

In addition to the raw velocity and vorticity data, the vortex filament method also enables us to look at the transient evolution of the filaments, subject to induced velocities, in their relation to each other. Since the filaments can become stretched and/or shortened during the simulation, it is best to visualize the axial location of the filament nodes rather than the actual filaments themselves.   Again, it is important to keep in mind that our simulation models the formative stages of transient breakdown. Figure 4-1 illustrates the axial position of nodes, pertaining to the inner-most radius, as a function of time. To help in visualizing the relative movement of the nodes, dotted lines are added connecting

identical nodes. In other words, the dotted lines represent axial trajectories of specific nodes. As you can see, the nodes do not maintain the initial equi-distant spacing (dz = 0.1) as the filaments begin to lengthen and shorten. This variation in nodal spacing is attributed to the difference in induced velocities caused by the self-induction process.
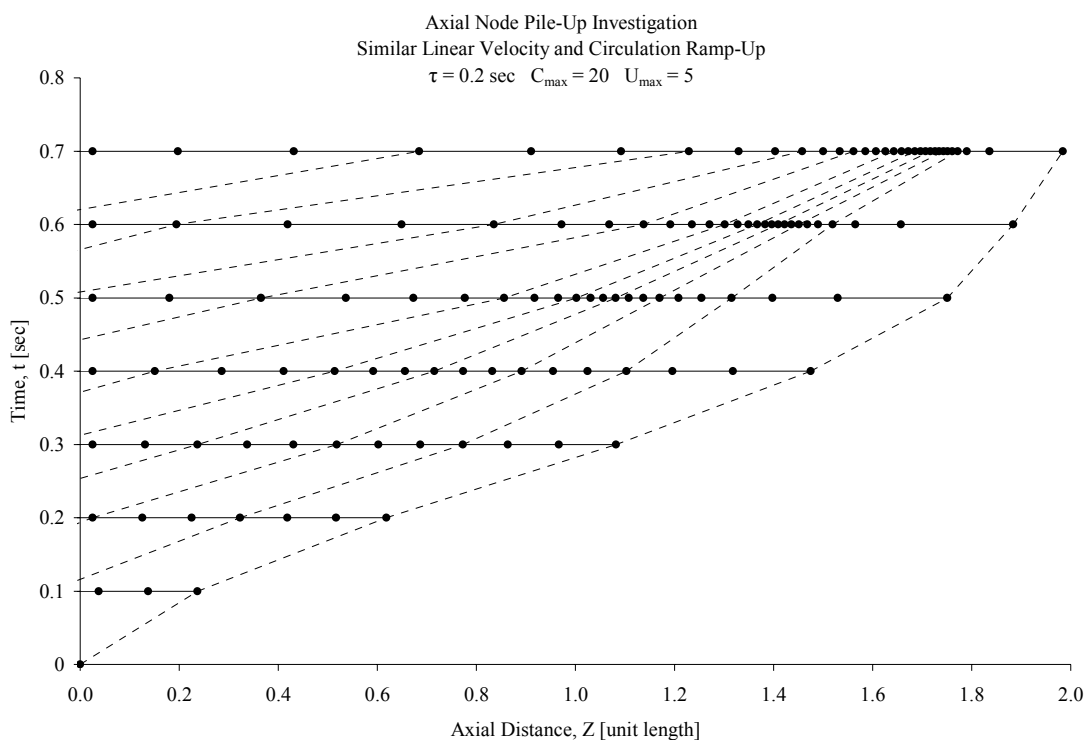
Figure 4-1: Shock behavior: axial node pile-up, short range

As time progresses, the spacing of incoming nodes is lengthened while the spacing between the nodes further downstream begins to shorten. This compacting behavior is referred to as 'pile-up' and is a result of the decreasing axial velocity downstream. This decreasing axial velocity is a precursor to the reverse flow seen immediately prior to vortex breakdown.

While Figure 4-1 illustrates the transitive effect of pile-up just prior to vortex breakdown, Figure 4-2 illustrates the continuing transitive effect after vortex breakdown has occurred. In this case, the number of nodes within the pile-up region has greatly increased, even though the axial width of the region has not. Clearly, this pile-up effect is analogous to the temporal formation of a shockwave. Since our simulation is a

transient study, the recirculation region and stagnation point is continuously convected downstream.   It is because of this reason that the pile-up region, which is closely located to the recirculation region, continues to transient downstream in Figure 4-2. Similar to Figure 4-1, lines are used to trace the relative movement of similar nodes. However, in this case, the colored lines are shown to highlight an important behavior – nodal overlapping. If you look at T=1.5, you will see the green, blue and red lines, in ascending order. However, at T=2.0, the order of the lines are reversed. This inversion is caused as downstream nodes are pulled or "sucked" into the recirculation region, overlapping the nodes immediately behind them. This continuing overlapping behavior can also been seen experimentally, as flow passing over the breakdown shear layer is reversed and circulated back through the bubble. It is important to note that the simulation results give rise to a systematic overlapping behavior during breakdown. By systematic, we mean that the behavior follows an orderly sequence and is not simply a random scattering of nodes.
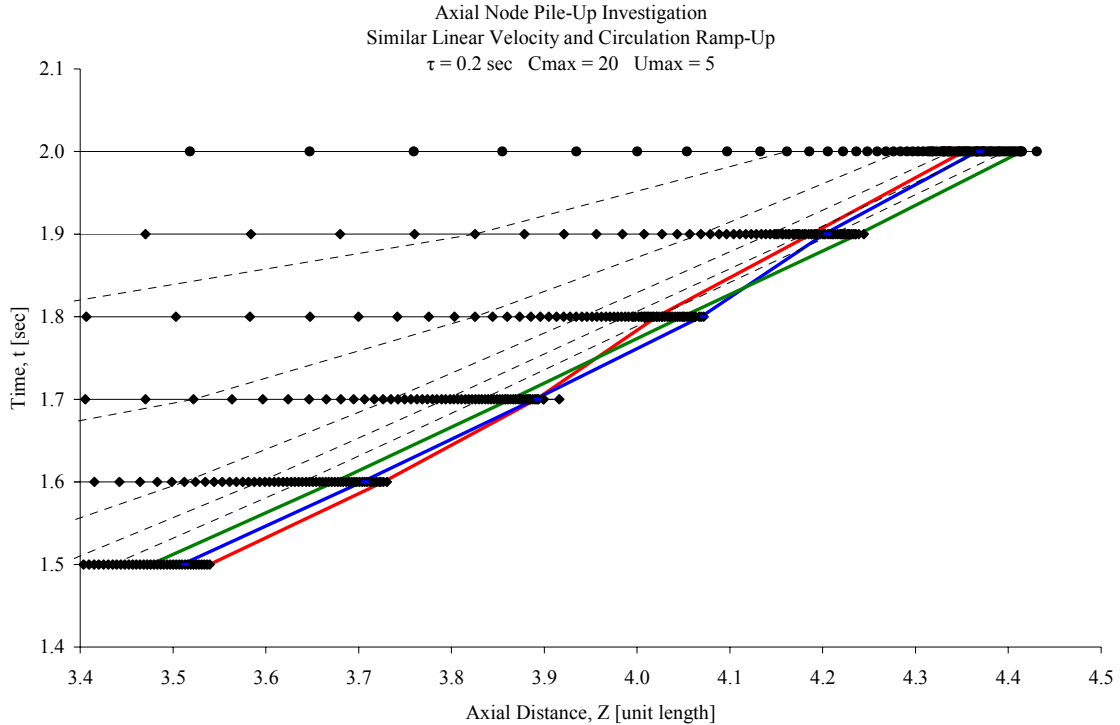
Figure 4-2: Shock behavior: axial node pile-up, long range

Another method of illustrating the shock-like behavior of vortex breakdown includes graphing the inner-radius (r=0.03) nodal spacing between adjacent nodes, Δz, as a function of axial distance. This method is shown in Figure 4-3 and Figure 4-4. Similar to the previous plots, Figure 4-3 also illustrates a transient shock-like behavior.   By T = 0.8, which is just prior to breakdown, the spacing of the vast majority of nodes is much less than the initial dz=0.1 value. In fact, the downstream nodal spacing appears to approach Δz=0 as time progresses. The negative Δz values represent the nodal overlapping effect. According to the figure, nodal overlapping begins at approximately T=1.6. This time matches well with the previous plots, as it is exactly the same time we saw the colored lines begin to overlap, in Figure 4-2.
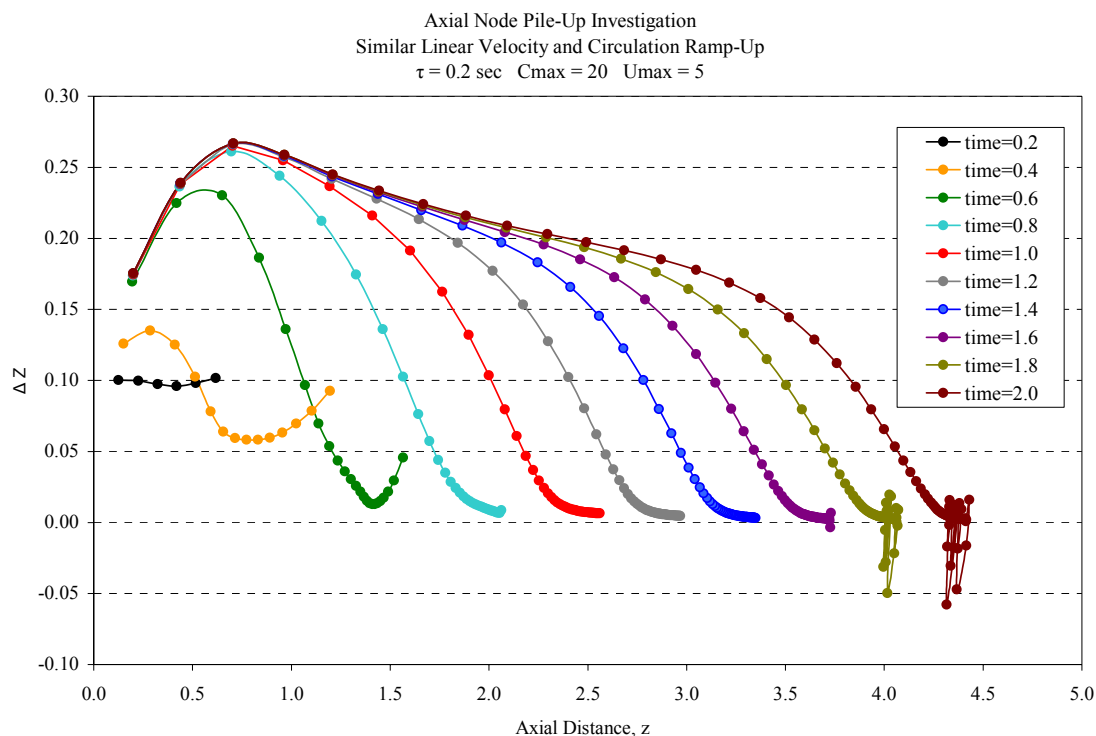
Figure 4-3: Nodal spacing (Δz) vs. axial distance, long range

Although Figure 4-3 shows a long range time history of the transient shock-like behavior and axial pile-up, it does a poor job at showing the early transient behavior. In contrast, Figure 4-4 illustrates better the nodal spacing as a function of axial distance given at the early time range of T=0.12 to T=0.30. In this figure, you can see a more refined transient

behavior.   In the preceding chapter, it was shown that the initial swelling of the vortex tube occurred at approximately T=0.21, for the current τ=0.20 case. In agreement with this, it is clearly evident from Figure 4-4 that pile-up has also started at this time. As continuity states, this supports the argument that axial pile-up and radial expansion begin simultaneous.
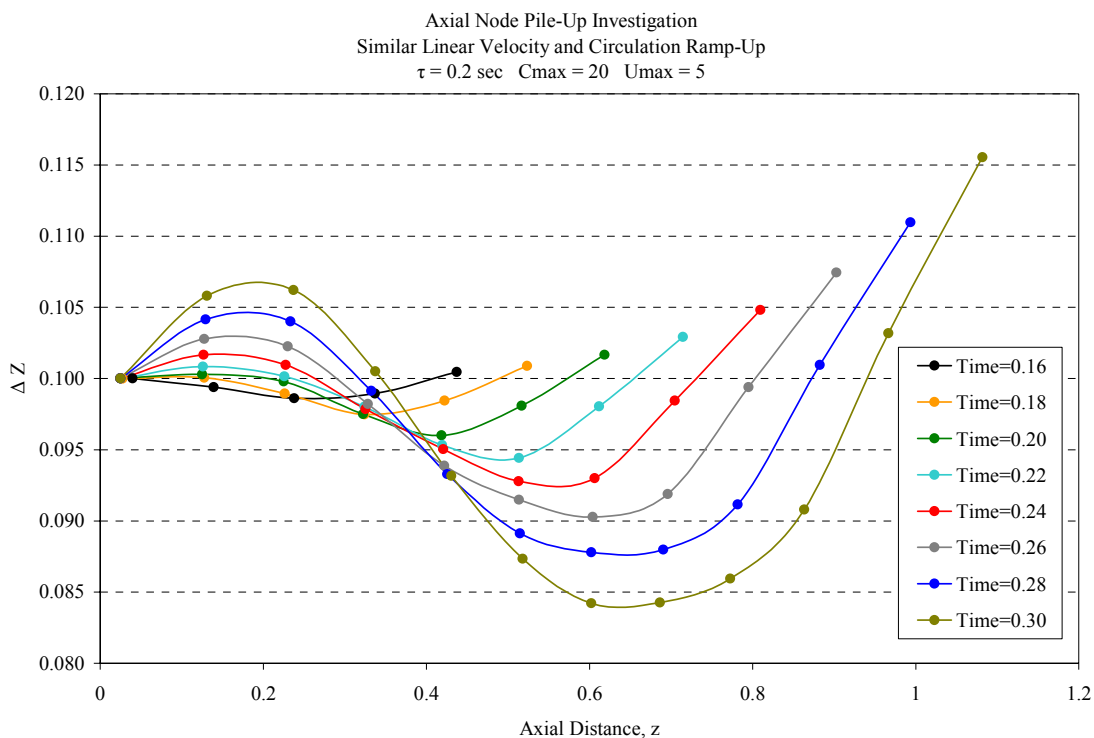
Figure 4-4: Nodal spacing (Δz) vs. axial distance, short range

4.1.2   Radial Pile-up

The previous section investigated the axial movement of the filaments subject to induced velocities in relation to each other. In doing such, the connection between the filament behavior during transient breakdown and that of a shockwave was made. However, the results can be deceiving because the investigation looked only at the pile-up of nodes along the streamwise axis, z, excluding any pile-up effect in the radial direction. In order to fully visualize and account for three dimensional pile-up effects, we must further investigate the transient behavior of pile-up in the radial direction. One method of illustrating the relative radial pile-up is to view a meridional projection of one

filament, initially emerging at z=0 at r=0.03, the inner most radius, focusing on its corresponding nodes. An example of this projection is shown is Figure 4-5, which the gives better insight into the existence of radial pile-up. However, since it is a meridional projection it is still quite hard to distinguish between the axial spacing and radial spacing. For example, from the three-dimensional rendering representation in Figure 4-5, we know that the yellow filament traces a spiral streakline as it turns around the vortex core and into the plane, becoming hidden in this side-view. However, this fact is not so clearly evident in the meridional projection of the filament nodes. In fact, the two-dimensional projection does not aid in the ability to distinguish when the filament turns into the meridional plane from when it turns out of the plane.
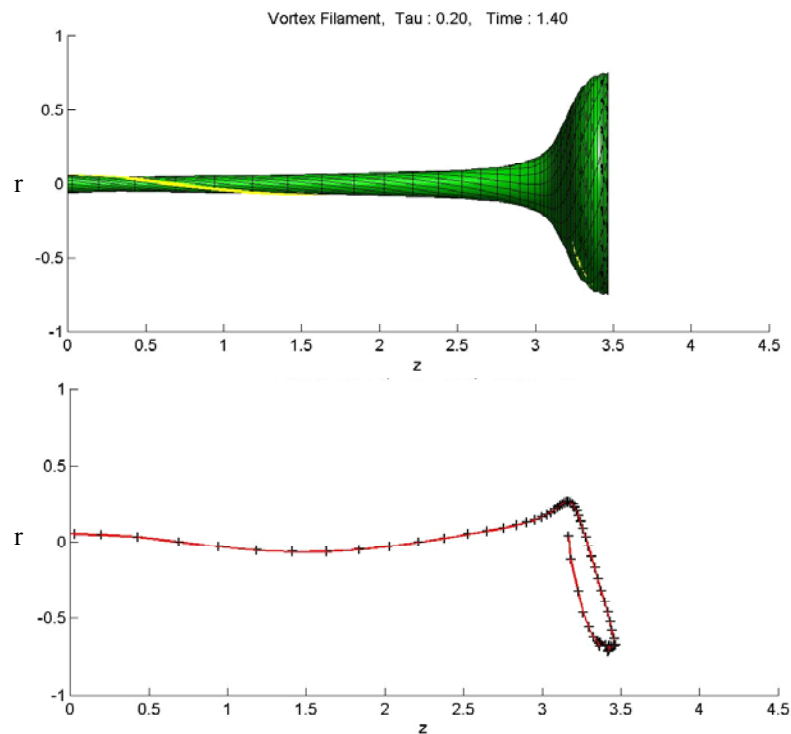
Figure 4-5: Radial pile-up: meridional nodal projection

This shortcoming of the meridional projection is evident throughout the entire history of the vortex flow, as shown in Figure 4-6.
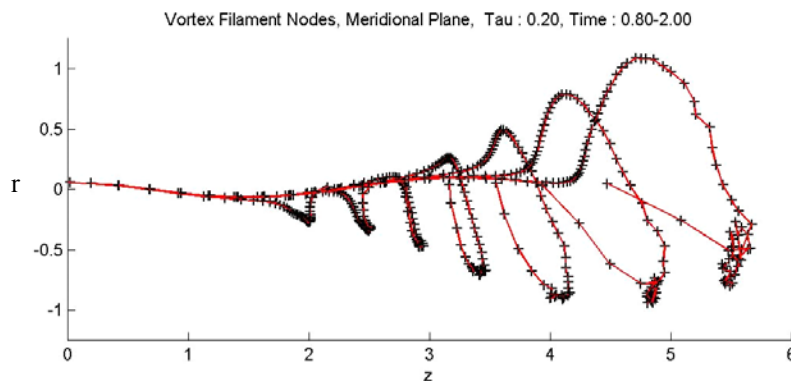
Figure 4-6: Radial pile-up: time history of meridional nodal projection

Another method of illustrating the radial pile-up is to project the filament nodes onto a plane orthogonal to the meridional plane. You can think of this case as an end-view, sitting on the centerline far downstream and looking up the vortex core (z-axis) toward the vorticity source. This projected view is illustrated in Figure 4-7. This view gives a much better interpretation of the radial pile-up, as you can now witness the spiraling streakline. In this case, movement in the positive y-axis direction represents a turn into the meridional projected plane.   However, in opposition to the meridional projection, this orthogonal projection gives no information in regards to the axial spacing. In fact, Figure 4-7 gives no information concerning the nodal overlapping, which can be seen in the meridional plane.
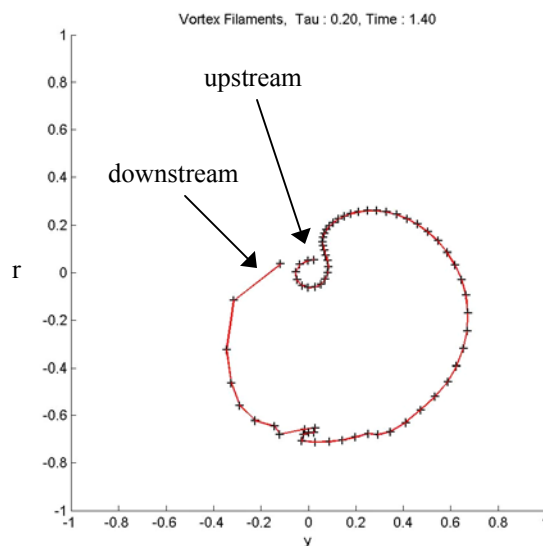
Figure 4-7: Radial pile-up: end-view projection

Although the orthogonal projection method offers additional spacing information, it is no better in representing the absolute spacing between nodes along the filament than that of the meridional projection.

4.1.3   Pile-up Along Filament Length

As shown in the previous sections, a shock-like pile-up behavior occurs in both the axial and radial directions. Therefore, in order to capture the absolute spacing of the nodes we must be able to interpret the respective directional spacing simultaneously, rather than independently. The axial projection and end-view projection alone fail to illustrate this absolute spacing between two adjacent nodes, because neither is able to account for simultaneous movement in both planes.

Thus, one simple planer projection of node locations is not sufficient to achieve this multi-dimensional assessment. Instead, we must represent the nodal spacing along the vortex filament length. A perspective view is offered in Figure 4-8. On the left side of the figure is a three-dimensional rendering of the r=0.03 streaklines. Amidst the solid surface, a yellow line traces out an individual vortex filament. On the right side, this individual streakline is then isolated and its respective filament nodes are highlighted. (It does not matter which filament within the radial shell we choose to highlight, since the vortex-filament method assumes that the spiraling flow is axisymmetric.)
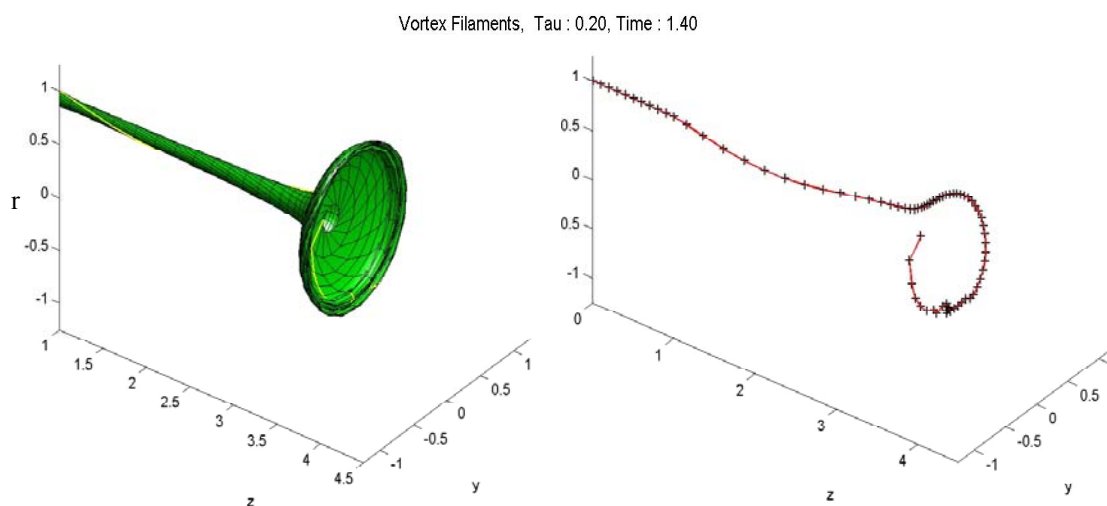
Figure 4-8: Absolute pile-up: perspective view

Figure 4-8 is able to illustrate the connection between axial and radial pile-up much better than any projected method. As you can see, as the axial pile-up is accentuated, the filament turns causing a sudden radial expansion. The filament then continues to wrap around and be drawn into the newly formed recirculation bubble.

Using the nodal position data from the vortex-filament method, a plot of absolute spacing along the vortex filament can be computed. This plot is shown in Figure 4-9. Similar to the axial pile-up plots, the pile-up along the filament length also exhibits a spatial compression and sharp singular-like point, at L=3.3. As a means to aid in relating key positions along the vortex filament to their respective axial locations, equivalent axial positions are noted in the text boxes. Since we are investigating the spacing along the filament length, it is useful to note where the filament obtains the farthest downstream position, prior to being sucked back into the bubble. This position is marked with a text box (z=3.45). Therefore, any nodes further along the filament length have been sucked back into the bubble. Additionally, a side view of the rendered vortex surface is also shown in the figure to help correlate regions of radial expansion with the nodal spacing along the filament.
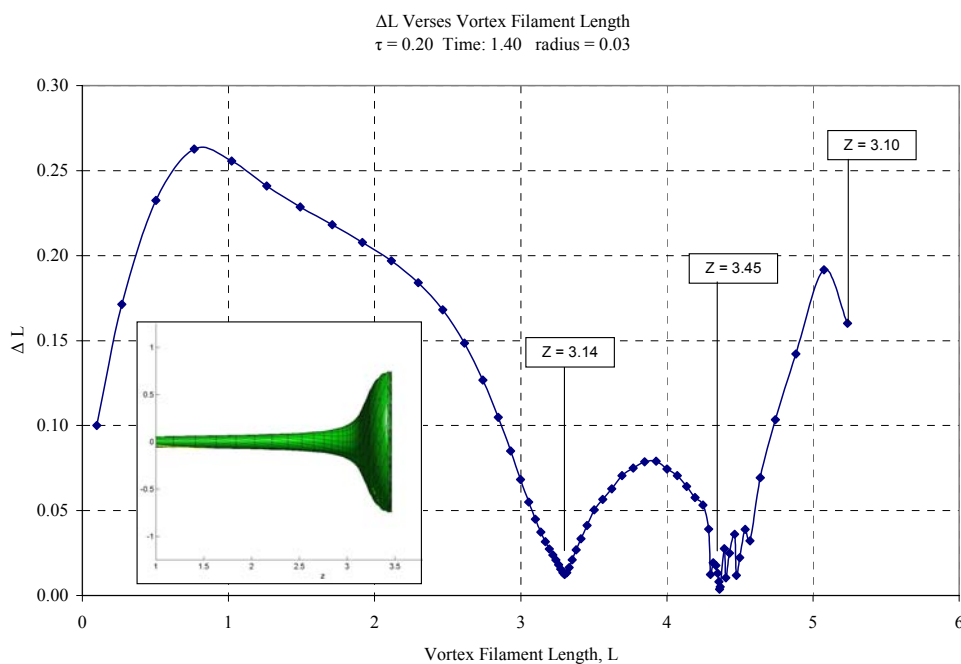
Figure 4-9: Nodal spacing along vortex filament, r=0.03, T=1.40

As you can see, the most intense area of absolute pile-up is located at an equivalent axial distance of 3.14. This location is the exact location where the sudden radial explosion occurs at the forefront of the recirculation bubble. Figure 4-9 only illustrates the nodal spacing along the vortex filament at a particular moment in time (T=1.40). Figure 4-10, however, shows the temporal evolution of the nodal spacing along the filament. From this figure, you can see that nodal pile-up begins early in the transient stages of breakdown, where as the sharp singular-like point evolves at a later time. This sharp kink in the line occurs at approximately T=1.20, which is roughly the same time the recirculation bubble has been fully established.

ΔL Verses Vortex Filament Length
$\tau = 0.20$ $\Delta t = 0.01$ sec   radius = 0.03
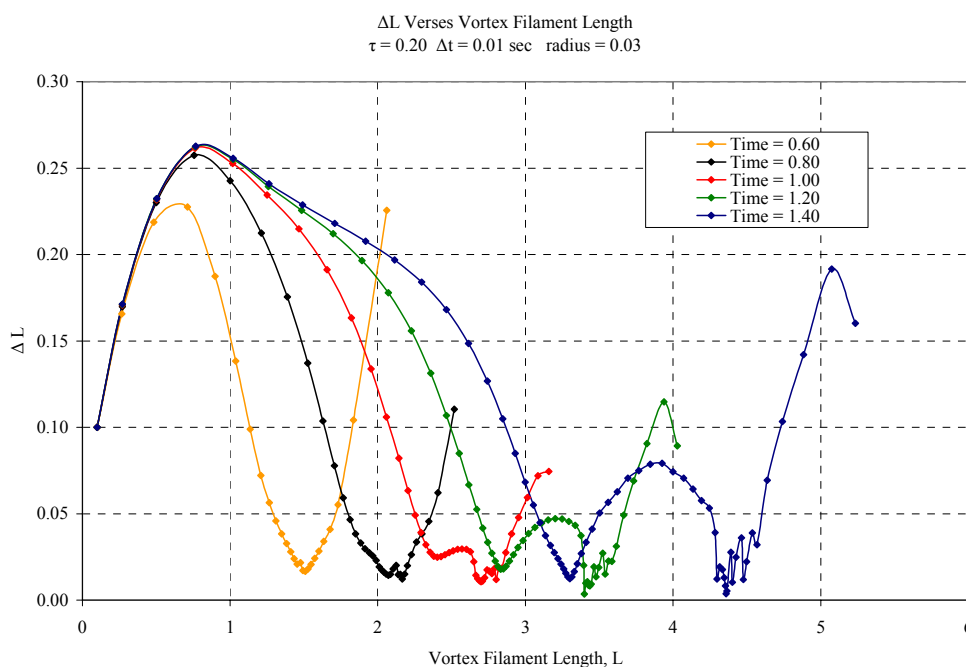
Figure 4-10: Time history of nodal spacing along vortex filament, r=0.03

4.2   *Vorticity Gradient Scenario*

Traditional views of the vortex breakdown have attributed the initial radial enlargement to the presence of an adverse pressure gradient, such as the gradient observed in a diverging pipe or over a delta wing. This investigation will argue that the initial vortex expansion and its subsequent radial growth are both a result of the self-induction among the vortex filaments subject to a vorticity gradient. Furthermore,

whenever the azimuthal vorticity decreases downstream, the resulting negative
vorticity gradient triggers both the initial expansion and sustained radial growth.

4.2.1   Generation of Negative Azimuthal Vorticity Gradient

Consider a vorticity vector, $\vec{\omega}$, with end coordinates *a* and *b* on the cylindrical
surface of the vortex core in the region where the azimuthal velocity, u_θ, is decreasing
downstream. Please refer to Figure 4-11 A & C. Again we must point out that the
vorticity vector always moves with the fluid. Therefore, as the vorticity is convected
downstream, the downstream and trailing end, *b*, spins at a slower rate than the upstream
and leading end, *a*, due to the difference in the azimuthal velocity. Consequently, as the
vorticity is pushed downstream, it transforms to $\vec{\omega}'$. This new vector, illustrated in
Figure 4-11A, is tilted and now defined with endpoints *a'* and *b'*. The differential rate of
spin is the cause of the titling behavior, which further causes the azimuthal vorticity
component of $\vec{\omega}'$ to be less than that of $\vec{\omega}$.

Correspondingly, the azimuthal vorticity, ω_θ, also decreases with downstream
distance in the region of decreasing azimuthal velocity, u_θ. The tilting behavior
continues to amplify as the vorticity vector is convected further downstream. Eventually,
the magnitude of the tilting gets so large that ω_θ may become negative and switch
directions. Please refer to Figure 4-11B. This azimuthal vorticity sign switch may occur
even for a vortex core of constant radius, somewhere in the region of circulation change,
or circulation ramp-up in the case of our simulation. In other words, somewhere between
the start of the simulation, represented by point *p*, and the time when the maximum
circulation value is attained, point q, there exist a region where the azimuthal vorticity
gradient becomes negative.

$$\frac{\partial \omega_\theta}{\partial z} < 0 \ \text{ or } \ \frac{\partial \omega_\theta}{\partial s} < 0$$

The magnitude of negative azimuthal vorticity gradient in the region of negative gradient,
increases at the same time the sign-switch occurs. Please refer to Figure 4-11D.
Accordingly, this increase in magnitude further incites the radial enlargement of the

vortex core. It is the inviscid self-induction process subjected to a prescribed negative vorticity gradient which causes the initial expansion of the vortex tube. Furthermore, this region of initial expansion, which has been found to occur in the region of changing circulation, will be shown to shift upstream into the steady-state region of circulation with time.

(A)

(B)

(C)

(D)
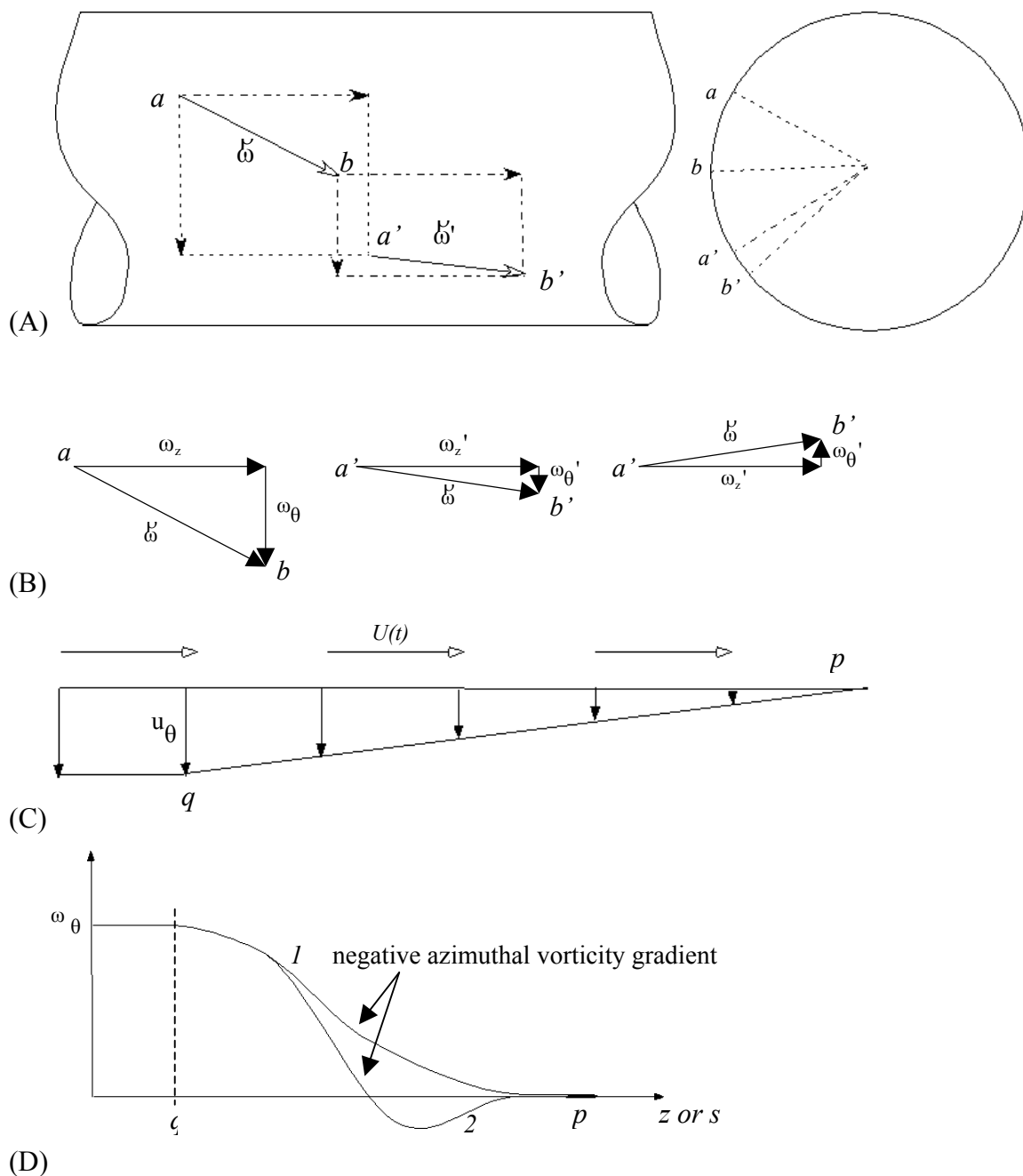
Figure 4-11: Elements of vorticity gradient generation

4.2.2   Movement of Negative Azimuthal Vorticity Gradient Region

As the region of initial radial expansion further expands, it extends upstream. This expanding region will continue to extend upstream and, eventually, will reach the point of steady circulation. At this location, the extending expansion region will further induce a negative azimuthal vorticity gradient. This behavior is shown in Figure 4-12. As the fluid particle at a radius r is pushed radially outwards to $r + \delta r$, the downstream end of $\overset{\nu}{\omega}$, *b*, is also radially displaced. At this point, the circulation is still a constant C_{max} value and therefore, the azimuthal velocity, u_θ, at point *b* is less than that at point *a*. This further causes a differential rate of spin, similar to the situation discussed in section 4.2.1. As a result of this differential rate of spin, the azimuthal component of the vorticity vector, at the next time step, is decreased:

$$u_{\theta b} < u_{\theta a}$$
$$\omega_\theta' < \omega_\theta$$
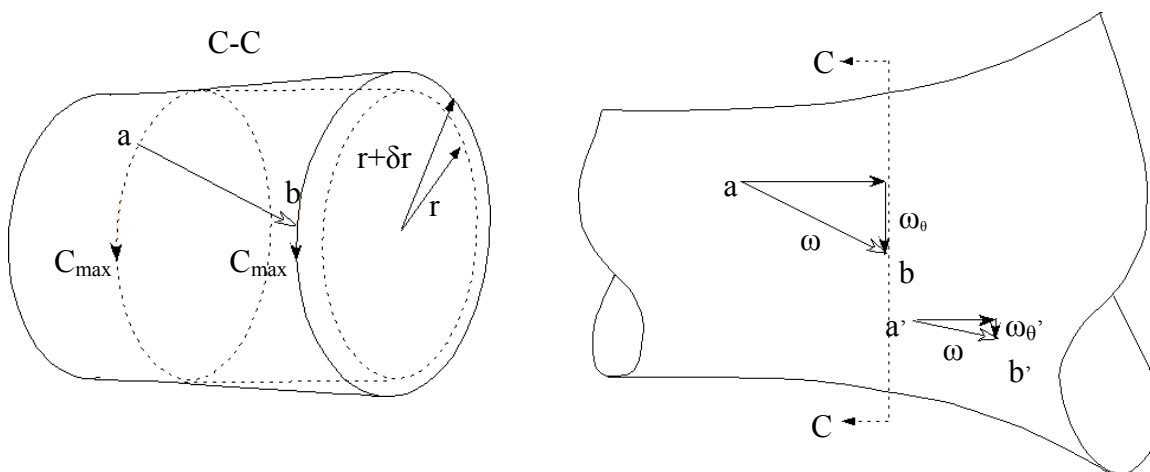
Figure 4-12: Elements of vorticity gradient movement

Relating back to the previous section, this decrease in the azimuthal component of vorticity, causes the negative vorticity gradient to shift further upstream toward the constant state region. This shift triggers the newly occupied region to radially expand, which then influences further upstream regions. Therefore as you can see, the feedback cycle continues and the negative vorticity gradient region repeatedly shifts upstream. Here by upstream shift, it is meant that the movement is relative to the downstream end

of the vortex. Since the vortex is convected downstream in reference to the absolute coordinate, the movement of the negative vorticity gradient region may be still in the downstream direction.

4.2.3   Supporting Simulation Results

The foregoing scenario indicates that radial expansion occurs in the region where the azimuthal vorticity gradient is negative. Furthermore, in a coordinate system moving the with the first vortex nodes, this negative vorticity gradient, and hence, region of radial expansion, continually shift upstream as time progresses. However, in order to justify this scenario, one needs more detailed numerical evidence. We can offer supportive computational evidence of the aforementioned claims with the use of the vortex-filament simulation. Using the results from the simulation, we are able to calculate and relate the values of the azimuthal vorticity, radial velocity, and azimuthal vorticity gradient as a function of axial distance. This information, gathered for T=0.21, is shown in Figures 4-13 and 4-14.
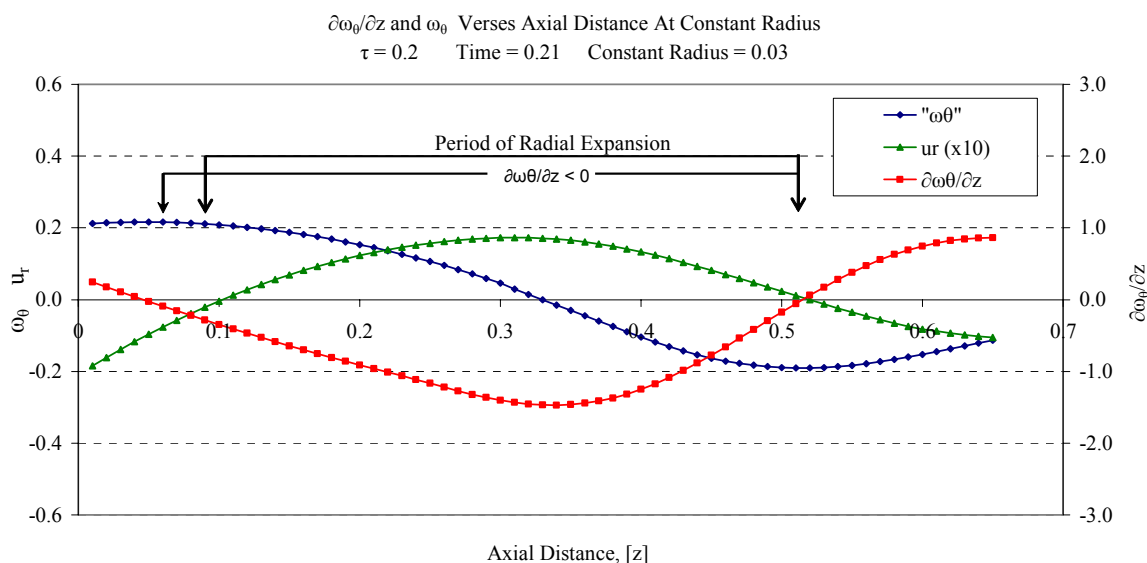
Figure 4-13: Azimuthal vorticity gradient at constant radius, T=0.21

$\partial\omega_\theta/\partial z$ and ω_θ Verses Axial Distance Along Projected Streamline
$\tau = 0.2$ Time = 0.21   R=0.03
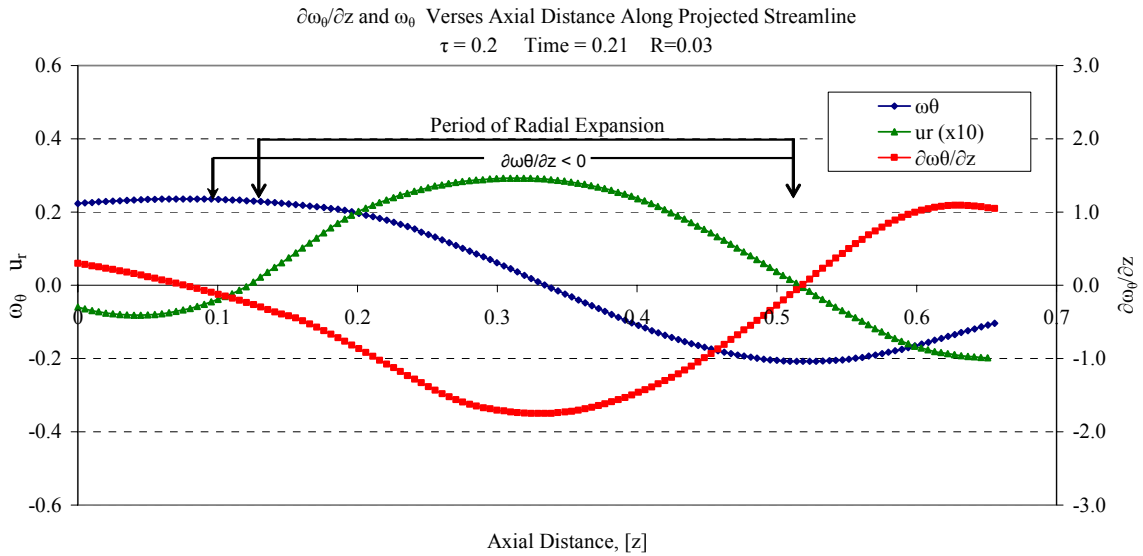
Figure 4-14: Azimuthal vorticity gradient along streamline, T=0.21

Since we are interested in the eventual control of vortex breakdown at the early transitive

stages, the early time of T=0.21 was selected. Additionally, this time is also noted as the

time when initial radial expansion is observed inside the vortex core. The difference

between the two figures is that values for Figure 4-14 were calculated for a constant

radial position of r=0.03, projected on the meridional plane , where as in Figure 4-15, the

values were calculated along the projected streamline initially emanating from r=0.03.

Regardless, both figures show a positive radial velocity for the majority of the negative

vorticity gradient region. In fact, the only slight difference occurs at the upstream end of

the negative vorticity region. At this location, there is a slight delay in the radial

expansion after the vorticity gradient obtains a negative value. This lag is not only small,

but expected when considering the numerically approximation of a two-phase flow. It is

also important to note that the maximum radial velocity occurs when the negative

vorticity gradient reaches a maximum negative value. The maximum occurs at

approximately z=0.35, which will be shown in the following to be located approximately

in the middle of the red section

        Similarly, we can use the simulation results to illustrate the continual upstream

shift of both the negative vorticity gradient and the resulting radially expanding region.

This upstream shift is illustrated in Figures 4-15 and 4-16. In both figures, the red region

is the region of changing circulation and the green region is the region of constant circulation. As you can see in Figure 4-16, the initial expansion at the outer edge of the vortex core, r=0.42, does not occur as early in the region of changing circulation and in time, as does the inner radius, shown in Figure 4-15. This is an effect of the expansion lag. The very onset of radial expansion occurs at the inner most radius and then propagates radially outwards. It is for this reason, that the r=0.42 radial shell does not experience any radial expansion until a short time after that of the inner most radius.
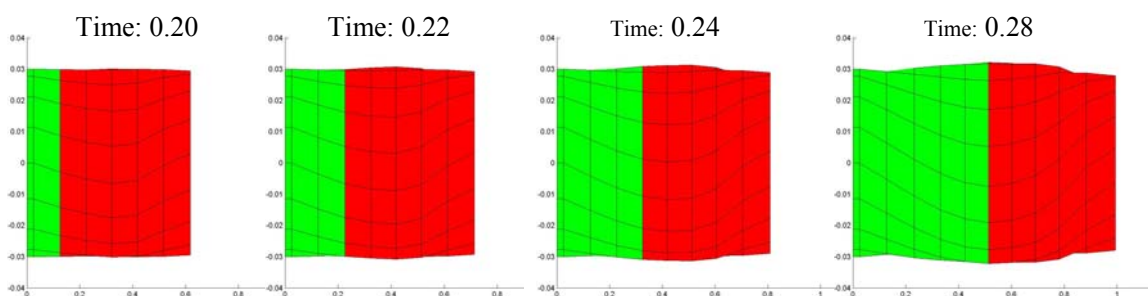
Figure 4-15: Movement of initial expansion, r=0.03
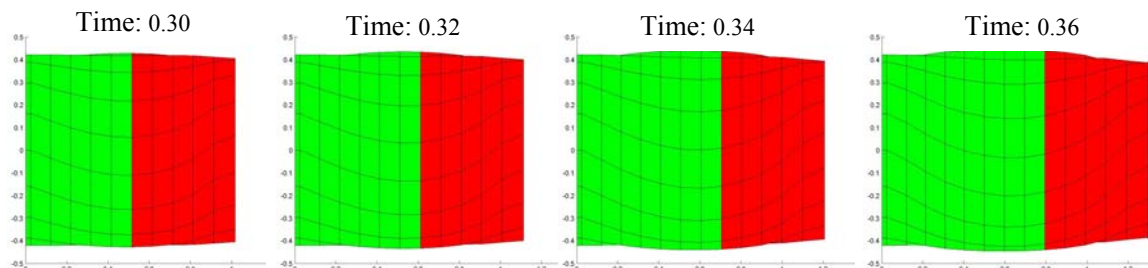
Figure 4-16: Movement of initial expansion, r=0.42

In the figures, it is also observed that as the radial expansion region moves from red region to green, or upstream in reference to the downstream end of the red region, so does the increasing curvature of the vortex streaklines, outlining the radial tube. This increasing bending represents the upstream movement of the negative vorticity gradient. As previously mentioned, the gradient and expansion region feed on each other. Therefore, as the radial expansion increases, moving upstream, so does the vorticity gradient and vice versa.

5   Quantitative Investigation

In this section, an equation displaying a simple dynamical relationship between the azimuthal vorticity gradient and curvature of the projected instantaneous streamline will presented in equation form. A method to numerically evaluate the individual terms in the equation will be then discussed. Finally, using the results from the vortex-filament simulation, the relationship will be validated computationally.

5.1   *Dynamic Relationship in Meridional Plane*

In the preceding chapter, it was shown that the initial expansion and subsequent growth of the vortex tube was induced by the global presence of a negative azimuthal vorticity gradient. As a complement to that qualitative investigation, we offer here a local and dynamical relationship between the azimuthal vorticity gradient at a particular location and the curvature of the instantaneous streamline, projected onto the meridional plane, at the same location. In the meridional plane, the streamline coordinates (s, n) are defined such that s is along and n is normal to the projected instantaneous streamsurface. For the remainder of this report, this projected surface will be referred to as the meridional streamline. These coordinates, along with their associated angles are shown in   Figure 5-1. Applying the inviscid equations of motion to this meridional coordinate system, one can show

$$\frac{\partial \omega_\theta}{\partial s} = \frac{1}{r_m^2}\frac{\partial r_m}{\partial t} + \frac{\partial}{\partial s}\left(\frac{C}{4\pi^2 r^2 q_m}\frac{\partial C}{\partial n}\right) - \frac{\partial}{\partial s}\left(\frac{1}{q_m}\frac{\partial H}{\partial n}\right) \tag{5-1}$$

where

$$\frac{\partial C}{\partial n} = 2\pi r \omega_m \cos \Phi_m \tag{5-2}$$

ω_θ is the azimuthal vorticity, t the time, r_m the radius of curvature of the meridional streamline, $q_m = \sqrt{u_r^2 + u_z^2}$, the meridional velocity, $\omega_n = \sqrt{\omega_r^2 + \omega_z^2}$, meridional vorticity, $C(r,z) = C(n,s) = 2\pi r u_\theta$, the circulation at the position z and at radius r,

$H = \dfrac{P}{\rho} + \dfrac{\overset{\text{o}}{u}^2}{2}$, the total head pressure and, Φ_m, the relative angle between ω_m and q_m.

The sign convention for r_m is also shown in Figure 5-1. Please refer to Appendix A for the step-by-step derivation of Equation (5-1).

If we assume the special case of steady-flow, the time-rate derivative term can be removed. Integrating the resulting equation in terms of s yields

$$\omega_\theta = \frac{C}{4\pi^2 r^2 q_m} \frac{\partial C}{\partial n} - \frac{1}{q_m} \frac{\partial H}{\partial n} .$$

(5-3)

This is reduced to the following if n is replaced with the stream function, ψ, by $dn = \frac{d\psi}{rq_m}$, the Bragg-Hawthorne equation:

$$\omega_\theta = \frac{C}{4\pi^2 r} \frac{\partial C}{\partial \psi} - r \frac{\partial H}{\partial n} .$$

(5-4)
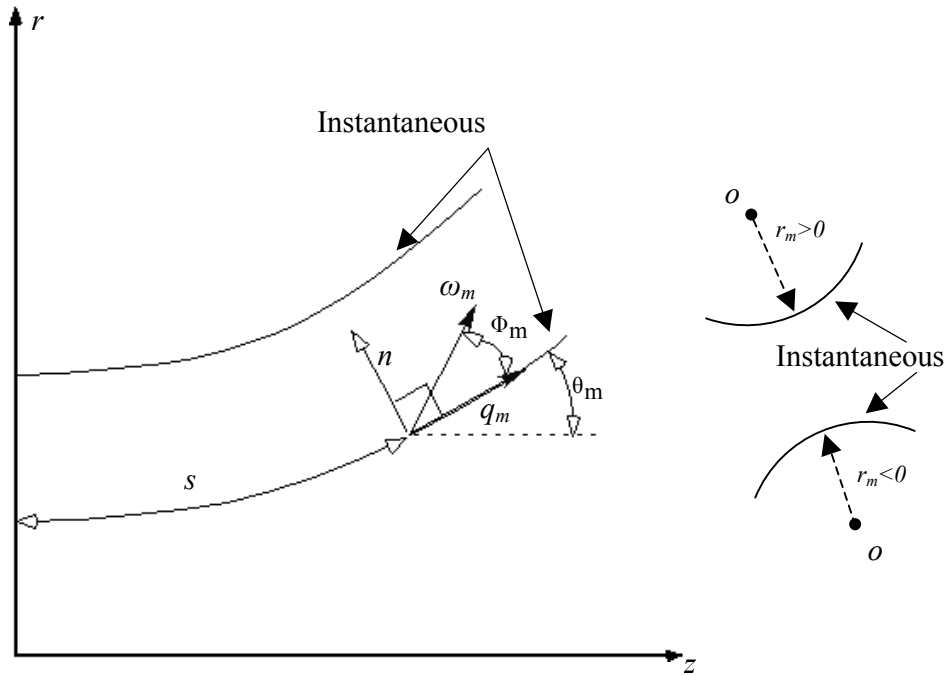
Figure 5-1: Streamline components in the projected meridional plane

In Equation (5-4), Brown and Lopez (*ref.* 10) noted that if circulation is held constant along the streamline, $\frac{\partial C}{\partial s} = 0$, such as in the steady-state case after ramp-up, then

$\dfrac{\partial C}{\partial \psi} = \dfrac{dC}{d\psi} = \dfrac{\omega_z}{w}$. This result corresponds to the case where the meridional vorticity

vector, ω_m is aligned with the meridional velocity vector, q_m, or simply $\Phi_m = 0$.
Utilizing this alignment, they obtained an explicit expression showing that the
competitive relationship between the two right-hand-side terms in Equation (5-3) could
result in a negative ω_θ value when the streamsurface diverges. Brown and Lopez were
the first to point out the prominent role of the azimuthal sign-switch in the region of
radial expansion. Brown and Lopez's argument gives compelling insight in the steady-
state scenario. However, it fails to offer any explanation into the commencement of the
radial expansion or creation of the azimuthal vorticity gradient, both of which are
prevalent and materialize during the formative stages of breakdown.

Returning to the present unsteady transient case, we rewrite Equation (5-1) as

$$\frac{\partial \omega_\theta}{\partial s} = -\frac{\partial}{\partial t}\left(\frac{1}{r_m}\right) + \alpha_c + \alpha_H \tag{5-5}$$

where

$$\alpha_c = \frac{1}{8\pi^2}\frac{\partial}{\partial s}\left(\frac{1}{r^2 q_m}\frac{\partial C^2}{\partial n}\right) \qquad \alpha_H = -\frac{\partial}{\partial s}\left(\frac{1}{q_m}\frac{\partial H}{\partial n}\right)$$

In this compact form, α_c and α_H are equivalent to the latter two terms in Equation (5-1)
respectfully. In the transient case, these two terms can become very small in general

when the dimensionless parameter, $B = \dfrac{(C_{\infty max})^2 \tau}{4\pi^2 r_c^3 U_\infty}$ is small. In the definition of this

parameter, $C_{\infty max}$ refers to the maximum total circulation, r_c is the vortex core radius, τ
is the circulation/velocity ramp-up time, and U_∞ is the freestream or convected velocity.
The value of B becomes smaller, for instance, as you decrease the ramp-up time. By
making the assumption that conditions exist such that B is small, Equation (5-5) can be
further reduced.

$$\frac{\partial \omega_\theta}{\partial s} = -\frac{\partial}{\partial t}\left(\frac{1}{r_m}\right) = \frac{1}{r_m^2}\left(\frac{\partial r_m}{\partial t}\right) \tag{5-6}$$

Equation (5-6) is a simple expression, which affords a direct relationship for the azimuthal component of a complex three-dimensional vorticity vector at a particular location, in terms of the streamline curvature at that same location. Equation (5-6) infers that the change in the azimuthal vorticity along the meridional streamline has the same sign as the temporal change in the radius of curvature, r_m. Therefore, once radial expansion commences in the region of negative azimuthal vorticity, $\frac{\partial \omega_\theta}{\partial s} < 0$, and

$r_{m1} > 0$, it continues to expand such that the meridional streamline becomes more curved with time, $r_{m2} < r_{m1}$. This fact supports our initial argument that the negative vorticity gradient not only initiates the radial expansion, but also, feeds its subsequent growth. On the contrary, in the region of a positive gradient, $\frac{\partial \omega_\theta}{\partial s} < 0$, and $r_{m1} < 0$, the streamline continues to flatten and level toward horizontal with time. In this later case, the subsequent streamline is marked by a larger radius of curvature, $r_{m2} > r_{m1}$. The difference between continual flattening (b), and increasing curvature (a), is illustrated in Figure 5-2.
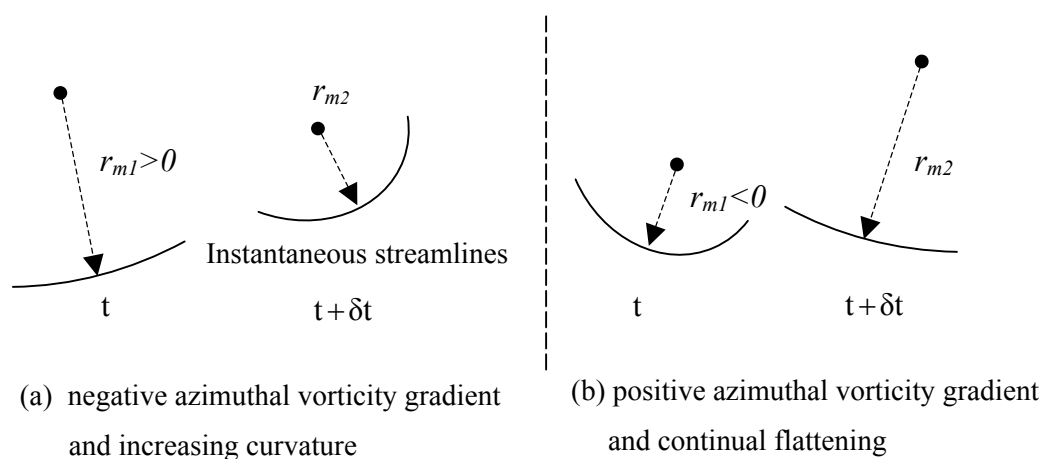
Figure 5-2: Temporal change in streamline curvature

5.2   Inclusion of the α_c Term

In the previous section, we presented the fact that if the B parameter was small, we could neglect the contributions of the α_c and α_H terms in the Equation (5-5). However, since the value of B is not particularly small for our baseline case, B=15, we will elect to retain this term for completeness. In addition, by calculating the values for, and investigating the trends of, α_c, we will gain additional understanding into the dynamics of the flow. On α_H, even though it is possible to have a gradient of H in inviscid flow from the following equation,

$$\frac{DH}{Dt} = \frac{1}{\rho}\frac{\partial P}{\partial t}$$

we will, however, choose to neglect α_H. The reason is that we are describing the vortex breakdown in the language of incompressible vortex dynamics, where pressure terms do not appear explicitly.

The strong variation of $\dfrac{\partial C}{\partial n}$ appearing within the α_c term can be seen in Figure 5-3. In this figure, a series of contour plots of local circulation (τ=0.20) is overlaid with assorted instantaneous streamlines (emanating initially at r=0.03, r=0.18, r=0.36).
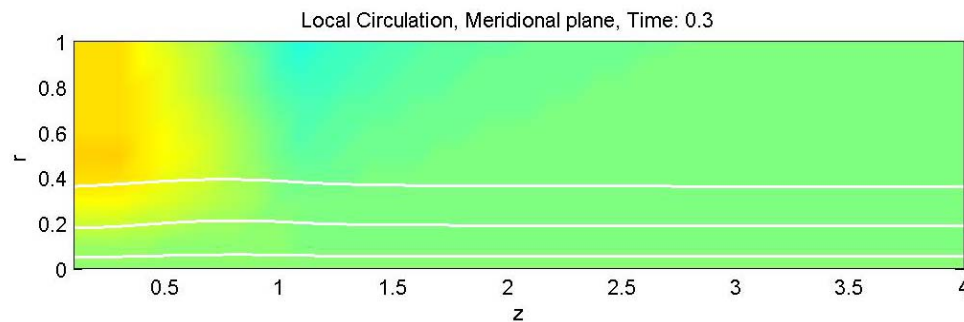
Figure 5-3: Local circulation and projected streamlines, τ=0.20
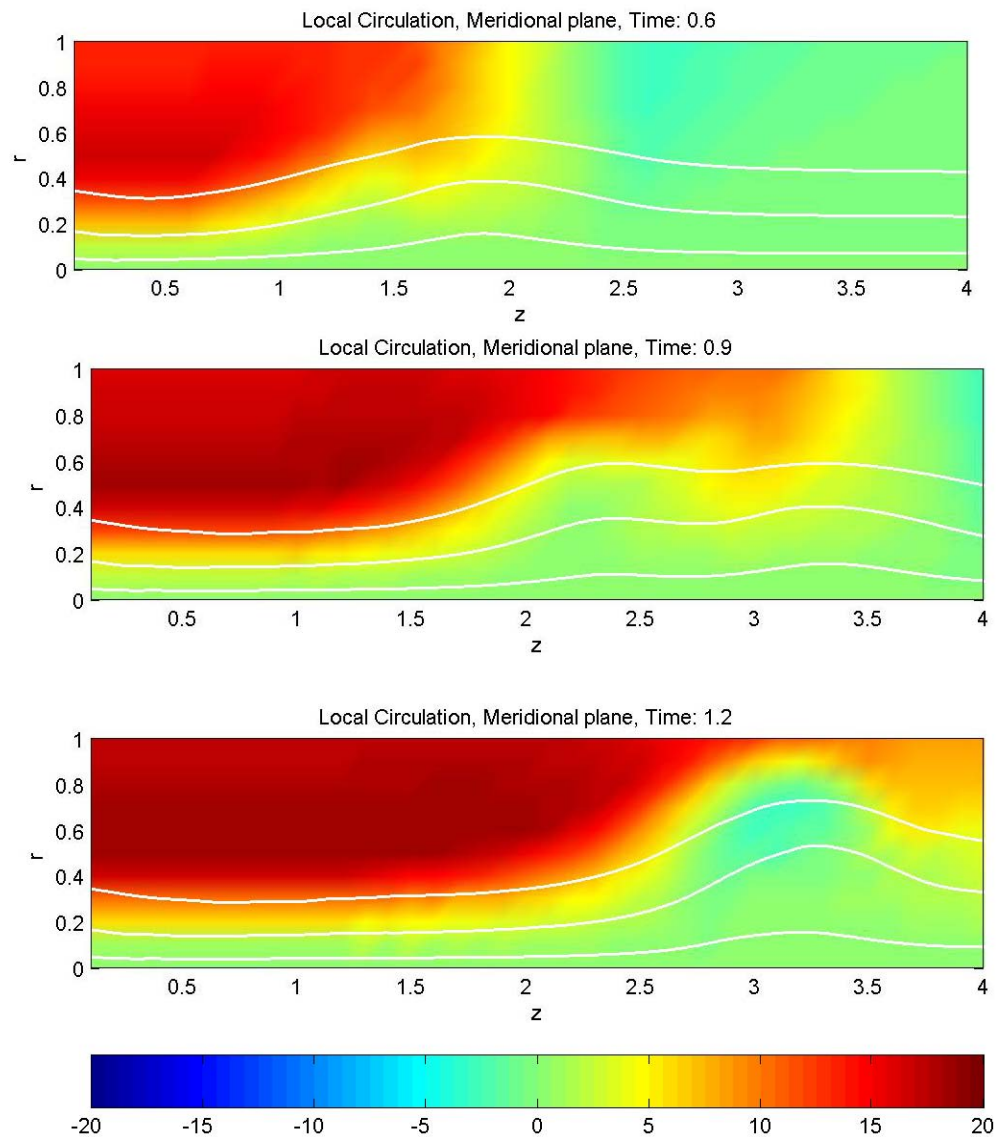
Figure 5-3 (cont.)

As you can see in the figure, there is a substantial change in circulation normal to the streamlines inside the vortex core region (r=0). On the contrary, as you move away from the core, the circulation change decreases rapidly. This fact confirms that, similar to a Rankine vortex, the flow field outside of the core can be considered irrotational and the circulation attains a constant value. However, near the core, it is clearly evident that we can not neglect the change in circulation normal to the streamline, and therefore, can not neglect the α_c term in Equation 5-5.

If we are to numerically calculate the value of α_c, we need to first express the

$\dfrac{\partial C}{\partial n}$ term, within the α_c equation, in terms of the meridional trigonometry. By doing so,

we avoid having to numerically take a partial derivative of a partial derivative, which can

prove to be both time consuming and computationally taxing. Starting with the

divergence-less property of vorticity and using streamline coordinate trigonometry, one

can determine an expression for this change in local circulation normal to the streamline,

$\dfrac{\partial C}{\partial n} = 2\pi r \omega_s$. This can be rewritten as Equation (5-2), from which one can derive the

following expression:

$$\alpha_C = \frac{\partial}{\partial s}\left(\frac{u_\theta \omega_m \cos \Phi_m}{q_m}\right) \tag{5-7}$$

The complete derivative of Equation (5-7) is shown in Appendix B. Substituting this

expression into Equation (5-5) gives the final dynamic relationship equation,

$$\frac{\partial \omega_\theta}{\partial s} = -\frac{\partial}{\partial t}\left(\frac{1}{r_m}\right) + \frac{\partial}{\partial s}\left(\frac{u_\theta \omega_m \cos \Phi_m}{q_m}\right) \tag{5-8}$$

5.3 *Dynamic Relationship Computation*

Up to this point, we have only derived the dynamic equation relating the

azimuthal vorticity and a change in the shape of a streamline at a particular location.

However, with the use of the vortex-filament method, we can computationally validate

this relationship expressed in Equation (5-8) by calculating both sides of the equation. In

order to illustrate the influences of the two right hand side terms in Equation (5-8), we

will calculate their respective values independently.

5.3.1 *Time rate of change in radius of curvature (r_m)*

The first step in validating Equation (5-8) is to calculate the time rate of change in

the radius of curvature at a particular point along a given streamline. This is achieved by

first projecting the meridional streamline from the three-dimensional stream surface. An

example of the projected streamline is represented by the white lines in Figure 5-4 below, which also shows azimuthal vorticity on the meridional plane.
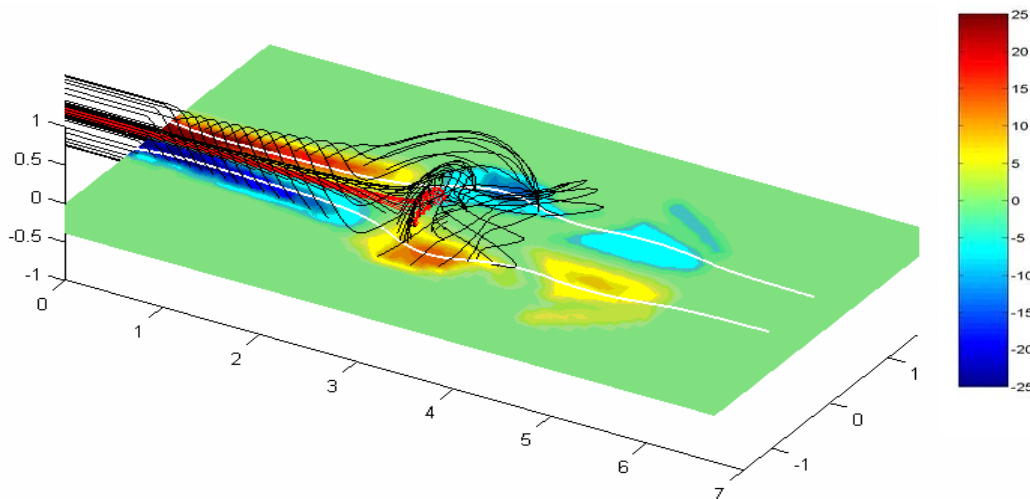
Figure 5-4: Azimuthal vorticity and streamline projection, meridional plane, T=1.2

Once the desired streamline, at time t, is obtained, a position along the streamline, such as point P in Figure 5-5, is selected and a new streamline at some later time, t + δt, which passes through P, is determined. In this case, since we are taking a time derivative, the spatial point of interest, P, must remain unchanged. We then calculate the difference in radii of curvature at P of the two streamlines, per unit time, δt..
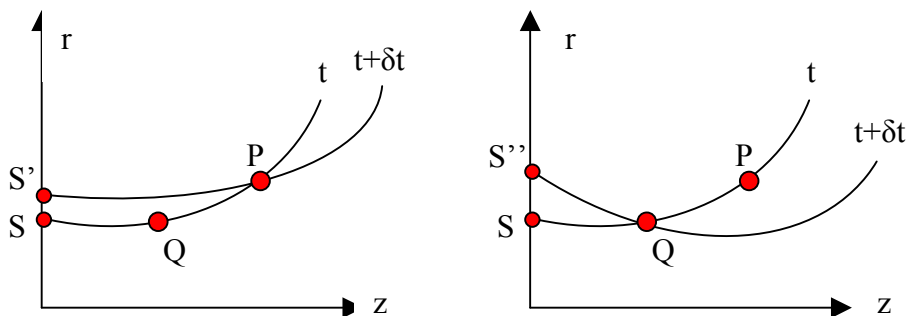
Figure 5-5: Illustration of the radius of curvature method: theoretical

As can be seen Figure 5-5, the streamline passing through point P at t + δt is not necessarily the same streamline passing point Q at t + δt; therefore, the two streamlines originate from different points, S and S'', at the vorticity source. Similar to a schematic

sketch of Figure 5-5, Figure 5-6 illustrates this streamline relationship in terms of our simulation results.
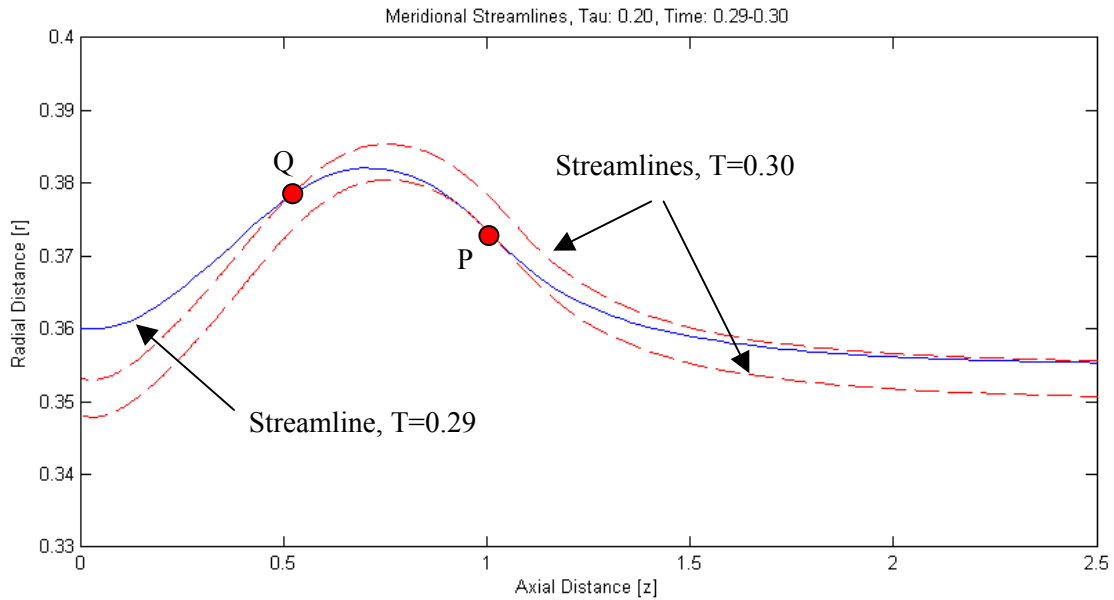
Figure 5-6: Illustration of radius of curvature method: simulation results

This process is then performed for all points along the original streamline. Therefore, if there are n number of points along the original streamline, n+1 total streamlines must be calculated to determine the time rate of change in radius of curvature along the entire length of the original streamline. It is also extremely important to note that our projected meridional streamline is determined computationally and thus, composed of a finite number of discretized points and must be smoothed as best as possible to avoid infinite radii of curvatures values. If, in fact, the streamline is not smoothed adequately, a particular point of interest, such as P or Q in Figure 5-6, may fall on a perfectly straight line discretized segment, leading to an infinite radius of curvature. For this investigation, a cubic-spline smoothing method was applied to smooth all streamlines, prior to calculating any radius of curvature. Additionally, to avoid excessively large r_m values, such as $r_m \rightarrow \infty$ corresponding to near-straight line curvature, $\dfrac{1}{r_m}$, will be used instead of r_m. An illustration of the meridional streamlines and the solid rendering of the vortex tube are shown in the Figure 5-7 (top). These same streamlines, now denoted in white,

are further shown superimposed onto the azimuthal vorticity field along the meridional plane (middle). Lastly, the bottom of Figure 5-7 illustrates the plots of curvature verses axial distance for both streamline (a) and (b).

Azimuthal Vorticity, Meridional Plane, T=0.30

One Over Radius of Curviature as a Function of Axial Distance, Time=0.3
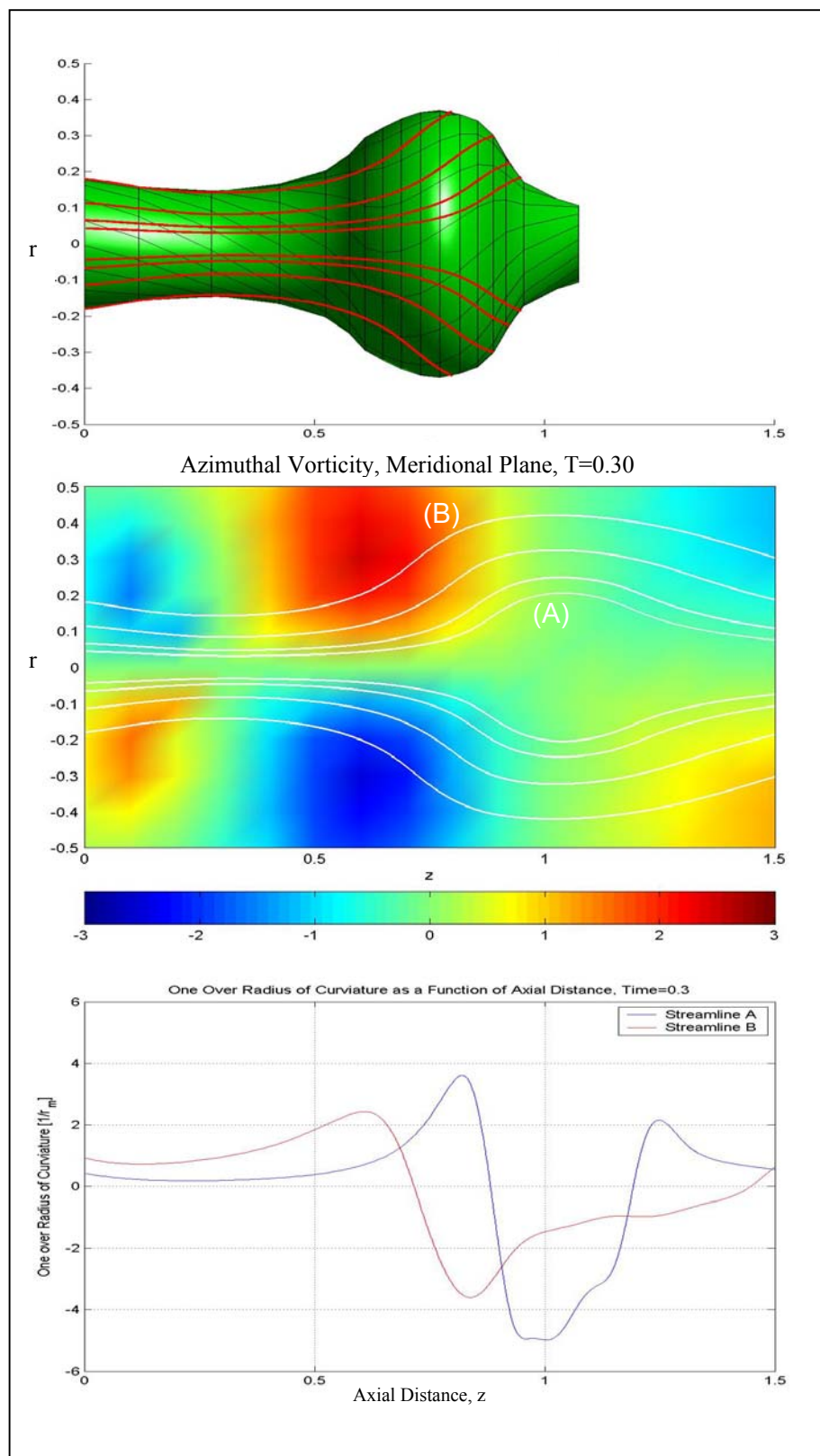
Figure 5-7: Radius of curvature for projected streamlines, τ=0.005, T=0.3

5.3.2 α_c *term calculation*

Unlike the radius of curvature, the calculation of α_c along a specific streamline, at time t, is much easier. In this case, since we are taking a spatial derivative along streamwise distance, s, time remains fixed. As a result, only one streamline is needed. Knowing all the physical parameters, we can calculate the value of

$$\frac{u_\theta \omega_m \cos \Phi_m}{q_m}$$

appearing in Equation (5-7) for all points on the desired streamline; and we further calculate the spatial derivative along the streamline using a center-spaced differencing scheme. Figure 5-8 and Figure 5-9 show the value of α_c as a function of axial distance for various projected streamlines, at T=0.3.
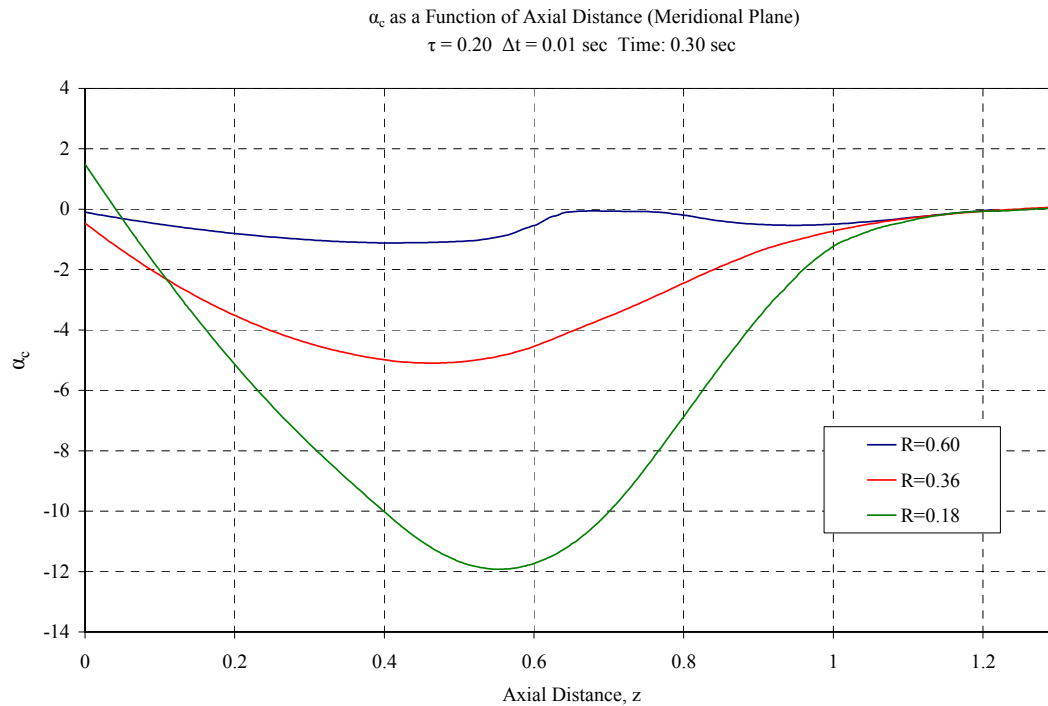
Figure 5-8: α_c as a function of axial distance, τ=0.20, T=0.30

α_c as a Function of Axial Distance (Meridional Plane)
$\tau = 0.005 \quad \Delta t = 0.01 \text{ sec} \quad \text{Time: } 0.30 \text{ sec}$
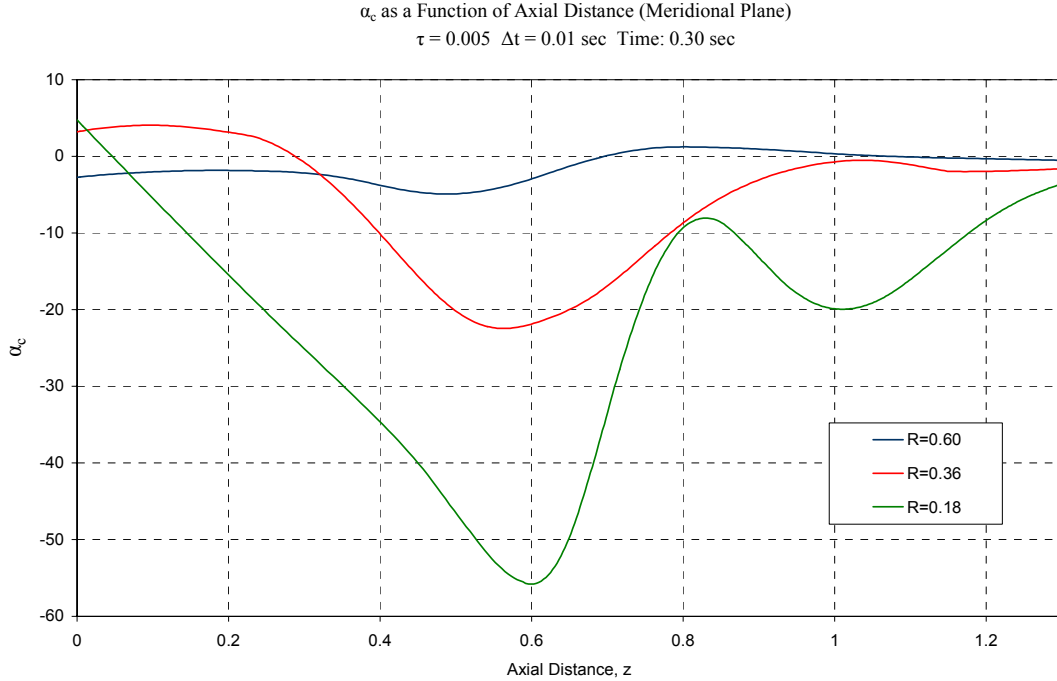
Figure 5-9: α_c as a function of axial distance, τ=0.005, T=0.30

As shown in both figures, the value of α_c along a streamline dramatically increases as you move inside of the vortex core. Similarly, as shown in Figure 5-9, the value of α_c for all streamlines also increases as you decrease the circulation ramp-up time. We would expect this correlation between α_c and decreased ramp-up time, since a faster ramp-up would create a stronger vorticity gradient, initially at such an early time of T=0.30. However, this increase in α_c with reduced ramp-up time does not mean that α_c terms in Equation (5-8) become more predominant in comparison to the first term on the right-hand side, $-\dfrac{\partial}{\partial t}\left(\dfrac{1}{r_m}\right)$. In fact, as the ramp-up time decreases, the $\dfrac{\partial}{\partial t}\left(\dfrac{1}{r_m}\right)$ terms become more dominant, as the preceding argument on the B-parameter suggests; this point will be confirmed in 5.3.4.

5.3.3 $\frac{\partial \omega_\theta}{\partial s}$ *term calculation*

To calculate the $\frac{\partial \omega_\theta}{\partial s}$ term, we superimpose the meridional streamline onto the meridional cut of azimuthal vorticity, ω_θ, shown in the plots of section 3.2.1. Examples of the streamline projections and meridional cut of azimuthal vorticity are shown in Figure 5-4 and Figure 5-7. We then extrapolate the values of ω_θ for every point along the streamline, and as we did in determining α_c, using a center-spaced differencing scheme to calculate the spatial derivative of azimuthal vorticity along the streamline.

5.3.4   *Numerical results*

Having calculated all the terms, the two sides of Equation (5-8) can be equated and compared for various ramp-up times, τ. A sample result is illustrated in the following graphs. Figure 5-10, 5-11, and 5-12 illustrate the validation of Equation (5-8) along three different streamlines (initially originating at r=0.18, r=0.36, and r=0.60 respectfully) at T=0.30 for τ=0.20. In the graphs, the left side of Equation (5-8), $\frac{\partial \omega_\theta}{\partial s}$, is represented by the black dotted line averaged over the two successive time interval T=0.29 and T=0.30.

Average $\partial\omega_\theta/\partial s$ Verses $-\partial/\partial t$ [1/rm] along Meridional Plane
$\tau = 0.20$ $\Delta t = 0.01$ sec   Time Range: 0.29-0.30 sec
Original Streamline, r = 0.18
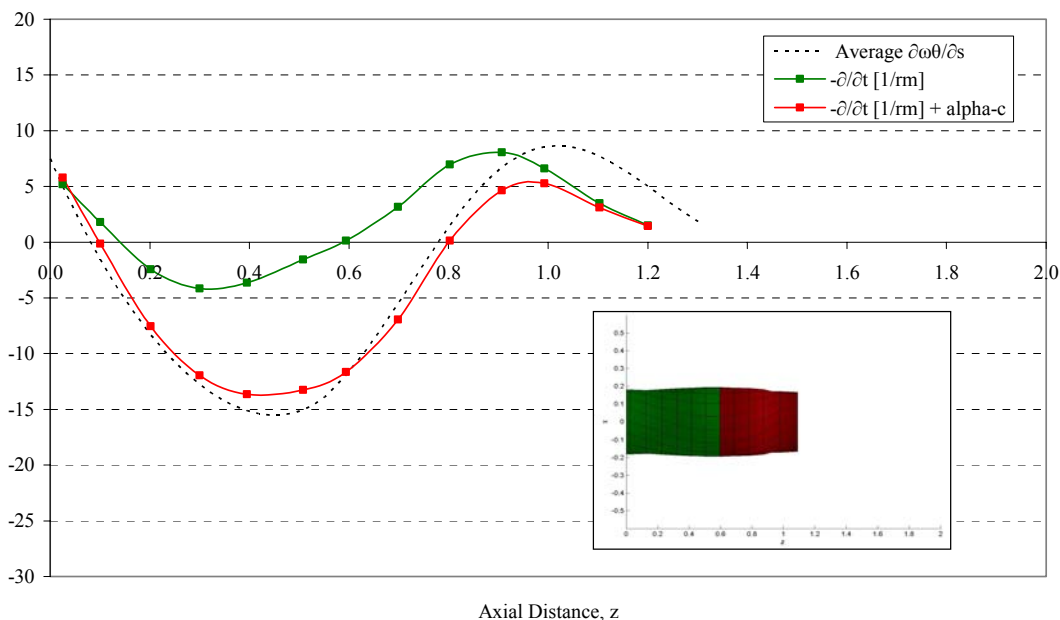
Figure 5-10: $\partial\omega_\theta/\partial s$ verses axial distance, r=0.18, τ=0.20, T=0.30

Average $\partial\omega_\theta/\partial s$ Verses $-\partial/\partial t$ [1/rm] along Meridional Plane
$\tau = 0.20$ $\Delta t = 0.01$ sec   Time Range: 0.29-0.30 sec
Original Streamline, r = 0.36
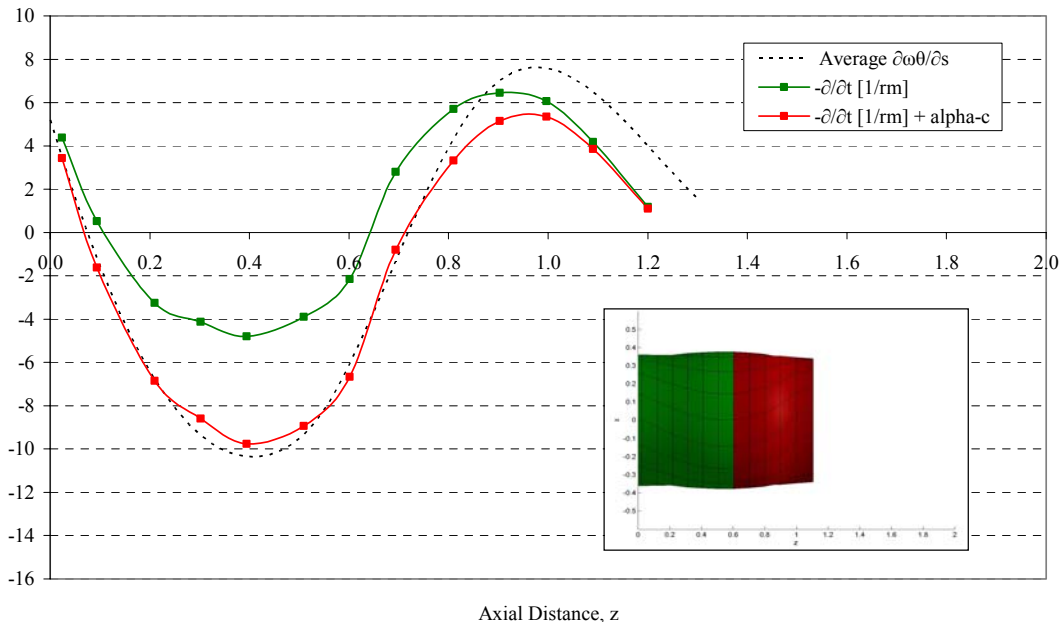
Figure 5-11: $\partial\omega_\theta/\partial s$ verses axial distance, r=0.36, τ=0.20, T=0.30
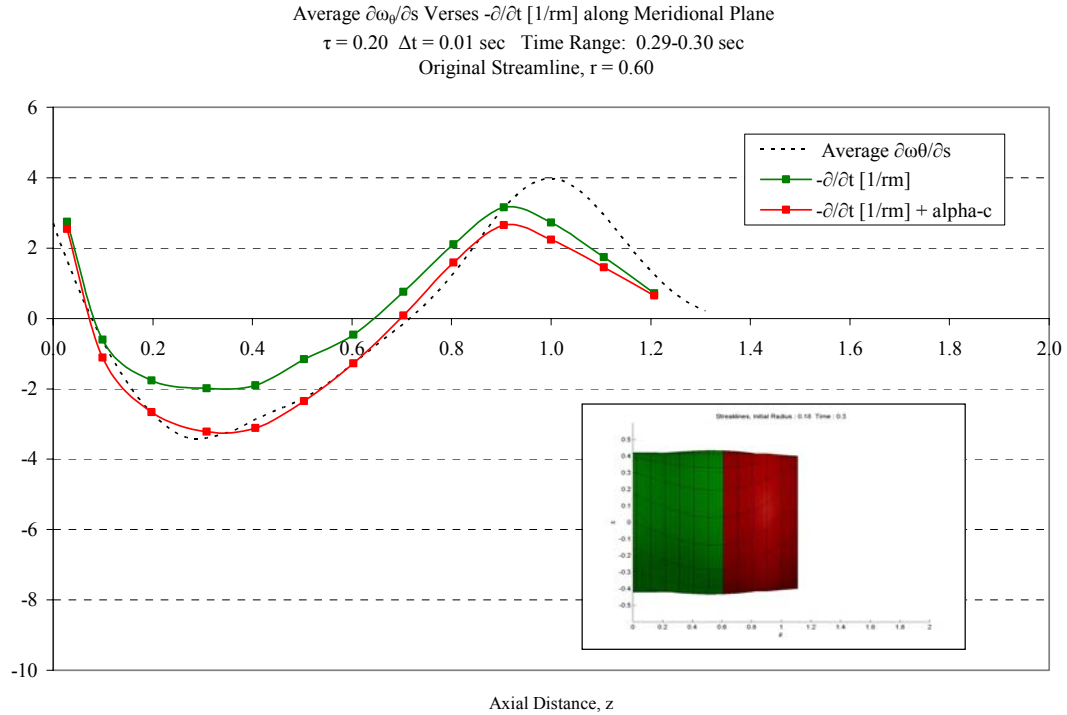
Figure 5-12: $\partial\omega_\theta/\partial s$ verses axial distance, r=0.60, τ=0.20, T=0.30

The green line refers to the value of $-\dfrac{\partial}{\partial t}\left(\dfrac{1}{r_m}\right)$ only, where the red line refers to the sum

of $-\dfrac{\partial}{\partial t}\left(\dfrac{1}{r_m}\right)$ and α_c . By distinguishing between these two lines, as proposed, we are able

to isolate the individual effects of two terms on the right-hand side. Additionally, a

subplot of the solid rendering of the respective vortex tube is offered in each graph to

associate the value of $\dfrac{\partial\omega_\theta}{\partial s}$ at particular locations with regions of radial expansion and

contraction. As mentioned earlier, a positive $\dfrac{\partial\omega_\theta}{\partial s}$ value indicates a region of radial

contraction and a negative $\dfrac{\partial\omega_\theta}{\partial s}$ value indicates a region of radial expansion. Similar to

all previous solid renderings, the red region refers to the region of changing circulation.

From the graphs, it is quite evident that the results from the vortex-filament

method produce a good agreement between the two sides of Equation (5-8). As expected,

the influence of α_c is not trivial and also shown to decrease with increasing radial distance. In fact, for the r=0.60 streamline case, represented in Figure 5-12, the $-\dfrac{\partial}{\partial t}\left(\dfrac{1}{r_m}\right)$ term alone provides a good approximation to $\dfrac{\partial \omega_\theta}{\partial s}$. Although the general profiles of the red line and dotted black line match well in all three graphs, we must be more concerned, from a controls perspective, with the agreement in the sign of the values, specifically at the downstream location where $\dfrac{\partial \omega_\theta}{\partial s} = 0$. This location marks the transition from radial expansion to contraction, which corresponds to the similar change depicted by the vortex streaklines in the solid rendering subplots. As also observed in the graphs, the agreement of this transition location, between both sides of Equation (5-8), improves with the addition of α_c and as you extend out radially from the vortex core. In general, the agreement between the values of $\dfrac{\partial \omega_\theta}{\partial s}$, which is determined using the Biot-Savart law, and the dynamic relationship is quite favorable, especially considering the simplicity of Equation (5-8). We must not, however, forget to note the slight difference in values towards the downstream end of the vortex tube. This difference may be the result of not accounting for the head pressure effects, contained in the α_H term.

Figures 5-13, 5-14, and 5-15 show the same comparison as the previous three graphs but for a faster ramp-up, τ=0.005. All the trends observed in the previous τ=0.20 case are also seen in the τ=0.005 case. In fact, the additive effect of α_c appears to decrease faster with increasing radial distance, at the faster ramp-up time. This trend is exactly what the B parameter suggested earlier. In addition, the faster ramp-up case shows better agreement between the two sides of Equation (5-8), particularly at the downstream end of the vortex tube. In keeping with the head pressure argument, this improvement at the downstream end would suggest that the head pressure effects diminish with decreasing ramp-up time value. However, before such an argument can be confirmed, future cases that include α_H must be investigated.
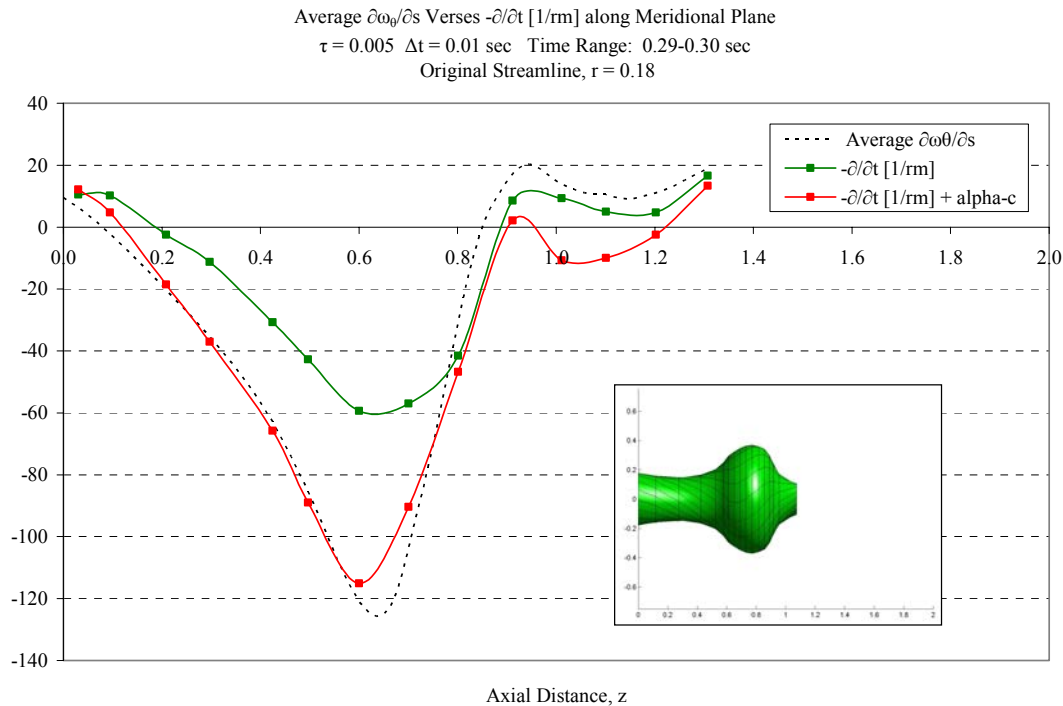
Figure 5-13: $\partial\omega_\theta/\partial s$ verses axial distance, r=0.18, τ=0.005, T=0.30
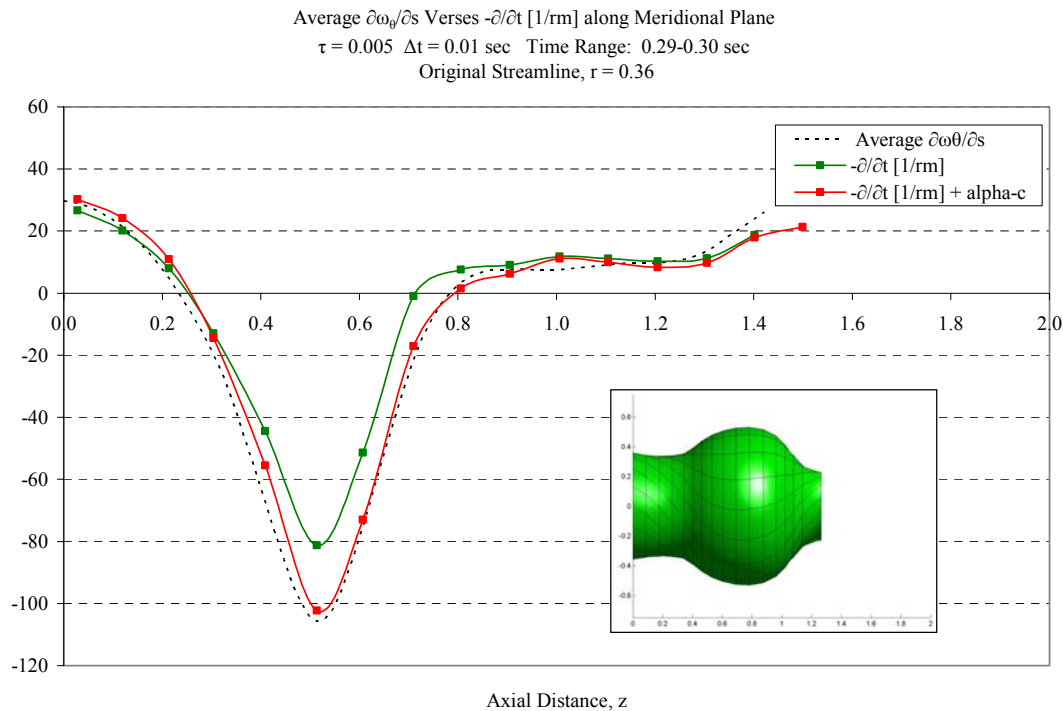
Figure 5-14: $\partial\omega_\theta/\partial s$ verses axial distance, r=0.36, τ=0.005, T=0.30

Average $\partial\omega_\theta/\partial s$ Verses $-\partial/\partial t$ [1/rm] along Meridional Plane
$\tau = 0.005 \quad \Delta t = 0.01$ sec Time Range: 0.29-0.30 sec
Original Streamline, r = 0.60
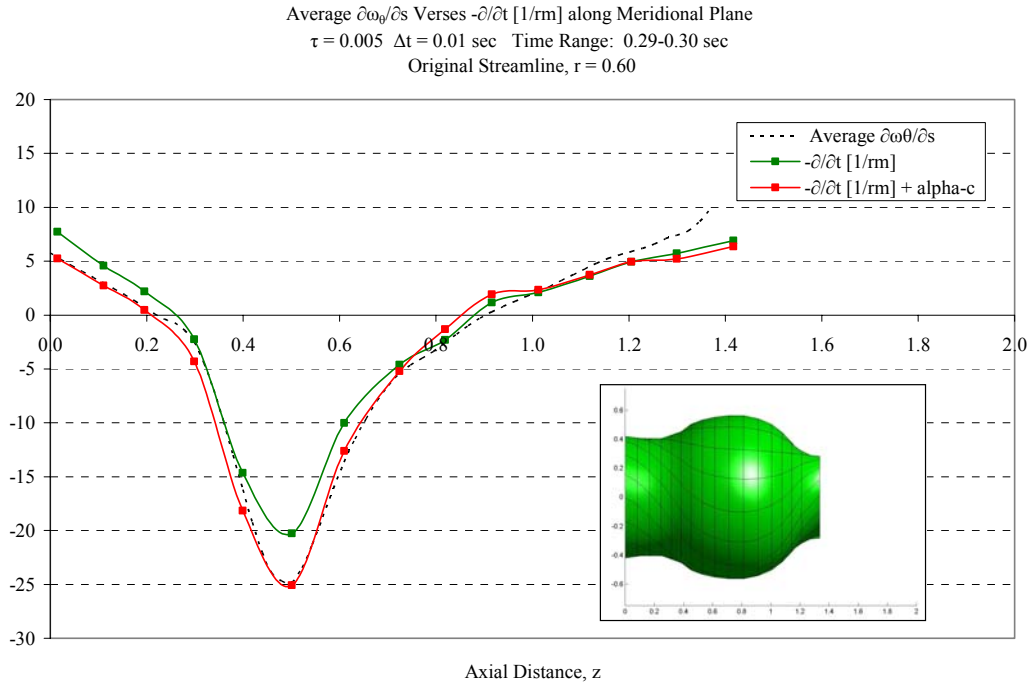
Figure 5-15: $\partial\omega_\theta/\partial s$ verses axial distance, r=0.60, τ=0.005, T=0.30

In summary, the vortex-filament simulation successfully validates the dynamic relationship expression, as well as all findings originating from Equation (5-8). Most important, a simple method to calculate the azimuthal component of the complex three-dimensional vorticity vector in terms of the temporal change in streamline curvature has been identified. A general overview of this relationship and its implications are shown in Figure 5-16. In this figure two scenarios are shown. The top of Figure 5-16 shows two identical plots of $\dfrac{\partial\omega_\theta}{\partial s}$ verses axial distance for τ=0.20 at T=0.30. On this curve two points have been highlighted: point P with positive curvature belonging to $\dfrac{\partial\omega_\theta}{\partial s} < 0$ and point Q with negative curvature belonging to $\dfrac{\partial\omega_\theta}{\partial s} > 0$. Below both plots, the time evolution of both the streamline and solid rendering are shown for T=0.30 to T=0.40. As you can see on the left, the radius of curvature at point P along the streamline increases from T=0.30 to T=0.40, signaling a region of radial expansion. On the contrary, the radius of curvature at Q, shown on the right of the figure, becomes less negative

$(\left|r_{m1}\right| > \left|r_{m2}\right|)$ with time, signaling radial contraction. The expansion and contraction

behavior at P and Q, respectively, is confirmed by the superimposed solid renderings.
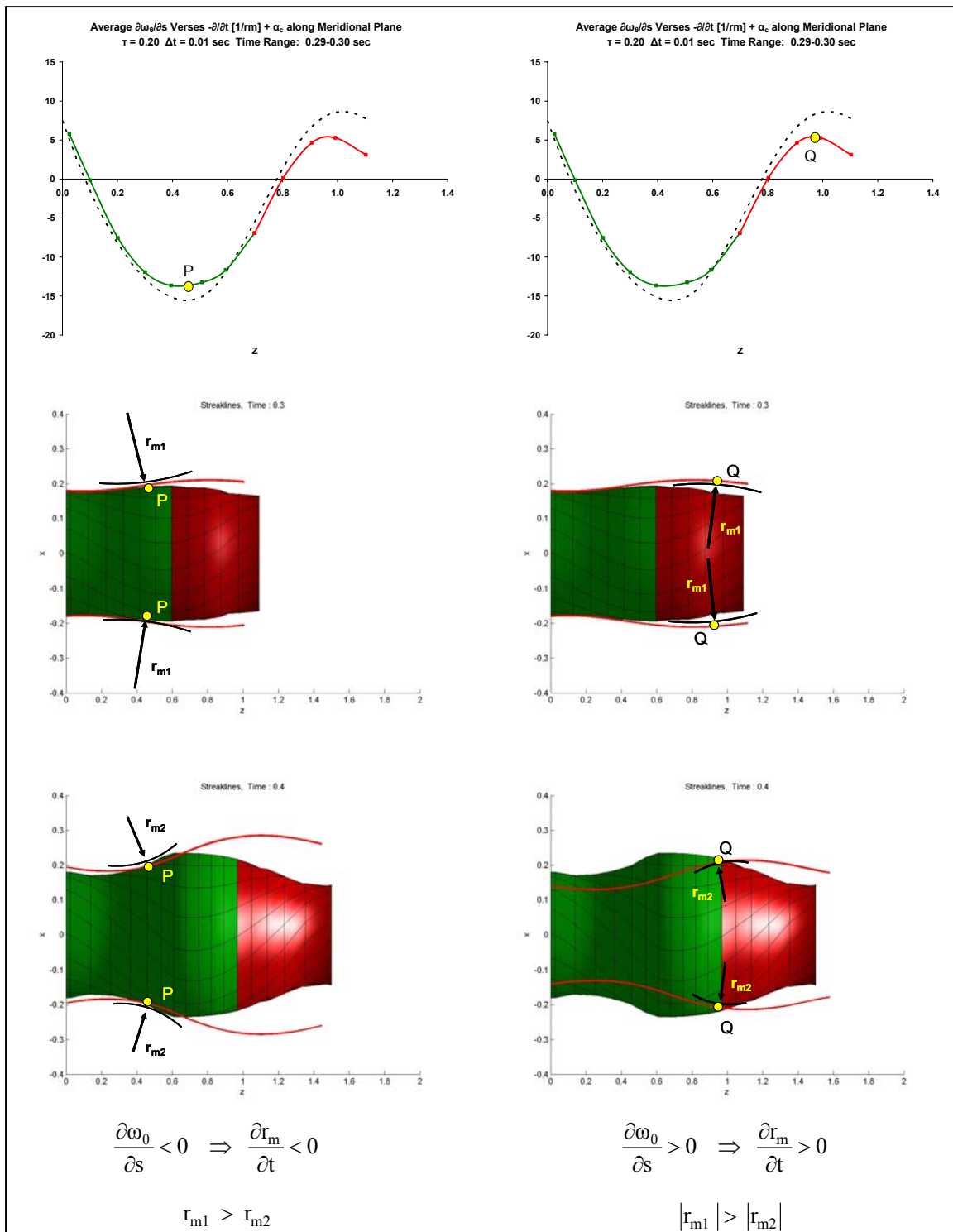
Figure 5-16: Overview of dynamic relationship expression

6   Steadiness Investigation

In this section we will numerically trace the helical angles of velocity and vorticity as the vortex tube transients downstream. The results will be presented in a temporal evolution form and will give further insight into the features of the swirling vortex tube. Additionally, using a steady state equation offered by Brown & Lopez, we will attempt to assess the steadiness of our transient simulation by comparing the vorticity profile along a respective streamline with that predicted by the steady state equation

6.1   Helical Angles Calculation

In modifying the present vortex-filament method, we determined for the helical angles of vorticity at its source based on the prescribed $\dfrac{\alpha}{\beta}$ value of 1.5. These angles are a function of both radial distance and time: $\alpha = \dfrac{u_\theta}{u_z} = \dfrac{C_\infty(t)\left(1 - e^{-br^2}\right)}{2\pi r U_\infty(t)}$. However, if the velocity at any time is proportional to that of the circulation, $C_\infty(t) \propto U_\infty(t)$, as is the case with our baseline calculation, the time dependency falls out and the helical value becomes only a function of radial distance. The helical angle approaches zero at both the center of the vortex core and at the far field radial boundary.   These helical angles, shown in Table 6-1, are then applied to the discretized radial locations at the vorticity source. As you can see from the values in the below table, the helical angle appears to reach a maximum at the approximate edge of the vortex core (r=0.30) and slowly decrease as you extend out from this edge. Likewise, the helical angle also decreases as you approach the centerline of the vortex core, however, at a much faster rate. Although we explicitly specify the initial helical angle at the vorticity source, the helical angle is free to develop on its own as the vortex tube transients downstream from the source, depending on the velocity induced by the vortex filaments at every radial location within the vortex tube.

Table 6-1: Prescribed helical angle at vorticity source, z=0

Radial Location	Helical Angle, deg
r = 0.03	29.1
r = 0.06	35.9
r = 0.08	42.5
r = 0.12	49.3
r = 0.18	56.8
r = 0.24	58.8
r = 0.30	59.3
r = 0.36	56.9
r = 0.42	53.6

The vortex-filament method affords us not only the ability to physically trace the helical angle of vorticity, but the ability to numerically determine both the helical angle of vorticity and velocity as a function of downstream location by tracking the relationship between their respective axial and azimuthal components. With the use of these axial and azimuthal components, we are able to view the temporal evolution of the tangent of the helical angle of velocity, α, and that of the angle of vorticity, β. This temporal evolution of angles, at constant radial cuts within the vortex core, is shown in Figure 6-1.
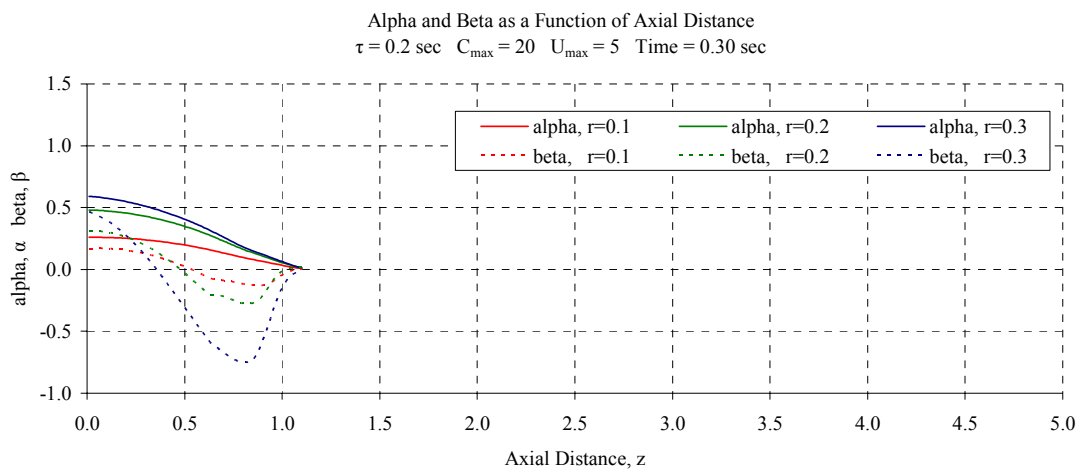
Figure 6-1: Temporal evolution of the tangent of helical angle of velocity and vorticity

Alpha and Beta as a Function of Axial Distance
$\tau = 0.2$ sec $C_{max} = 20$ $U_{max} = 5$ Time = 0.60 sec

Alpha and Beta as a Function of Axial Distance
$\tau = 0.2$ sec $C_{max} = 20$ $U_{max} = 5$ Time = 0.90 sec

Alpha and Beta as a Function of Axial Distance
$\tau = 0.2$ sec $C_{max} = 20$ $U_{max} = 5$ Time = 1.20 sec

Figure 6-1 (cont.)

Alpha and Beta as a Function of Axial Distance
$\tau = 0.2$ sec $C_{max} = 20$ $U_{max} = 5$ Time = 1.50 sec

Alpha and Beta as a Function of Axial Distance
$\tau = 0.2$ sec $C_{max} = 20$ $U_{max} = 5$ Time = 1.80 sec

Figure 6-1 (cont.)

Figure 6-1 offers a great deal of information regarding the flow features of the swirling flow. First of all, the vorticity sign-switch location which is marked by the negative value of β, occurs prior to T=0.30 and continues to move downstream with time.

However, it is important to note that the value of α remains positive for quite some time, despite a negative β value, and does not attain a negative value until T=1.80, well after that of the voriticty sign-switch. This points to two possibilities. The first is that, with azimuthal vorticity always remaining positive, the axial velocity reverses its sign only after T=1.80, which is inconsistent with our previous results. The second, and more likely explanation, suggests that the reversal in axial velocity and reversal in azimuthal velocity occur simultaneously. If the two flows reverse at the same time, the value of α remains positive.

Figure 6-1 also illustrates that the values and over-all profile of α and β, for each respective radial cut, appear to match better with time. In fact, after T=0.60, the two tangents of the helical angles show striking agreement at each radii. This converging trend is due to Helmhotz's law that the vorticity does, in fact, follow the material line of the fluid; thus, even the vorticity vector and velocity vector are not aligned initially, eventually they become aligned. In addition, the temporal evolution also shows that the values of α and β reach a maximum value upstream, just aft, of the vorticity source and slowly decay thereafter. These maxima occur shortly after the inception of the vorticity sign-switch. Once established, these maxima maintain a relatively constant value and, unlike the vorticity sign-switch location, do not move downstream with time. From the point of view of controlling breakdown, this time at which these maximum values are established represent a critical stage in the formative stages of breakdown and will play an essential part in preliminary control simulations, to be discussed in the following chapter.

In their steady vortex breakdown investigation, Brown & Lopez argued that in order for the breakdown to occur, a helix angle for the velocity which exceeds that of the vorticity is a required condition at the early upstream location. Although our simulation is a transient study of breakdown, this necessary flow condition is evident in Figure 6-1. In fact, the value of α appears to maintain a larger value than β up to approximately T=0.60. With this general consideration in mind, an important question is raised; how close to a steady state flow is our transient breakdown simulation? Obviously, we would not expect the initial flow leading up to breakdown to be steady, as the flow features are changing rapidly, however, what can be said about the structure of the flow once breakdown has been achieved?

6.2   Steady-State Criterion

In order to assess the steadiness of our transient breakdown simulation, we will compare the development of the azimuthal vorticity component along a streamline obtained from our simulation with the steady predictions offered by Brown & Lopez. For the case of steady, inviscid, axisymmetric swirling flow, Brown & Lopez derived an

expression for the azimuthal component of vorticity in terms of local upstream parameters and the radius of the downstream stream surface only. This expression, for both the case of $\omega_{\theta_o} = 0$ and $\omega_{\theta_o} \neq 0$, is given below.

$$\omega_\theta = \alpha_o \omega_{z_o} \left(\frac{r_o}{r} - \frac{r}{r_o} \right) \quad \text{for } \omega_{\theta_o} = 0 \tag{6-1}$$

or,

$$\frac{\omega_\theta}{\omega_{\theta_o}} = \frac{r_o}{r} \left(\frac{\alpha_o}{\beta_o} \right) - \frac{r}{r_o} \left(\frac{\alpha_o}{\beta_o} - 1 \right) \quad \text{for } \omega_{\theta_o} \neq 0 \tag{6-2}$$

where $\alpha_o = u_\theta / u_z$ and $\beta_o = \omega_\theta / \omega_z$ are the tangents of the helical angle for the velocity and vorticity, respectfully. Since in our simulations, the azimuthal vorticity component at the vorticity source is defined by a finite and non-zero value, we will focus on the latter equation, where $\omega_{\theta_o} \neq 0$. According to this Equation (6-2), at some location downstream of a initial point, z_o, the ratio of upstream azimuthal vorticity on the streamline to its initial value at z_o is simply a function of the initial helical angles of the vorticity and velocity at z_o and the ratio of the radius at the downstream location to the initial point.

Brown & Lopez's claim that $\frac{\alpha}{\beta}$ must be greater than one for the onset of breakdown to occur is apparent in Equation (6-2). In order for azimuthal vorticity to switch its sign, a required criterion for vortex breakdown, corresponding to a diverging stream surface, $r > r_o$, is that the second term in Equation (6-2) must be made positive: $\frac{\alpha_o}{\beta_o}$ value greater than one. In other words, the initial velocity helical angle must exceed that of the vorticity in order to spawn breakdown since, from Equation (6-2) as r / r_o increases from a value of one, only for the case of $\alpha_o > \beta_o$, $\omega_\theta / \omega_{\theta_o}$ becomes negative at large r / r_o values.

6.3 Steadiness Assessment

Using Equation (6-2), an initial assessment into the steadiness of our transient vortex breakdown simulation is conducted. In essence, we are comparing the downstream values of the azimuthal vorticity, in reference to some upstream reference point, of our simulation results with that offered by the steady Equation (6-2). As mentioned, the simulation is not expected to represent a steady flow prior to the formation of the recirculation region. This fact is clearly evident in Figure 6-2, which illustrates the value $\omega_\theta / \omega_{\theta_o}$ as a function of downstream location as calculated from Equation (6-2) as well as from our transient simulation results.

Steady Verses Unsteady Investigation
$\tau = 0.005$ $\Delta t = 0.001$ sec   Time: 0.18 sec
Original Streamline Y-intersetion = 0.03
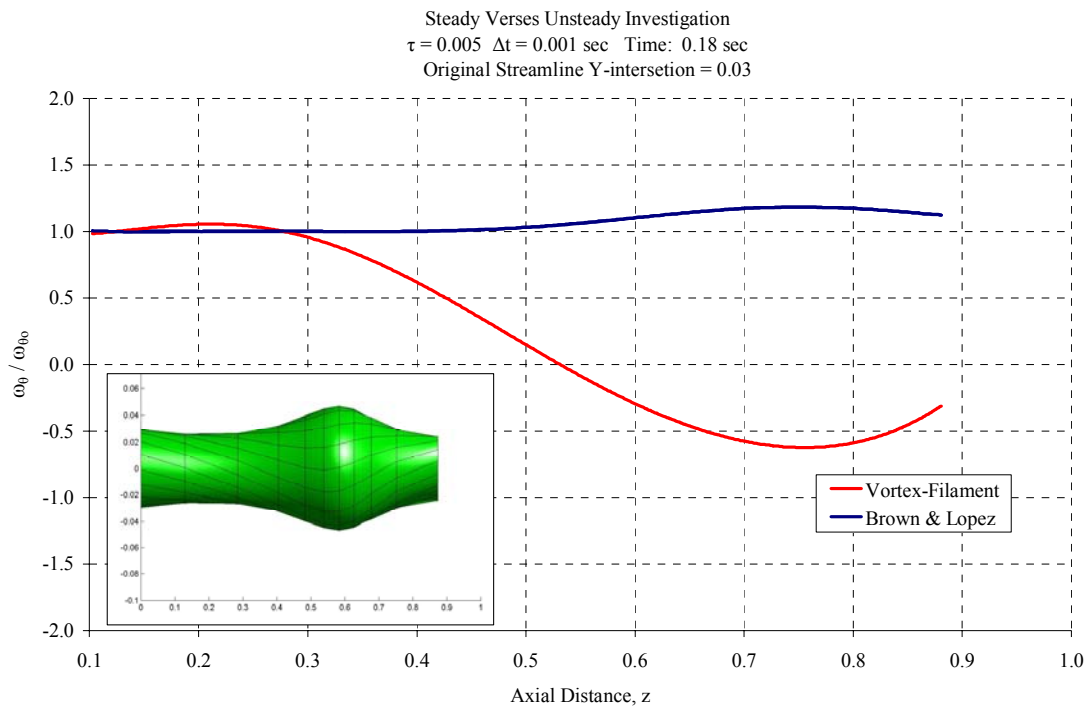
Figure 6-2: Steadiness assessment: prior to breakdown, T=0.18

As you can see, although the two methods are initially in good agreement, as they should be from the very definition of $\omega_\theta / \omega_{\theta_o}$, thereafter $\omega_\theta / \omega_{\theta_o}$ quickly diverges. Furthermore, it is crucial to note that the $\omega_\theta / \omega_{\theta_o}$ value determined by Brown & Lopez always remains positive; this suggests that the flow never experiences a vorticity-sign switch. On the other hand, the plot of $\omega_\theta / \omega_{\theta_o}$ offered by the transient simulation shows

a negative sign-switch at approximately z=0.53. This location matches well with the sign-switch location of the vortex streaklines seen in the solid rendering. Having determined that the simulation results leading up to the formation of breakdown do not represent that of steady flow, we will now focus on the flow at a later time; specifically at the time of approximate breakdown, T=1.0, and at the last time step, T=2.0. As required by Equation (6-2), an initial upstream reference point must be selected in order to calculate the downstream development of the azimuthal vorticity. An obvious reference location would be at the vorticity source, z=0. However, in order to minimize any biases or negating effect caused by the 'necking' effect immediately after the vorticity source, a reference location slightly downstream of the source will be selected, For the T=1.0 case, an axial reference location of z=0.5 is chosen. We will attempt to bridge the gap between the vorticity source and reference location by projecting the azimuthal vorticity value upstream as well as downstream of the reference location. This location is marked by the vertical dotted line in Figure 6-3 (top).

However, as can be seen in Figure 6-3 (bottom), this reference location is not the same for the T=2.0 case. Again, our simulation is a transient simulation and accordingly the recirculation bubble is continually convected downstream. Therefore, in order to keep a relative constant frame of reference we need to follow the same portion of the vortex tube with time. In the T=1.0 case, the distance from the reference location to the end of the recirculation region is approximately 4 units of length. Therefore, to maintain the same vortex tube length of 4 units, a reference location of z=2.0 is selected for the T=2.0 case. In other words, we are only concerned with how the downstream portion of the vortex selected at T=1.0 has changed at T=2.0.
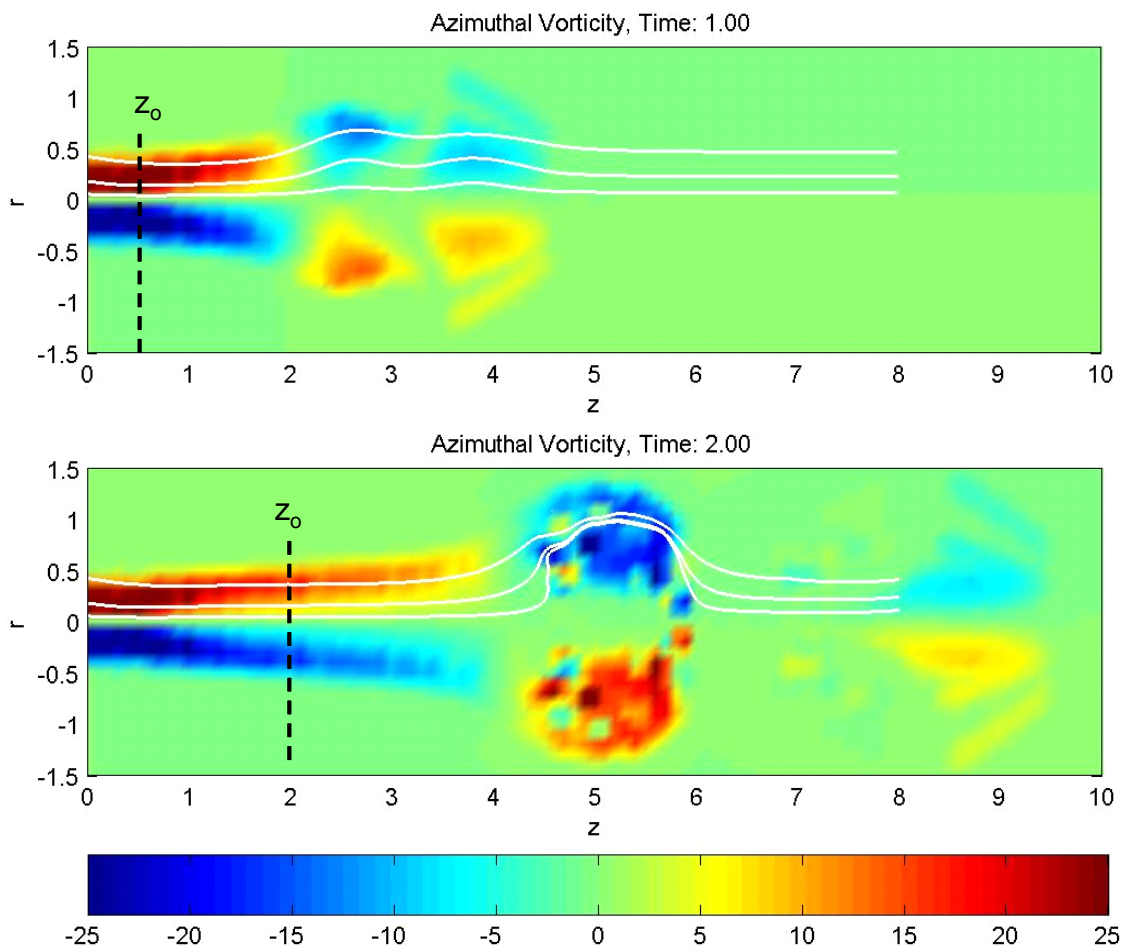
Figure 6-3: Steadiness assessment: case examples

Figure 6-3 also illustrates three projected meridional streamlines (r=0.03, r=0.18, and r=0.42). It is along these three streamlines that the value of $\omega_\theta / \omega_{\theta_o}$, in Figure 6-3, is calculated using both the results of the vortex-filament method and Equation (6-2).

Figure 6-4 shows the comparison between the simulation results and the steady state Equation (6-2) at the approximate time of the vortex experiences breakdown, T=1.0 for the baseline parameters given in Table 6-1. As can be seen in the comparison plots, the two lines initially start out in good agreement but soon then after begin to differ. Of the three respective streamlines, the r=0.03 streamline shows the best agreement while the r-0.42 streamline shows the poorest agreement.
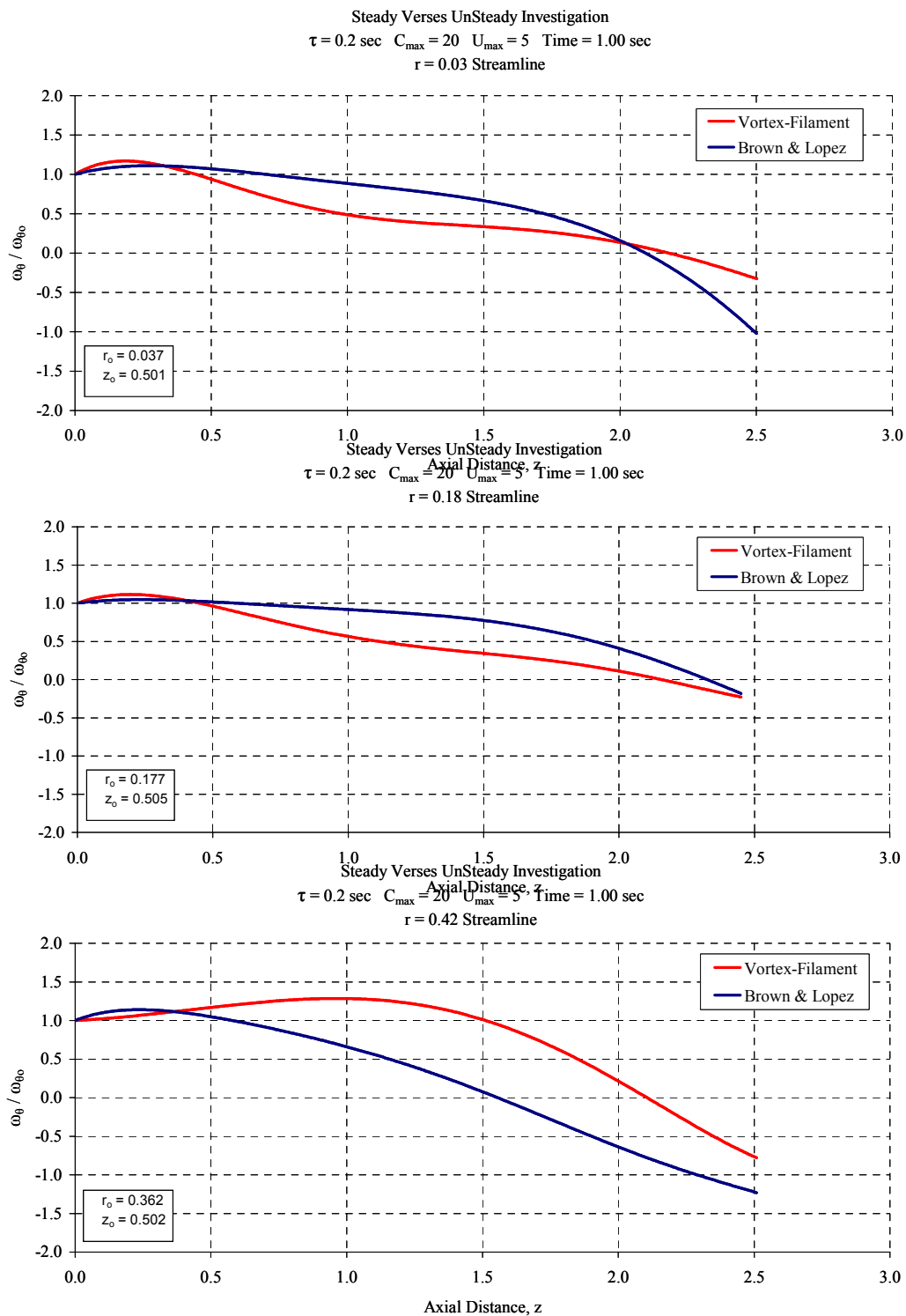
Figure 6-4: Steadiness assessment along individual streamlines, T=1.0

In general, the difference between the two becomes greater as you move radially out from the vortex core. In fact, for the r=0.42 case, Equation (6-2) predicts the axial location of the vorticity sign-switch to occur 20 percent further upstream than that of our simulation results. From this information, we can make the claim that the fluid at the very center of the vortex core of our transient simulation carries more quasi-steady flow qualities than that at the outer edge of the core. Additionally, it is also evident from Figure 6-4 that the agreement in the predicted location of the vorticity sign-switch also worsens as you move out radially from the vortex core. Moreover, the gross trends for the results of both methods appear to be relatively similar along all three streamlines. In fact, both methods illustrate a vorticity sign-switch along each respective streamline, which we know, from our previous studies, to occur in fat at this time. The location of the vorticity sign-switch, predicted by the simulation results, remains relatively unchanged in axial location with increasing radii. This trend ties into our earlier argument in that the axial flow stagnation point first appears at the inner most core radius and prorogates almost instantly radially outward.

Continuing on with our steadiness assessment, we perform at T=2.0 a similar comparison between the development of azimuthal vorticity along the streamline with that proposed by Brown & Lopez's steady formula, which is illustrated in Figure 6-5. Immediately clear is the fact that the three plots appear to show better agreement than those offered for T=1.0 in Figure 6-4. Like the T=1.0 case, the r=0.03 case at T=1.0, shows remarkable agreement between the two methods up to the sign-switch location which, in reference to Figure 6-4, coincides with the axial velocity stagnation point. However, immediately after this point, the two methods begin to differ with the Brown & Lopez method showing a faster negative drop in the value of $\omega_\theta / \omega_{\theta_o}$. Similarly, the profiles of the intermediate and outer streamline at T=2.0 maintain a better agreement for a longer portion of the vortex tube. It is also important to note that at r=0.42, the Brown & Lopez formula does not show the value of $\omega_\theta / \omega_{\theta_o}$ becoming negative; hence according to their result the vorticity along this material streamline does not experience a sign-switch, in contrast to the results of the simulation. In other words, the steady formula suggests that the flow at this radius continues to swirls around the core and

recirculation bubble in its initial direction, never experiencing a switch in swirling direction.
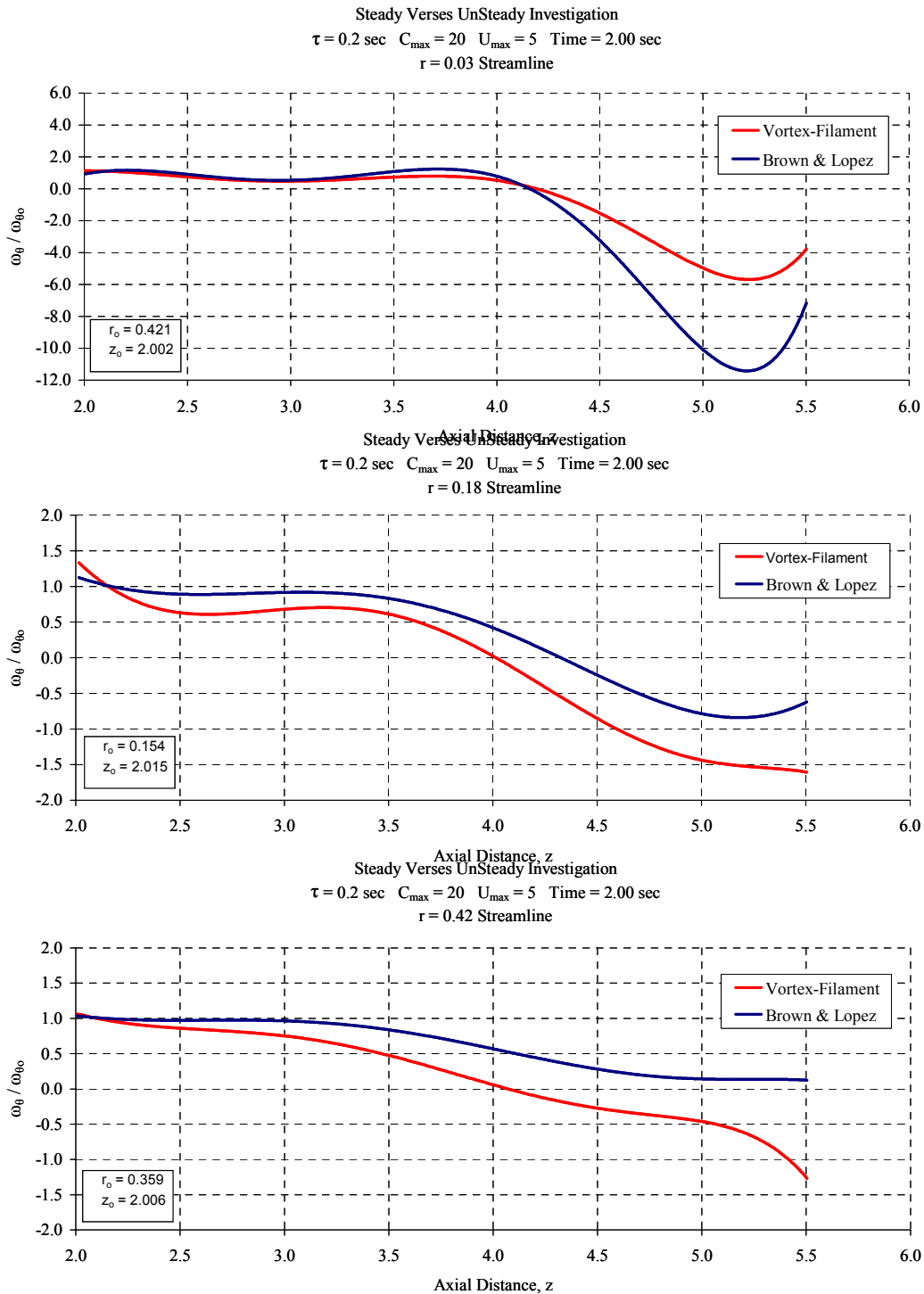
Figure 6-5: Steadiness assessment along individual streamlines, T=2.0

In summary, the steadiness assessment of our transient vortex simulation has illustrated a trend opposite to that of the radius of curvature method offered in the previous chapter. The radius of curvature method showed better agreement with the simulation vorticity results with increases radial distance from the core centerline and with decreasing time. On the contrary, the vorticity relationship represented by the Brown & Lopez's steady formula was found to be in better agreement with our simulation results with decreasing radial distance and increasing time. As a result, there is a trade-off between the two methods; as one method improves with a varying degree, the other worsens. From a control prospective, although the Brown & Lopez method does give support to the flow features of swirling flow, it does not offer much accurate insight into the flow properties during the formative stages of vortex breakdown.

7   Preliminary Control

Having gathered considerable great insight into the flow mechanisms of swirling flow and isolated key features of inviscid vortex breakdown, this section investigates the possibility to control and/or delay vortex breakdown by manipulating the azimuthal vorticity gradient.   Using the results presented earlier in this paper along with past contributions to the explanation of vortex breakdown, this section offers two specific control simulation scenarios.   The first involves adding opposite circulation to the flow whereas the second scenario entails creating a positive vorticity gradient. Both control cases will be modeled using the vortex-filament method and the results will be presented and discussed.

7.1   Mirrored Profile Control Simulation

The first attempt at actively controlling vortex breakdown entails the addition of opposite circulation into the vortex core. Although this technique has been proven to be quite difficult to perform experimentally, the vortex-filament simulation can perform this rather easily and consistently.

7.1.1   Simulation profile

But when is the appropriate time to add opposite circulation to be added? Obviously, we want to give the simulation enough time to induce the formative stages of breakdown such that we can see the effects of adding opposite circulation. One distinguishing feature that was discovered in the previous chapter was the unique maximum value of β. This maximum value occurred after the vorticity sign-switch but prior to the complete development of the recirculation region. Therefore, we will use this feature as the 'control switch' for our simulation. In other words, when the value of β (along the r=0.18 plane) reaches a maximum, the simulation will immediately begin to add opposite circulation, equal to C_{final} in magnitude, to the vortex. We will refer to this control simulation as the 'mirrored' control simulation since we are mirroring the circulation profile.

Ideally, you would want to add the opposite circulation in order to affect directly the region of flow where the formative features of breakdown are occurring. One method to achieve this would be to allow the region of opposite circulation to be convected downstream at a faster rate than the rest of the vortex tube, allowing it to catch-up with the formative breakdown region. The present vortex-filament method code, however, does not incorporate the ability to do such. In our simulation every material point along the vortex is convected downstream at an equal velocity. Similarly, in our present set-up circulation is prescribed prior to the start of the simulation and therefore, we can not arbitrarily change the circulation of an individual portion of the vortex downstream of the vorticity source. As a result, the region of opposite circulation addition will initially travel at the same speed as the region of initial breakdown. This should, however, not hamper the effects of the opposite circulation so long as it is added close to the formative breakdown region.

Figure 7-1 shows the velocity and circulation profile for the mirrored control case. It is also important to note that besides the switch in circulation, all other parameters are set to be the same as the baseline case value, previously shown in Table 3-1.
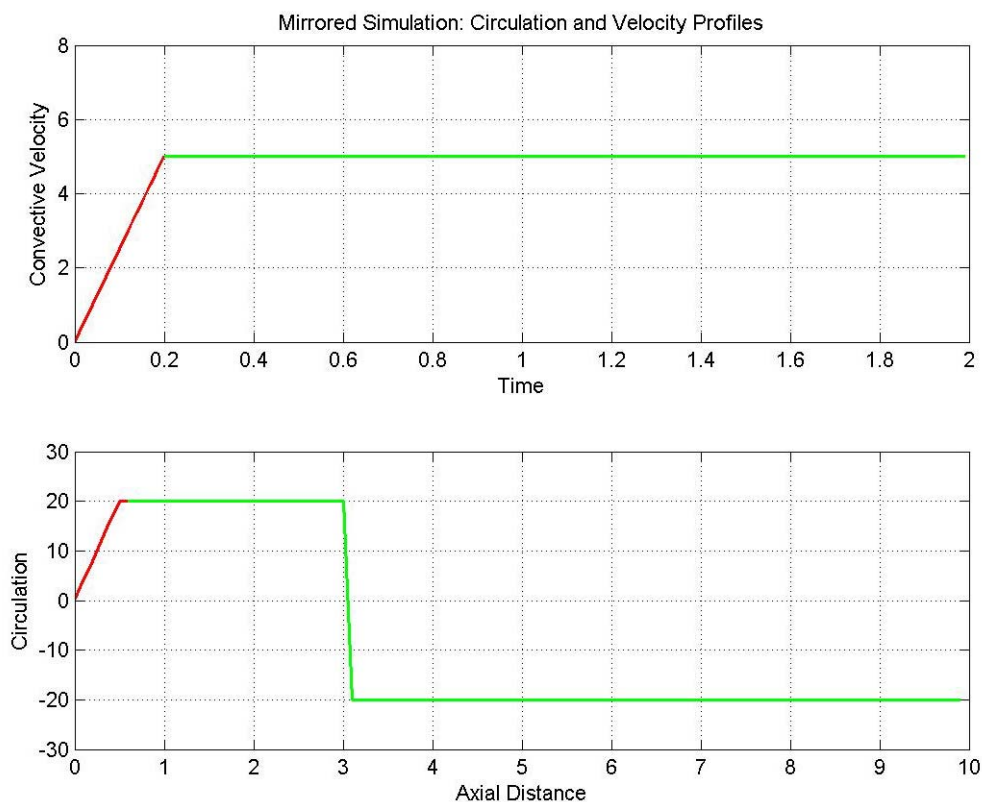
Figure 7-1: Mirrored control simulation profile

7.1.2 Simulation results

The simulation results of the mirrored control case (r=0.08) are shown below in Figure 7-2. As you can see, there is a new blue region associated with the vortex tube. In an effort to investigate the effects of radial expansion and contraction at the downstream edge of the red region, a vortex tube extension with no circulation was placed in the domain prior to T=0. This vortex tube, represented by the blue region below, is analogous to the flow within a tube pre-existing prior to the introduction of swirling flow or circulation, similar to the experimental transient study performed by Hamada (*ref.* 14)
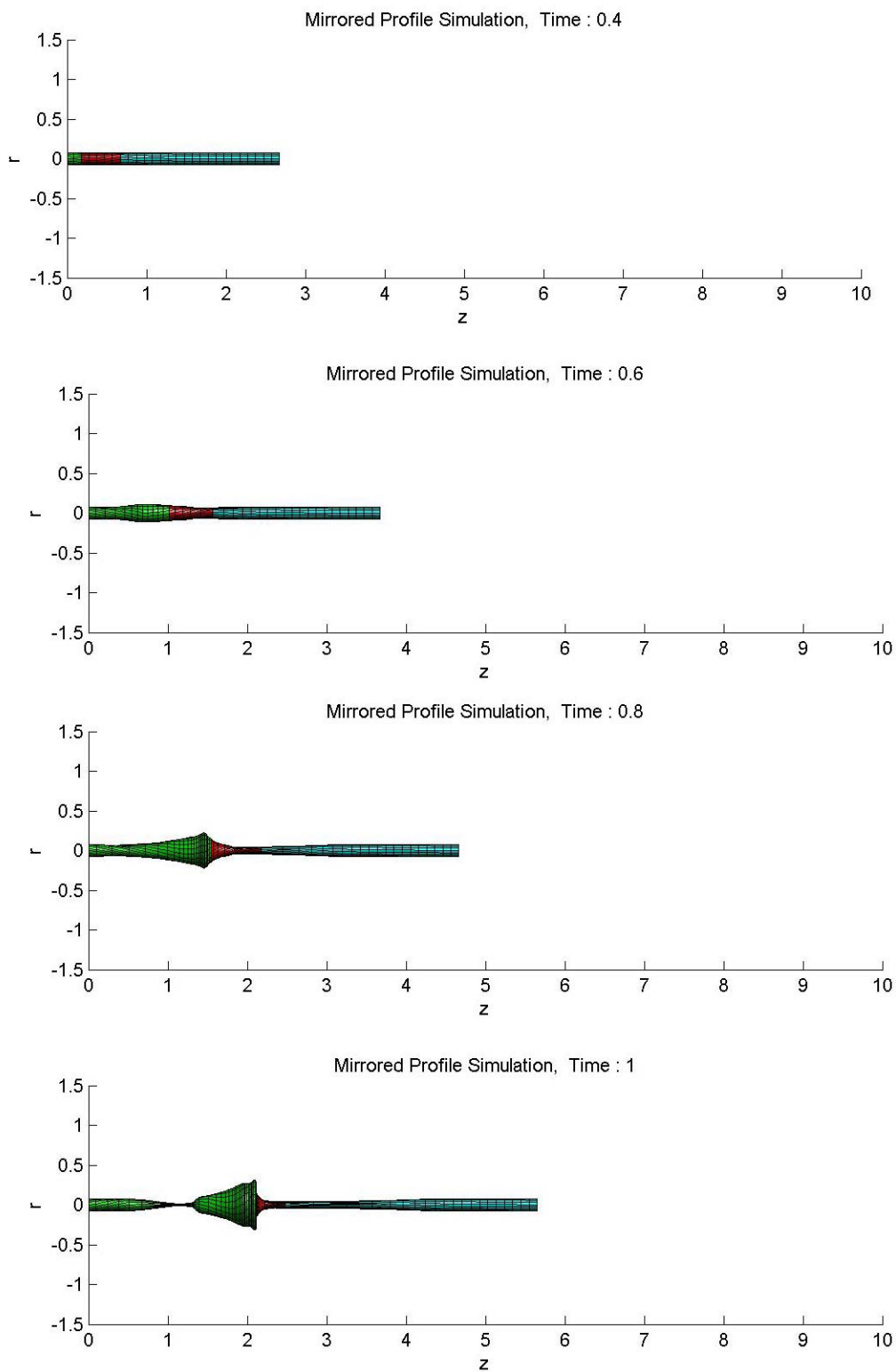
Figure 7-2: Mirrored control simulation results, r=0.08
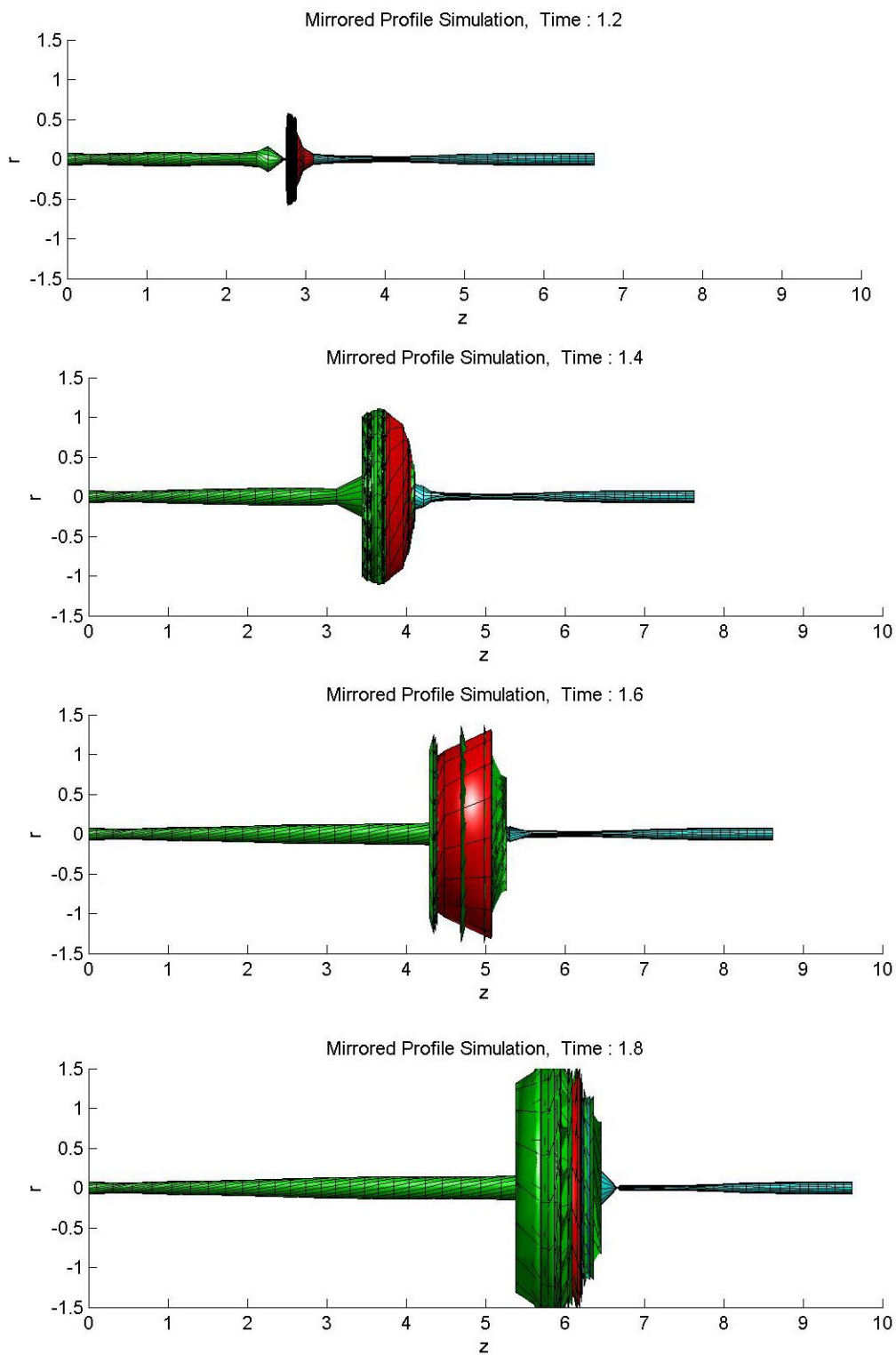
Figure 7-2 (cont.)

7.1.3   Discussion

The results in Figure 7-2 are of arresting interest. The first thing to note is that the vortex tube undergoes the same exact formative breakdown flow features that were discussed in the preceding chapters. In fact, the structure of the vortex tube is exact to that offered by the baseline simulation up to approximately T=0.90, at which opposite circulation begins to be added. The opposing circulation is evident by the reversal in swirling direction of the vortex streaklines, highlighted below for T=1.0.
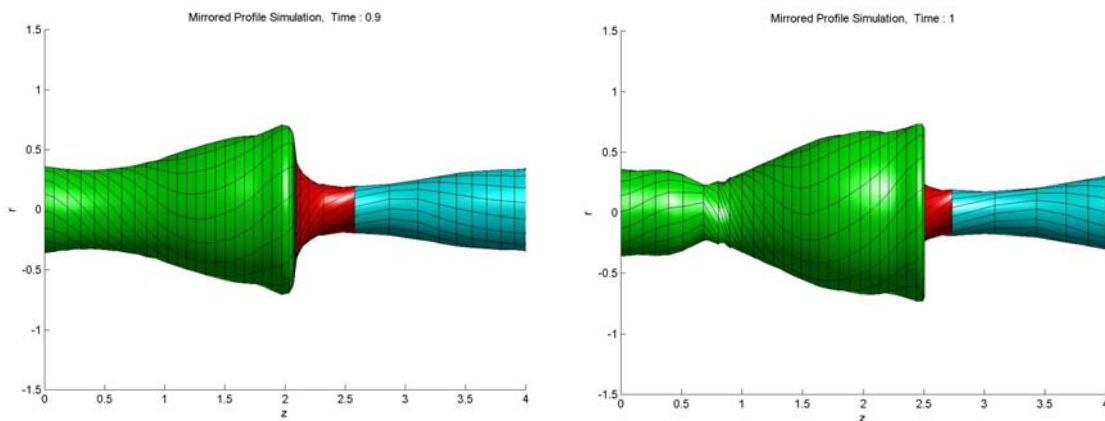
Figure 7-3: Opposite circulation and vortex streakline reversal

A sharp pinch is formed at the location of the opposite circulation addition However, this pinch can be explained from a vorticity gradient perspective. The circulation immediately downstream of the pinch is positive and the circulation immediately upstream is negative. As a result of this opposite direction of swirl, circumferential tilting of vortex filaments become reversed at the kink. This generates negative azimuthal vorticity upstream of the kink, followed by the usual positive azimuthal vorticity just downstream. Consequently, this sudden jump in circulation causes a relatively large and positive local azimuthal vorticity gradient at the pinch. From our previous discussions, we know that a positive azimuthal vorticity gradient, $\frac{\partial \omega_\theta}{\partial z}$, causes radial contraction. However, in this case, the gradient is so large that the contraction is almost instantaneous, forming what is illustrated as a sharp kink at T=1.0 in Figure 7-2.

Subsequently, another notable flow behavior becomes apparent. At approximately T=1.2, the downstream bowl-like structure, which can be thought of as the upstream edge of the recirculation bubble, begins to lose its conical shape and flattens vertically. Quickly thereafter, the once bowl-structure flips and begins to form upstream. Furthermore, the addition of opposite circulation continues in time, the now upstream-facing structure begins to deepen, as seen at T=1.40. However, if we take a snapshot of the flow just prior to the flip, we see that the flow exhibits a very thin radially-shaped structure, as seen at T=1.30 in Figure 7-4.
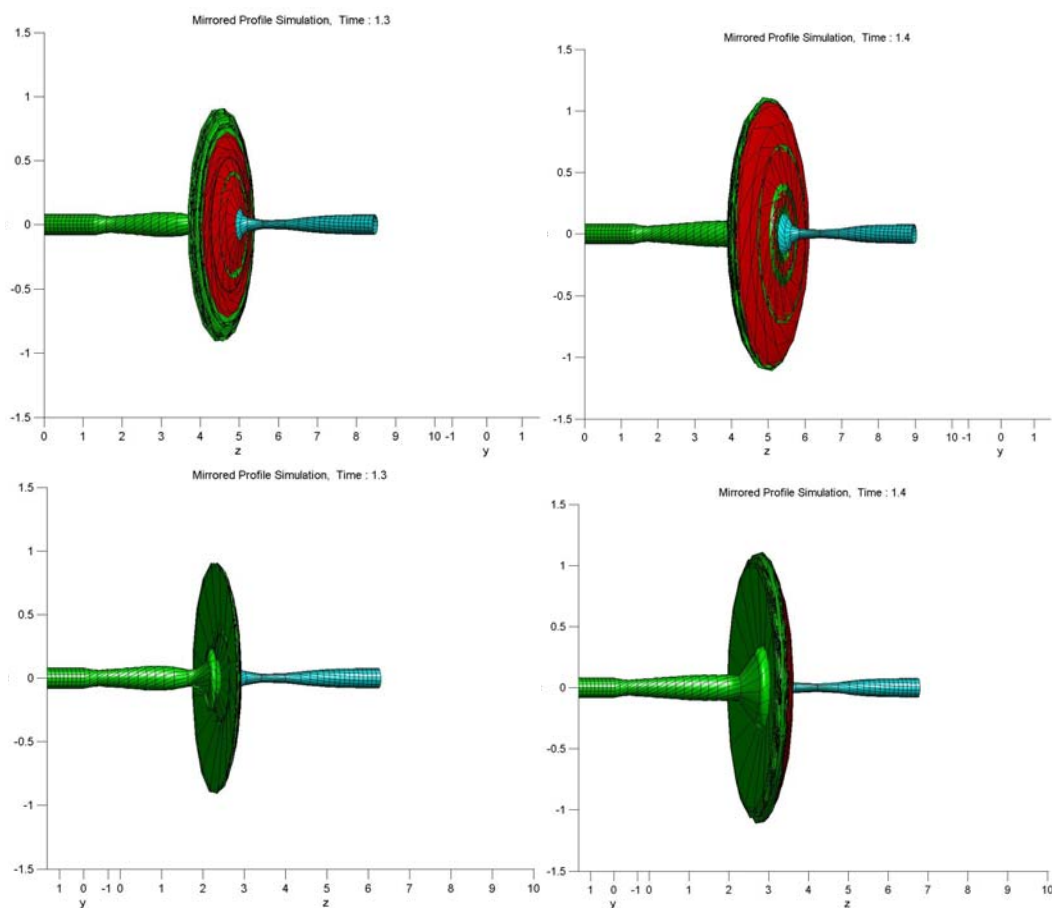
Figure 7-4: Mirrored control simulation: vorticity destruction

This disk-like structure is a result of the vortex-filament method's inability to account for viscous effects. As mentioned earlier, the present simulation is inviscid, and as such, does not allow for the cancellation of opposing vorticity which, in real flow, occurs within the recirculation region. As a result, the induction process involves the two

opposing vorticity elements, inducing a velocity in the radial direction. Therefore, given an equal and opposite amount of vorticity within the recirculation bubble, the simulation would induce radial displacement. In the mirrored circulation case, the introduction of opposite circulation causes a mass inflow into the recirculation bubble, which from continuity and a lack of viscosity will lead to larger radial displacement. This scenario is illustrated below in Figure 7-5.
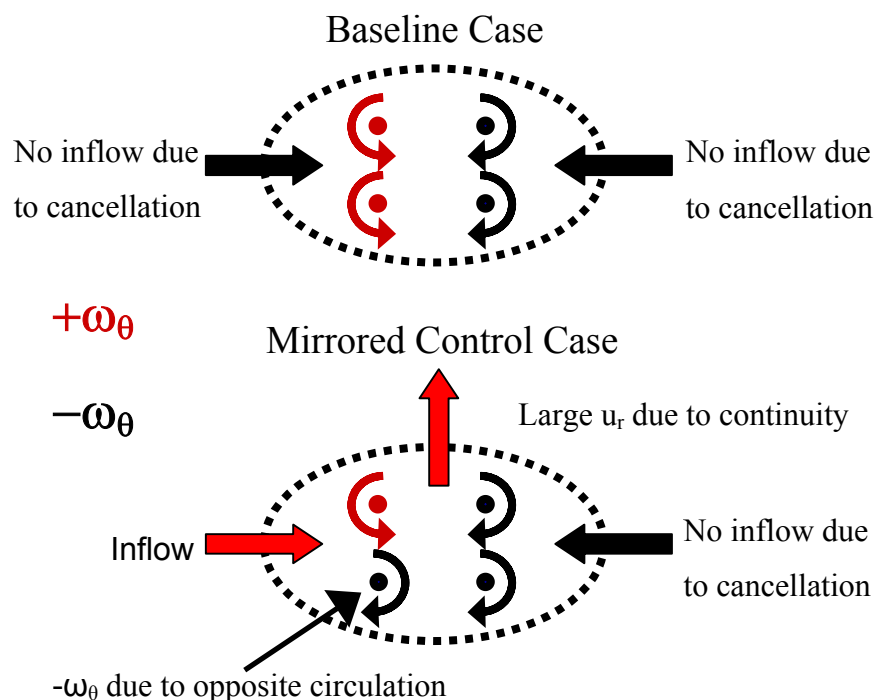
Figure 7-5: Vorticity Cancellation

The flip and upstream facing bubble is therefore the result of the continuing induction process on the should-be-canceled region. These findings support the claim that had the flow been given the ability to cancel out opposite vorticity, the radial expanding region would have been suppressed and soon abolished, eliminating any future breakdown in the vortex.

7.2   *Positive Vorticity Gradient Control Simulation*

The second control scenario involves applying a positive vorticity gradient to the flow during the formative stages of vortex breakdown. The aim is that such a positive

vorticity gradient will cause radial contraction along the vortex tube, suppressing the radially expanding region and ultimately preventing breakdown.

7.2.1   Simulation profile

Similar to the mirrored control case, the question of when to apply the positive vorticity gradient again comes into play. The placement of such a gradient is crucial. If the vorticity gradient is applied too soon, then the self-induction process will not trigger the formative features of breakdown, whereas, if the vorticity gradient is applied too late (too far upstream of the predicted breakdown location) its effect on the region of radial expansion and reversed axial velocity will not be strong enough to suppress the inevitable breakdown of the flow. If the vortex-filament method could allow us, we would choose to convect the positive gradient faster downstream than that of the downstream portion of the vortex tube, the hopes being that the positive vorticity gradient would add to the already existing negative gradient and cancel. This destructive cancellation would prevent radial expansion which, if left alone, will continue to intensify due to the feedback cycle of the self-induction process, further triggering the inviscid breakdown progression.

In our case, since we can not force the positive vorticity gradient faster downstream nor impose a negative gradient directly to a downstream location, we are hoping that the influence of the upstream positive gradient alone will weaken the downstream negative vorticity gradient. If this is in fact the case, we may not be able to completely eliminate breakdown, but could suppress its development. In reality, suppressing breakdown may be as effective as completely eliminating it; if you can suppress it long enough the breakdown location is forced outside of the area of interest. This would be analogous to delaying breakdown over a delta wing long enough such that it breaks down well aft of the trailing edge of the wing.

Since we expect the effect of the positive gradient to be less than that of the opposite circulation, the positive gradient needs to be added closer to the moment of initial radial expansion. Therefore, we will set a temporal 'control switch' at T=0.5.

This time is approximately half way between the time of initial radial expansion and the time of maximum β value.

Figure 7-6 shows the velocity and circulation profile for this positive vorticity gradient control case.
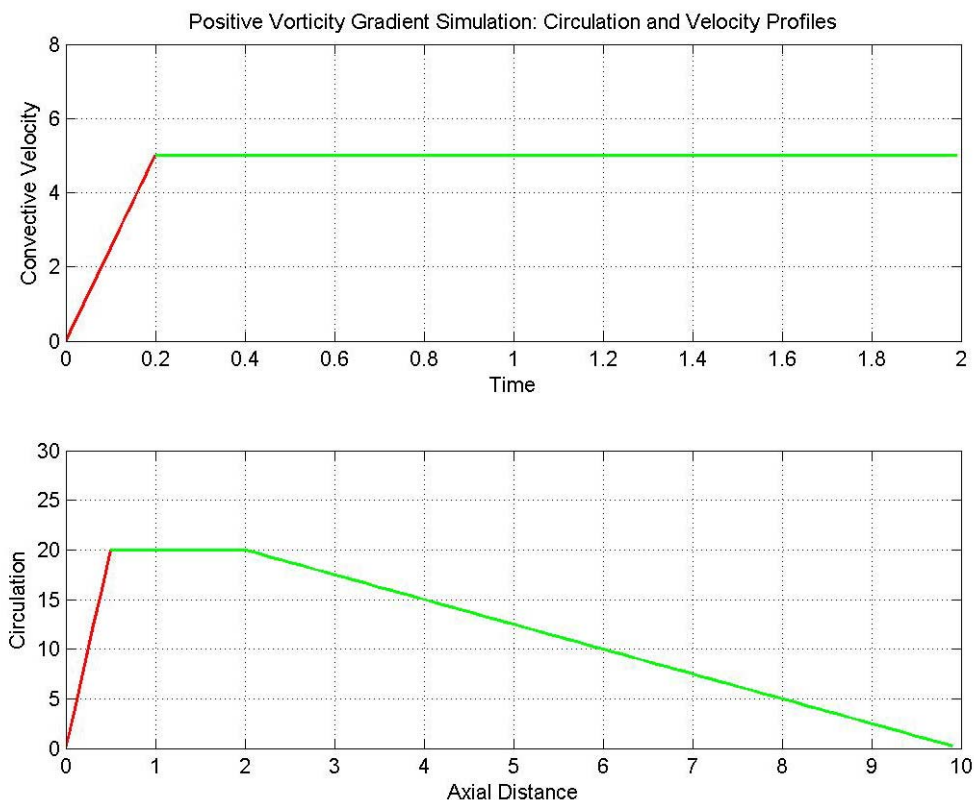
Figure 7-6: Positive vorticity gradient control simulation profile

7.2.2   Simulation results

The simulation results of the positive vorticity gradient control case are shown in the following figures.   Figure 7-7 illustrates the solid rending results for r=0.08, whereas Figure 7-8 shows the solid rending of the vortex tube at r=0.03.   As in the first control simulation, the addition of a blue region is utilized to model the existence of fluid within the domain, prior to introducing any type of swirling motion.
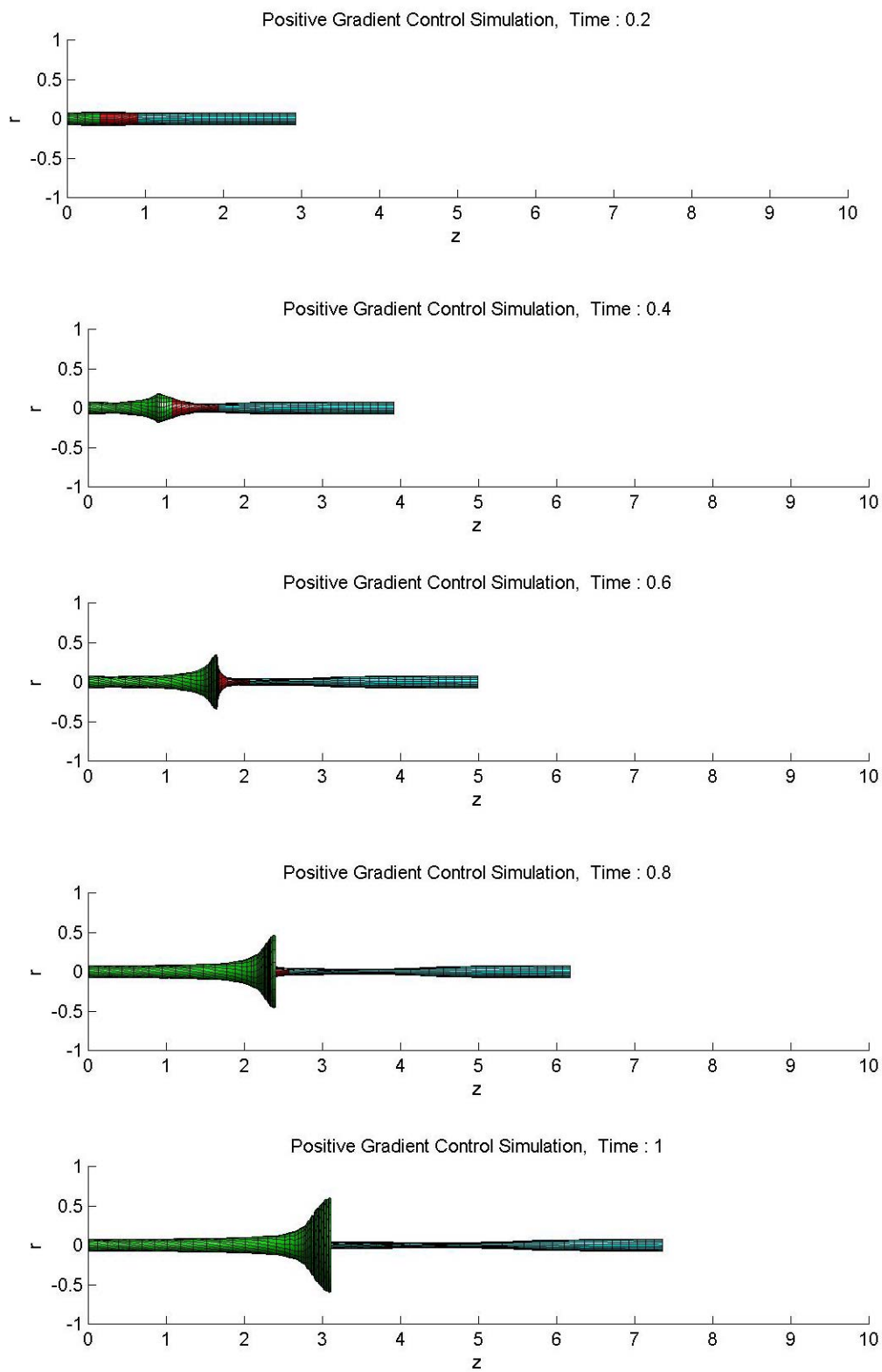
Figure 7-7: Positive gradient control simulation results, r=0.08
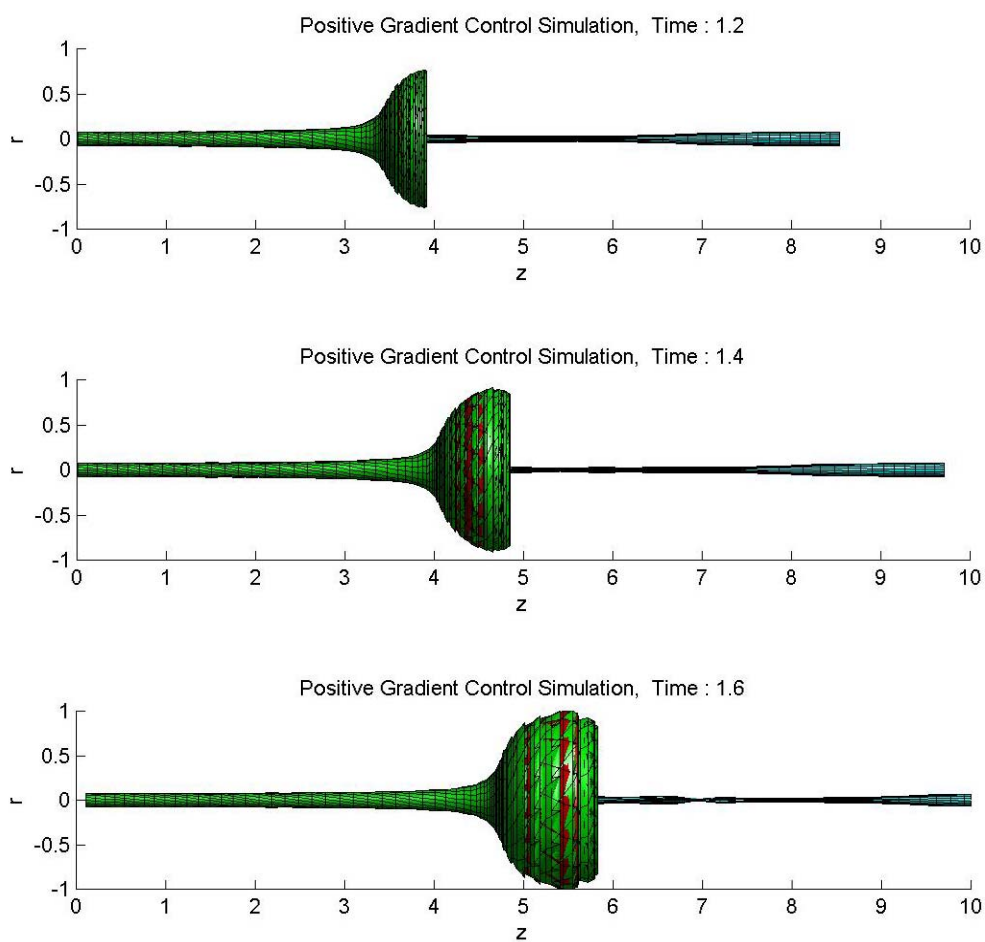
Figure 7-7 (cont.)
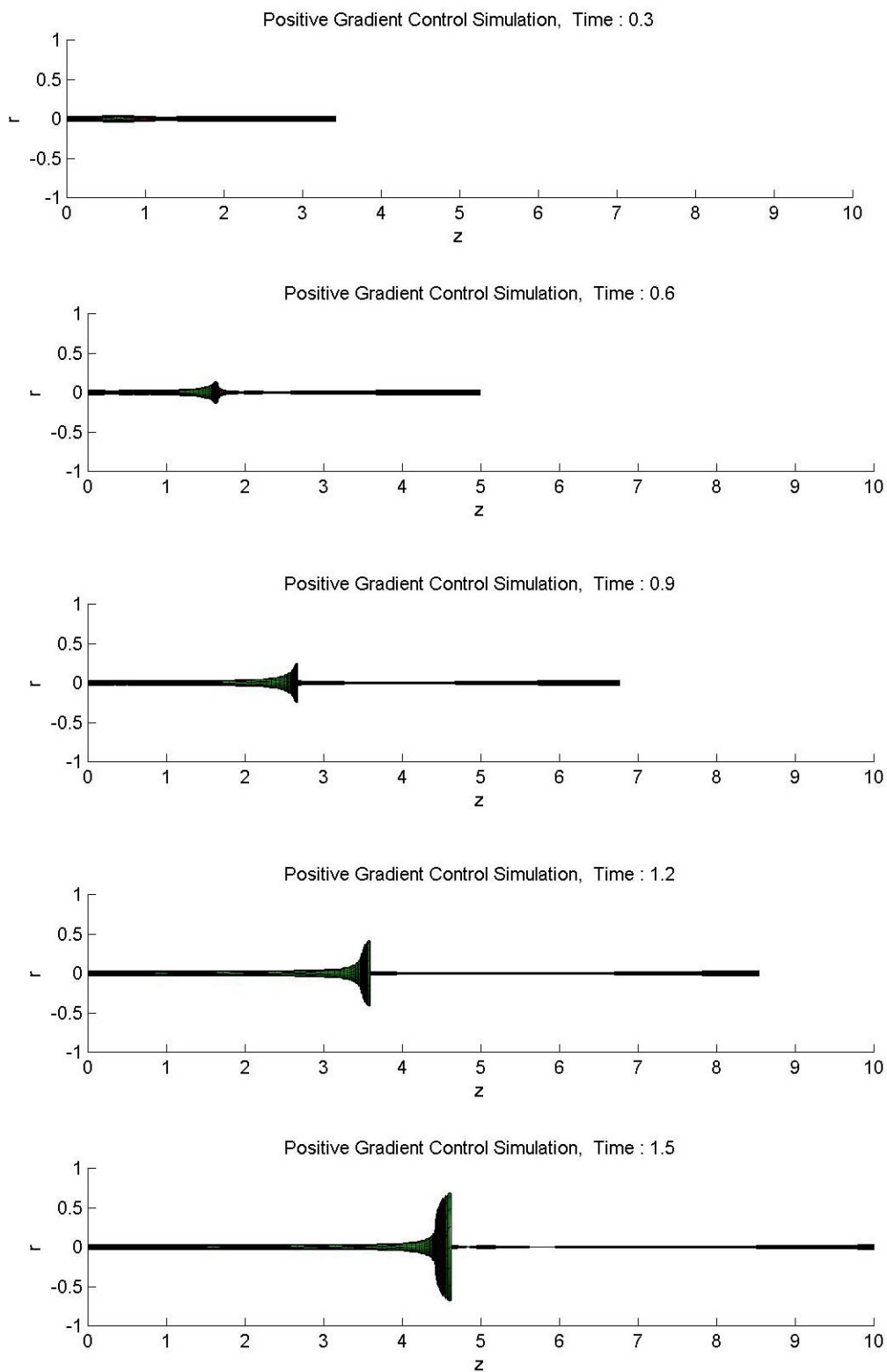
Figure 7-8: Positive gradient control simulation results, r=0.03

7.2.3 Discussion

The results in Figure 7-7 and Figure 7-8 do not illustrate the dramatic deviation in flow development as seen in the previous control scenario. At first glance the flow appears to follow the exact formative breakdown route as our previous baseline scenario. However, through close inspection, we soon gain evidence that the flow is different than the baseline case. When directly compared with the baseline case, there appears to be a slight delay in the formative features of breakdown after the initial introduction of the positive vorticity gradient, commencing at T=0.5. After this time, the development of the transient vortex is subject to the effects of the upstream positive gradient. The initial influence of the positive gradient on the vortex flow structure can be seen in Figure 7-9.
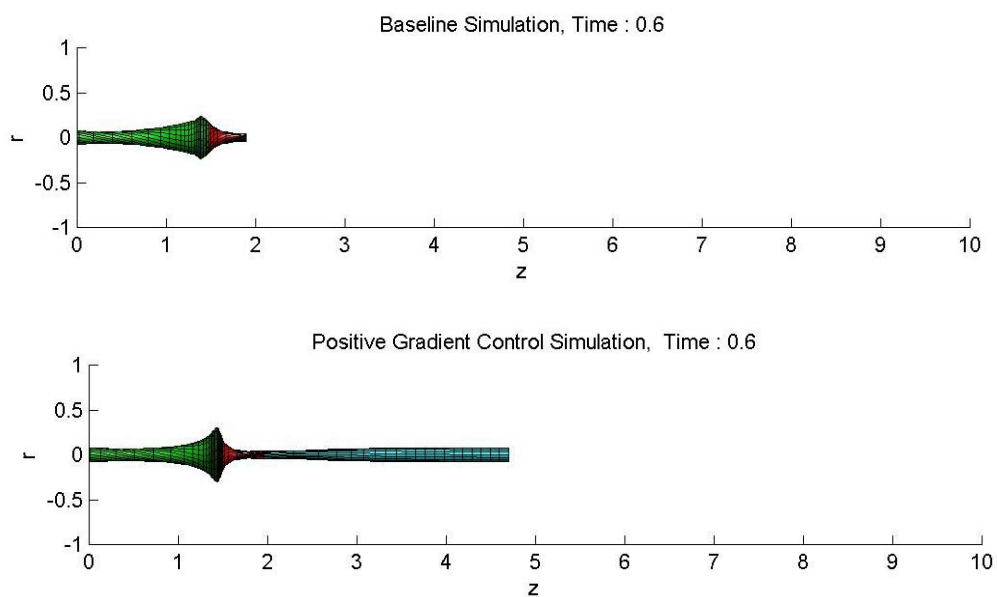
Figure 7-9: Positive gradient control simulation comparison, T=0.6

Figure 7-9 offers a direct comparison of the solid rendering of the vortex streaklines of both the baseline and control simulation at T=0.6. As you can see, though slightly different in shape, the general profiles of the two vortex tubes agree well with each other. This strong similarity highlights the fact that the effect of the positive gradient has been quite minimal up to this point in time. This, however, is to be expected since the positive gradient has only been introduced for approximately 0.1 units of time.

As the flow continues to transient downstream, the vortex tube is subject to more of the positive vorticity gradient, traveling upstream of the radial expanding region. Therefore, we would expect to see a stronger influence of the gradient on the flow as time progresses. Our assertions are proved to be correct in Figure 7-10. In this figure, a comparison between the baseline and control simulation is again offered, but this instance at a later time of T=1.4. The structure of the two expanding regions are, again, very similar; illustrating the initial formation of the recirculation bubble. However, in this case, there is a significant difference in the axial location of the upstream edge of the breakdown bubble. The difference can be traced back in time to the initial introduction of the positive gradient and increases with time.
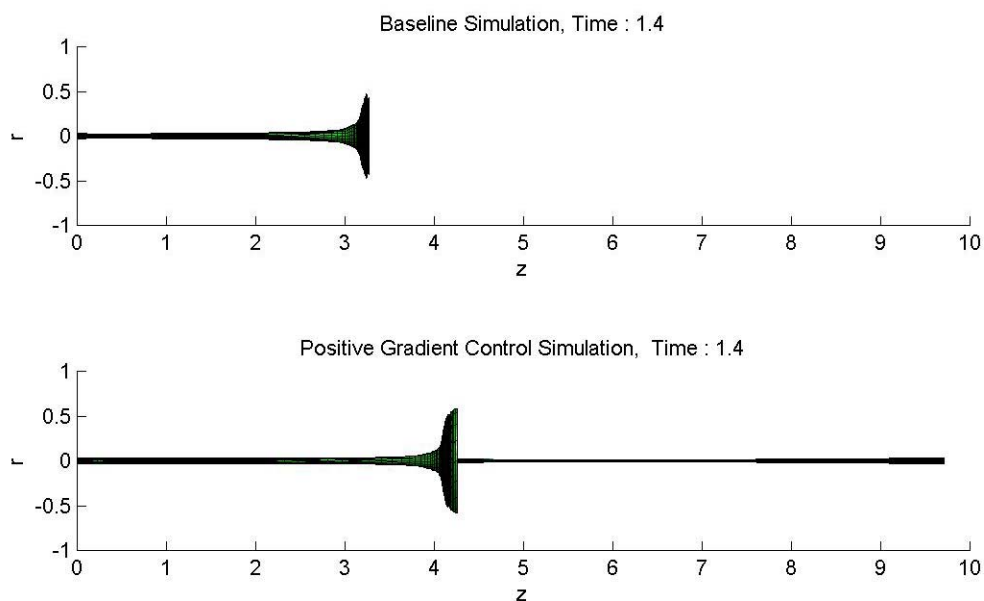
Figure 7-10: Positive gradient control simulation comparison, T=1.4

This behavior leads to the claim that the addition of the positive vorticity gradient causes a delay in the breakdown of the vortex. One question that needs to be further investigated is that whether the positive gradient continually suppresses the breakdown region as it transients downstream or if, in fact, the growth of the radial expansion region is only initially stunted by this gradient but not its subsequent growth. Both of these cases could lead to the flow development exhibited in Figure 7-9. Regardless of them,

the introduction of the positive vorticity gradient does appear to slow the rate of radial growth, thus reducing the effects of the reversed axial velocity. Both aid in moving the stagnation location further downstream, relative to the flow.

Additionally, one can assume that the positive gradient's ability to weaken the radial expansion would only increase if we were able to either add it directly to the region of radial expansion or force it downstream at a faster rate than that of the flow. Nonetheless, the introduction of a positive vorticity gradient appears to delay the breakdown process, which in many applications can be viewed just as good as preventing it

7.3   *Experimental Control Considerations*

Both control scenarios offer valuable knowledge into the control features of the swirling flow. However, in order to validate the aforementioned findings and claims, the two scenarios need to be confirmed experimentally. Doing such eliminates many effects which are caused by the limiting assumptions of the vortex-filament method. Furthermore, substantiation of the scenarios experimentally allows for effects of viscosity to come into play which, although not required for breakdown to occur, is still an important feature.

From an experimental control perspective it may, however, be difficult to apply either opposite circulation or a positive vorticity gradient to the downstream portion of the vortex. In fact, past experimental studies, such as performed by Wimer, have given evidence that after a certain distance the vortex core no longer entrains any fluid from outside of the core. In the specific case of a delta wing, Wimer found this crucial distance to be approximately 10 percent of the chord. At this approximate distance, the vortex core is completely formed and thereafter remains constant along the axial length of the vortex until reaching the location of breakdown. This fact serves to say that, if left undisturbed, the elements needed for breakdown are established well upstream of the breakdown location. In such case, death of the vortex is not only determined, but also must set into motion, near its birth.

With this in mind, the difficultly in controlling the breakdown of the vortex becomes quite obvious. In order to offer any possibility of success, one must be able to add either opposite circulation and/or impose a vorticity gradient directly into the core during the early development of the vortex in order to control its breakdown. This task, in itself, is extremely difficult since the core size, as well as the length of the vortex, in most experiments is extremely small.

8   Current On-going Studies

Even in light of the computational and theoretical evidence gained by this report, a complete understanding into the fundamental nature of vortex breakdown is still yet to be achieved. In a continuing effort to pursue and reach an all-encompassing agreement into the breakdown of vortex flow and the interactions between its key flow features, additional investigations are currently on going. This section offers two such on-going investigations. The aim and background for each investigation is briefly discussed, in to addition to highlighting their essential role in future control simulations.

8.1   Necking Effect

Although the modified vortex-filament method has been proven to successfully model inviscid development of vortex breakdown, there are still many artifacts of the current self-induction process which require further refinement and improvement. One such area for improvement involves the necking effect which occurs as the vortex filaments emerge from the vorticity source into the flow domain. This immediate effect causes the vortex tube to initially contract, giving the appearance of the quick narrowing behavior of the vortex core. Its effect can also be seen in the comparison plots of Equation (5-7), by the initial positive gradient immediately downstream of $z=0$. The necking effect is a trivial effect on both the inviscid development of the vortex core and its effective breakdown process. Nonetheless, this effect represents an inaccurate flow feature, and does not manifest itself in experimental investigations. Therefore, further modifications need to be applied to the current vortex-filament method in order to eliminate this erroneous flow feature.

Before improvements can be made to alleviate the necking at the vorticity source, the cause for this must first be determined. In the current vortex-filament method, the geometry of the vortex tube is prescribed prior to the self-induction being set off. The axial cross-section of vortex is composed of nine concentric circles. Each axial slice of these nine concentric circles is the same, and axially displaced a defined distance, dz, from the upstream. As a result of this geometry, the vortex filaments connecting the nodes between the radial slices are not only straight but aligned parallel to the z-axis.

Therefore as the filaments emanate from the vorticity source, they enter the flow domain in this straight and horizontal configuration. Once in the flow domain, they are subjected to the self-induction process and begin to tilt circumferentially. They continue to tilt more and more until reaching a constant tilt angle, at which they will stay til they are incorporated into the vorticity sign-switch region. It is important to note that the tilt angle, although it remains temporally constant in the present simulation, is different for each respective radial shell. It so happens that the necking effect occurs exclusively in the region in which the filaments are transitioning from horizontal to the temporally constant angle.

If we analyze the behavior of the vorticity vector in this region, it becomes evident that the necking is related to this change in vorticity vector. As the vortex filaments begin to tilt from horizontal, the azimuthal component of their vorticity vector also begins to increase relative to the upstream position, creating a positive azimuthal vorticity gradient. This positive vorticity gradient, as explained in the earlier chapters, causes local radial contraction. This radial contraction manifests itself in the form of the perceived necking behavior.

Therefore, in order to remove the necking effect, we must eliminate the tilt transition of the vortex filaments. The most obvious way this can be accomplished is by forcing the filaments within the necking region to stay at the required tilt angle. This method, however, requires dramatic changes in the self-induction algorithm which has been proven to be quite challenging. The alternative, and more appropriate method, entails prescribing the vortex tube geometry, such that all vortex filaments along the length of the vortex tube are already tilted at the needed angle prior to the start of the self-induction. This exact modification is currently being implemented into the vortex-filament method.

A good approximation of the required filament tilt angle is to specify the helical angles, which were discussed earlier for our baseline simulation, earlier in this paper. Since our simulation assumes axi-symmetric flow, each node within an axial slice of the vortex tube is simply rotated by an angle equal to that of the corresponding helical angle.

Due to the upstream proximity of the affected region, this modification is crucial to future control attempts and simulations.

      Figure 8-1 illustrates an image of the current modified vortex tube. The blue rings trace the axial slices of the r=0.42 shell while the red spiraling lines represent the vortex filaments. As mentioned, the vortex filaments no longer run parallel to the centerline of the vortex core, but rather swirl around the vortex at the given helical angle.
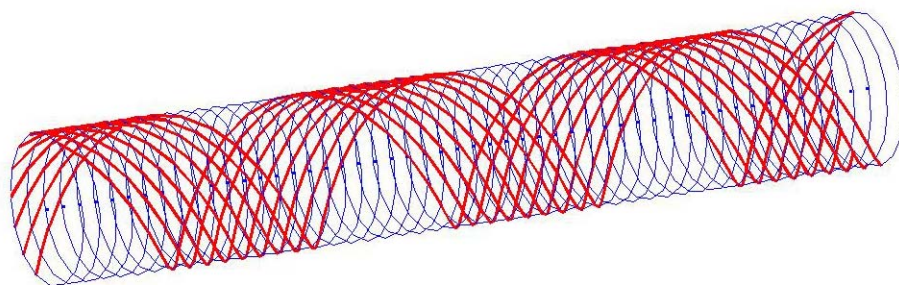
Figure 8-1: Modified vortex tube, r = 0.42

The upper illustration in Figure 8-2 displays the same vortex tube, as above, but this time viewed from the side. The lower illustration in the Figure 8-2, shows two of the concentric radial shells simultaneously; the black filaments refer to the r=0.24 shell and the red, again, to r=0.42. As can be seen, the two respective vortex filaments are not subjected to the same helical angle. In fact, the inner black filaments spiral tighter than those of the outer filaments.
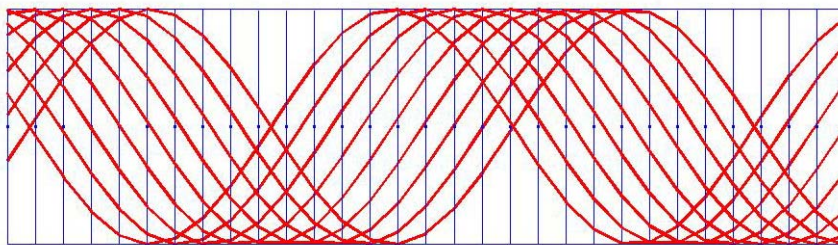
Figure 8-2: Modified vortex tube, side view
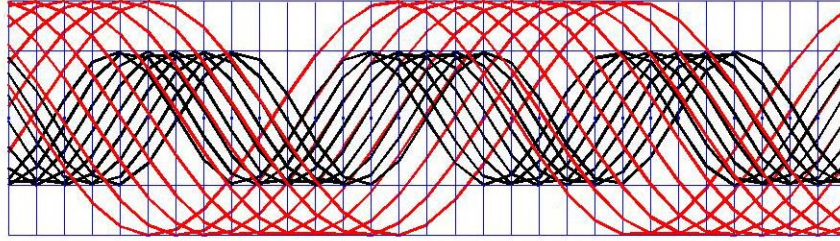
Figure 8-2 (cont.)

8.2   *Additional Analytical Study*

Similar to the local dynamic relationship that was derived in Chapter 5 linking the azimuthal vorticity gradient to the local change in radius of curvature along a projected streamline, an expression connecting directly the radial velocity and the axial gradient of azimuthal vorticity can also be obtained.   To obtain this direct relationship, the equation of continuity for axi-symmetric flow, $\dfrac{1}{r}\dfrac{\partial(ru_r)}{\partial r}+\dfrac{\partial u_z}{\partial z}=0$, is substituted directly into the azimuthal vorticity equation, $\omega_\theta=\dfrac{\partial u_r}{\partial z}-\dfrac{\partial u_z}{\partial r}$, resulting in

$$\frac{\partial^2 u_r}{\partial r^2}+\frac{1}{r}\frac{\partial u_r}{\partial r}-\frac{u_r}{r^2}+\frac{\partial^2 u_r}{\partial z^2}=\frac{\partial\omega_\theta}{\partial z}. \tag{8-1}$$

In this expression the axial gradient of azimuthal vorticity appears explicitly as the source term for radial velocity. Therefore if there is no azimuthal vorticity gradient present, radial velocity remains zero. This holds true regardless how large the magnitude of azimuthal vorticity may be. Once again, this makes sense if we think in terms of a single row of discrete vortices. In this case, a net radial induction occurs only is the presence of a change in the relative strength of vortices, in the horizontal direction. If all the discrete vortices carry the same value of vorticity, then the radial induce velocity would be cancelled out by the sum of the neighboring vortices.

In the absence of the $\dfrac{u_r}{r^2}$ term, the left hand side of Equation (8-1), would be a Laplacian. In the present case, the equation can be solved for the radial velocity by using the Hankel transform with J_1 as a kernel (refer to Appendix C)

$$u_r(r,z) = -\frac{1}{2\pi} \int_{-\infty}^{\infty} dz' \int_0^{\infty} \frac{\partial \omega_\theta(r',z')}{\partial z'} \sqrt{\frac{r'}{r}} Q_{\frac{1}{2}} (\frac{r^2+r'^2+(z-z')^2}{2rr'}) dr' \tag{8-2}$$

where $Q_{\frac{1}{2}} = Q_{\frac{1}{2}}^0$ is the Legendre function of the second kind, of the zeroth degree and of

order $\frac{1}{2}$. It is further related to the hypergeometric function as

$$Q_{\frac{1}{2}}(z) = \pi 2^{\frac{-3}{2}} z^{\frac{-3}{2}} \left(\frac{5}{4},\frac{3}{4};2;z^{-2}\right) \tag{8-3}$$

where in the present case

$$z \equiv \frac{r^2+r'^2+(z-z')^2}{2rr'} > 1 \tag{8-4}$$

From the following integral representation of $Q_{\frac{1}{2}}$

$$Q_{\frac{1}{2}}(z) = \int_0^{\infty} \left[z^2 + (z^2-1)^{\frac{1}{2}} \cosh t \right]^{\frac{3}{2}} dt \tag{8-5}$$

In conjunction with Equation (8-4), it can be concluded that

$$Q_{\frac{1}{2}} > 0 \tag{8-6}$$

From the above derived relationship, a key conclusion can be made.

Noting that the term $Q_{\frac{1}{2}}(\frac{r^2+r'^2+(z-z')^2}{2rr'})$ is always positive, Equation (8-2) states that

when the gradient of azimuthal vorticity is negative everywhere inside the vortex tube, there will be a positive radial velocity. On the other hand, if the gradient of azimuthal vorticity is positive a negative radial velocity is generated, inducing radial contraction. It is important to note that the radial velocity at the observation point (r, z) should be the same as determined using Biot-Savart's law. In fact, the derivation of Biot-Savart's law and that of Equation (8-2) are intertwined, such that one can be obtained from the other. The powerful benefit of Equation (8-2), however, is that its derivation is not as cumbersome and is much more straightforward than that of Biot-Savart's law.

In order to give evidence to the aforementioned relationship, Equation (8-2) must be validated using the results of the modified vortex-filament method; similar to what was executed in the computational validation of Equation (5-1). Doing such, not only confirms Equation (8-2) but, more importantly, lends strong support to the many claims presented throughout this vortex breakdown investigation.

9   Conclusions and Recommendations

9.1   Conclusions

The self-induction theory of vortex breakdown was investigated using a refined and modified version of Cain's vortex-filament method. Through the use its improved simulations, this modified method has given further evidence that vortex breakdown is initiated by the development of an azimuthal vorticity gradient through an inviscid self-induction feedback mechanism. Though inviscid, this self-induction theory successfully demonstrates how the feedback mechanism and its central elements of radial expansion pile up, and vorticity sign-switching culminate in a turning point, the initial manifestation of vortex breakdown.

Unlike the many past experiments, the simulations of the modified vortex-filament method, offered in this report, have given rise to and highlighted the paramount mechanisms that initiate vortex breakdown while expounding ways of eliminating, delaying, or weakening breakdown. With this new paradigm of the inviscid self-induction process, we have not only taken big strides toward a general and complete understanding of breakdown, but have established a strong framework for future methods of controlling and exploiting the breakdown of vortex flow.

In this robust breakdown investigation, the many areas and rudiments of the formation stages of vortex breakdown have been examined and scrutinized. Although some findings were more far reaching and comprehensive than others, their combination presents a more inclusive overall picture of vortex breakdown, its many mechanisms, and how it can be controlled. A summary of these findings are highlighted below.

1. The modified vortex method, with its additive pitch-up velocity profile, models the explosion of the recirculation bubble phenomenon better than any former method, especially at the inner most radius.

2. In the formative stages of breakdown, reversed axial flow initiates at the inner most radius. This back flow leads to the establishment of a downstream stagnation point, which strengthens radially to form the upstream edge of the

recirculation bubble. Furthermore it is this initial explosion of the inner core which feeds the initial development of the recirculation bubble.

3. It is not the magnitude of the azimuthal vorticity component that determines vortex breakdown, but rather the existence of a differential change in azimuthal vorticity.   In fact, given enough time, even the smallest differential change will trigger the inviscid formative stages of breakdown. However, the stronger the differential change (stronger the azimuthal vorticity gradient) the more vigorous the breakdown process.

4. It is the inviscid self-induction process subjected to a prescribed negative vorticity gradient which causes the initial expansion of the vortex tube. Furthermore, this region of initial expansion, which was shown to start occur in the region of changing circulation, shifts upstream into the steady-state region of circulation with time. As the region of initial radial expansion further expands upstream, so does it feed the upstream movement of the negative azimuthal vorticity gradient region.

5. The vortex-filament method has given evidence to the claim that there is a unique relationship between the time of initial vortex tube expansion and the time of complete breakdown (determined by the existence of a turning point).   This suggests that once the inviscid self-induction mechanism causes a radial expansion, the subsequent process of breakdown is already predetermined.

6. Our many vortex breakdown simulations give support to the claims that the initial formative stages of the vortex breakdown phenomenon behave similar to the developing evolution of flow properties in a materializing shock-wave.

7. This investigation offered a local and dynamical relationship between the azimuthal vorticity gradient at a particular location and the curvature of the instantaneous streamline, projected onto the meridional plane, at the same location. This remarkable relationship affords simple method for calculating the azimuthal component of the complex three-dimensional vorticity vector at a particular location, in terms of the radius at that location.

8. The dynamical relationship was validated using the results of the vortex-filament method simulation. Moreover, it showed that a positive azimuthal vorticity gradient causes radial contraction of the vortex tube while a negative gradient indicates a region of radial expansion.

9. The vortex-filament method afforded the ability to physically trace evolution of and numerically calculate the helical angles of velocity and vorticity as a function of downstream location. The time evolution showed that the values of α and β reach a maximum value upstream, just aft of the vorticity source, and slowly decay thereafter. These maximum occur immediately after the conception of the vorticity sign-switch. Once established, these maximums maintain a constant value and their respective locations do not move downstream with time. This insight offers a possible control switch for controlling mechanisms.

10. A steadiness assessment of the transient vortex-filament method was performed by comparing the development of the azimuthal vorticity component along a streamline with the steady numerical predictions offered by Brown & Lopez. This assessment illustrated that the results of the vortex-filament method approaches the steady-state solution with time. Additionally, it illustrated that the trends obtained by Brown & Lopez's expression for azimuthal vorticity are opposite of those obtained by our local and dynamical expression. The accuracy of our expression improves with increasing radial distance and decreasing time, while Brown & Lopez improves with decreasing radial distance and increasing time.

11. Using results obtained earlier in this investigation along with past contributions, two specific control simulations were performed; the first adding opposite circulation and the second adding a positive vorticity gradient to the flow. Even in light of the transient nature of our simulation, both control cases, when compared to the baseline simulation, showed signs of either eliminating or delaying vortex breakdown.

9.2   Recommendations

Based on the findings in this study, several suggestions for future work are warranted:

1. Effort into the employment of the modified vortex tube should continue. Once employed, the comparison plots offered in Chapter 5 need to be recalculated with the hopes of eliminating the initial positive azimuthal vorticity gradient caused by the necking effects.

2. In order to further refine and improve the vortex-filament method, the method should be updated such that the vortex tube geometry is created at the vorticity source as a function of time. Doing such would allow both the circulation and velocity pitch-up to both be a function of time; further eliminating the many difficulties apparent in the present version of the method. Additionally, this improvement would reduce the size of the outputted data files while reducing the computational time required running the simulation.

3. An experimental study, using DPIV perhaps, needs to be performed to further validate the local and dynamical expression, presented earlier in this investigation.

4. Further simulations into the subjecting either a positive azimuthal vorticity gradient and/or opposite circulation to a vortex during the formative stages of breakdown should be explored.

5. The vortex-filament method should be modified to allow the additive regions of opposite circulation and positive vorticity gradient to transient downstream at a faster rate than that of the vortex tube. This would allow the controlling agent to catch up with the region of initial radial expansion, thus increasing its ability to either suppress and/or delay breakdown.

6. Experimental investigations into vortex breakdown at large Reynolds numbers need to be performed in order to further validate our simulation results and conclusions.

7.   Experimentally determine the contribution of the α_H term in Equation (5-5). Perhaps with the use of pressure sensitive paint (PSP).

LIST OF REFERENCES

1. NASA Dryden Flight Research Center, http://www.dfrc.nasa.gov/Gallery/Photo/F-18HARV/index.html, 1989.

2. NASA Langley Research Center, http://www.larc.nasa.gov/images/small/El-1996-00130.jpeg,1996.

3. Anderson, John D., *Fundamentals of Aerodynamics*, Third Edition, McGraw-Hill, Inc., New York, 2001.

4. Bertin, John J.,and Smith, M.L., *Aerodynamics for Engineers*, Prentice Hall, New Jersey, 1998.

5. Velinski, Oleg., "Review of Vortex Methods for Simulation of Vortex Breakdown." Defense Science and Technology Organization, Australia, 2001.

6. Nakamura, Y., Leonard, A., and Spalart, P.R., "Numerical Simulation of Vortex Breakdown by the Vortex-Filament Method." NASA Ames Research Center, Moffett Field, CA.

7. Cain, C.B., "The Self-Induction Theory of Vortex Breakdown", Masters Thesis, University of Washington Department of Aeronautics and Astronautics, 2001.

8. Leonard, A., "Vortex Methods for Flow Simulation", Journal of Computational Physics, Vol. 37, 1980, pp. 289-335.

9. Grabowski, W. J. and Berger, S. A., "Solutions of the Navier-Stokes Equations for Vortex Breakdown", Journal of Fluid Mechanics, 1976, oo. 525-544.

10. Brown, G.L., and J.M. Lopez, "Axisymmetric Vortex Breakdown. Part 2. Physical Mechanism", Journal of Fluid Mechanics, Vol 224, 1990, pp. 553-576.

11. Harvey, J.K., "Analysis of the Vortex Breakdown Phenomenon. Part 2", Imperial College, Aeronautical Department Report, 103, 1960.

12. Escudier, M.P., "Observations of the Flow Produced in a Cyclindrical Container by a Rotating Endwall", Experiments in Fluids, Vol. 2, 1984, pp. 189-196.

13. Faler, J.H., and Leibovich, S., "Disrupted States of Vortex Flow and Vortex Breakdown", Physics of Fluids, Vol. 20, No. 9, 1977, pp. 1385-1400.

14. Wimer, J.D., "A Digital Particle Image Velocimetry Investigation of Delta Wing Vortex Flow and Vortex Breakdown", Masters Thesis, University of Washington Department of Aeronautics and Astronautics, 2003.

15. Hamada, T., "The Effect of Flow Acceleration and Deccleration on Vortex Breakdown", B.S. Thesis, Miyazaki University, Japan, 2002.

16. Sarpkaya, T., " On stationary and travelling vortex breakdowns", Journal of Fluid Mechanics, Vol. 45, part 3, pp. 545-559, 1971.

17. Srigrarom, S., "On the Formation of Vortex Breakdown over Delta Wings", PhD Dissertation, University of Washington Department of Aeronautics and Astronautics, 2001.

18. Benjamin, T. B., "Theory of Vortex Breakdown Phenomenon", Journal of Fluid Mechanics, Vol. 144, 1962, pp. 593-629.

19. Keller, J.J., W. Egli, and J. Exley, "Force and Loss-Free Transitions Between Flow States", Journal of Applied Physics, Vol. 36, 1985, pp. 854-889.

20. Strunk, W., and White, E. B., *The Elements of Style*, Third Edition, MacMillian Publishing Co., Inc., New York, 1979.

Appendix A – Local and Dynamical Relationship Derivation

In this section we derive the relationship between the gradient of azimuthal vorticity and the radius of curvature of the instantaneous streamline by writing the principal equations in the streamline coordinate system. If we project the three-dimensional and instantaneous stream surface onto the meridional plane, we introduce a new streamline coordinate system. The streamline coordinates (s,n) are define such that s is the distance along the instantaneous streamline and n, normal to it. Furthermore, for any quantity, F,

$$\frac{\partial F}{\partial r} = \frac{\partial F}{\partial n}\cos\theta_m + \frac{\partial F}{\partial s}\sin\theta_m \tag{A-1}$$

$$\frac{\partial F}{\partial z} = -\frac{\partial F}{\partial n}\sin\theta_m + \frac{\partial F}{\partial s}\cos\theta_m \tag{A-2}$$

Where θ_m is the angle between a tangent to the instantaneous projected streamline and the z-axis. Additionally, the following continuity equation for axisymmetric flow

$$\frac{1}{r}\frac{\partial(ru_r)}{\partial r} + \frac{\partial u_z}{\partial z} = 0, \tag{A-3}$$

Can be rewritten in the streamline coordinate system, as

$$\frac{\partial(rq_m)}{\partial s} + rq_m\frac{\partial\theta_m}{\partial n} = 0, \tag{A-4}$$

where q_m is the meridional velocity

$$q_m = \sqrt{u_r^2 + u_z^2}, \tag{A-5}$$

Next, we write the equation of motion as

$$\frac{\partial \vec{u}}{\partial t} = \text{grad}H - \vec{u}\times\vec{\omega} = 0 \tag{A-6}$$

Where H is the total head, $H = \frac{P}{\rho} + \frac{\vec{u}^2}{2}$, and $\vec{\omega}$ the vorticity. The azimuthal component of the equation of motion may be expressed in the streamline coordinates

$$\frac{\partial C}{\partial t} + q_m\frac{\partial C}{\partial s} = 0 \tag{A-7}$$

Where C is the location circulation. The radial and axial components of (A-6) are

$$\frac{\partial u_r}{\partial t} + \frac{\partial H}{\partial r} + \left(u_z \omega_\theta - \frac{u_\theta}{r} \frac{\partial (r u_\theta)}{\partial r} \right) = 0 \tag{A-8}$$

$$\frac{\partial u_z}{\partial t} + \frac{\partial H}{\partial r} + \left(-u_r \omega_\theta - \frac{u_\theta}{r} \frac{\partial (r u_\theta)}{\partial z} \right) = 0 \tag{A-9}$$

If one multiplies (A-8) by u_z and (A-9) by u_r, and then subtracting one from the other, the following is reached

$$\omega_\theta + \frac{\partial \theta_m}{\partial t} - \frac{1}{8\pi^2 r^2 q_m} \frac{\partial C^2}{\partial n} + \frac{1}{q_m} \frac{\partial H}{\partial n} = 0 \tag{A-9}$$

Differentiating (A-9) by s and combining the result with (A-3), you reach

$$\frac{\partial \omega_\theta}{\partial s} - \frac{1}{r_m^2} \frac{\partial r_m}{\partial t} - \frac{1}{8\pi^2} \frac{\partial}{\partial s}\left(\frac{1}{r^2 q_m} \frac{\partial C^2}{\partial n} \right) + \frac{\partial}{\partial s}\left(\frac{1}{q_m} \frac{\partial H}{\partial n} \right) = 0 \tag{A-10}$$

It is important to note that in deriving (A-10), the below relationship is used

$$\frac{\partial \theta_m}{\partial s} = \frac{1}{r_m} \tag{A-11}$$

Where r_m is the radius of curvature of the instantaneous streamline,

$$\frac{1}{r_m} = \frac{\dfrac{d^2 r}{dz^2}}{\left[1 + \left(\dfrac{dr}{dz} \right)^2 \right]^{\frac{3}{2}}} \tag{A-12}$$

Finally, the radius of curvature is defined such that positive curvature refers to the streamline being concave downwards, and thus, negative when concave upwards.

Appendix B – Deriving and Solving for α_c Term

In this section we derive the expression for the α_c term which is used in Equation (4-4). Staring from the governing vorticity principle $\text{div}\,\vec{\omega} \equiv 0$ and expanding can obtain

$$0 = \iiint_V \text{div}\,\vec{\omega}\,dv = \iint_S \vec{\omega} \cdot \vec{n}\,ds \tag{B-1}$$

where $\vec{n}$ is a unit vector pointing outwards. Since Equation (B-1) involves a surface and volume integral it is important to first define our volume and respective surface components. The volume of interest and surfaces are illustrated in Figure B-1.
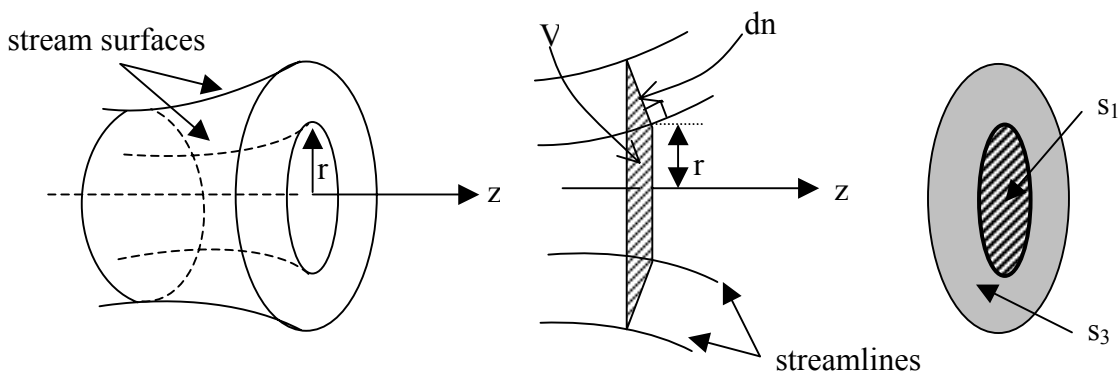
Figure B-1: Elements of stream surfaces and streamlines

To evaluate the surface integral in Equation (B-1), we break down surface integrals to each respective surface, shown in Figure B-2, and obtain the following expression for each of the three respective surfaces

$$s = s_1 + s_2 + s_3$$
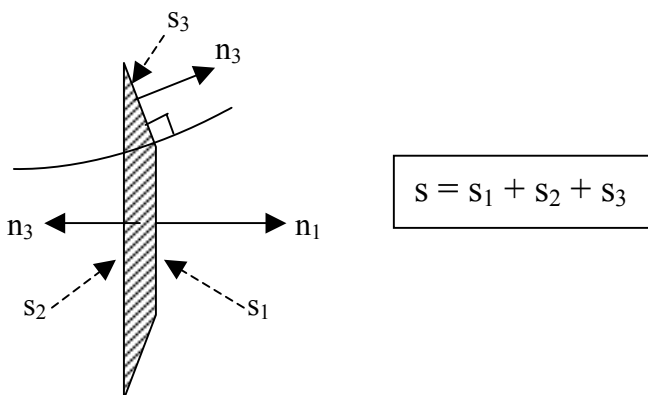
Figure B-2: Surface integral components

$$\iint_{S_1} \overset{\rho}{\omega}_1 \cdot \overset{\rho}{n}_1 \, ds_1 = C \tag{B-2}$$

$$\iint_{S_2} \overset{\rho}{\omega}_2 \cdot \overset{\rho}{n}_2 \, ds_2 = -(C + dC) \tag{B-3}$$

$$\iint_{S_3} \overset{\rho}{\omega}_3 \cdot \overset{\rho}{n}_3 \, ds_3 = 2\pi r dn \cdot \omega_s \tag{B-4}$$

where ω_s refers to the streamline component of ω_m, the meridional projection of $\overset{\nu}{\omega}$ and dC corresponds to a change in stream surfaces separated by dn shown in

Figure B-1.
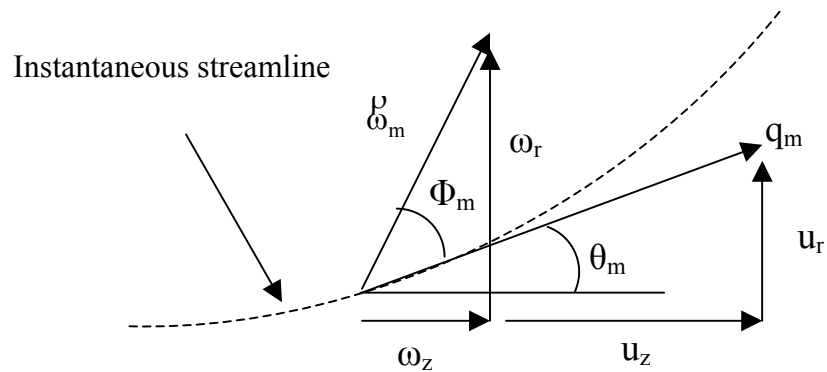
Figure B-3: Vector components and angles of meridional streamline

Using the relationships illustrated in Figure B-3, we also know the following component expression for vorticity and velocity, for the meridional streamline.

$$\omega_s = \omega_m \cos \Phi_m \tag{B-5}$$

$$\omega_m = \sqrt{\omega_z^2 + \omega_r^2} \tag{B-6}$$

$$q_m = \sqrt{u_z^2 + u_r^2} \tag{B-7}$$

Having obtained the above vorticity and velocity component expressions, we can substitute into each of the three component surface integrals. When this is done the following is reached

$$C - (C + dC) + 2\pi r dn \cdot \omega_s = 0 \tag{B-8}$$

From this, we obtain the expression for the partial derivative of circulation with respect to n.

$$\frac{\partial C}{\partial n} = 2\pi r \omega_s \tag{B-9}$$

We can now substitute this derivative directly into the expression for α_c, Equation B-10, which was derived in Appendix A, as

$$\alpha_c = \frac{1}{4\pi^2} \frac{\partial}{\partial s} \left[\frac{C}{r^2 q_m} \frac{\partial C}{\partial n} \right] \tag{B-10}$$

Furthermore, substituting Equation (B-5) into (B-10), gives the following

$$\alpha_c = \frac{1}{4\pi^2} \frac{\partial}{\partial s} \left[\frac{C}{r^2 q_m} 2\pi r \omega_m \cos \Phi_m \right] \tag{B-11}$$

Next, by noting $C = 2\pi r u_\theta$,

$$\alpha_c = \frac{1}{4\pi^2} \frac{\partial}{\partial s} \left[\frac{2\pi r u_\theta}{r^2 q_m} 2\pi r \omega_m \cos \Phi_m \right] \tag{B-12}$$

Finally, we can cancel like terms and obtain the simplified expression for α_c,

$$\alpha_c = \frac{\partial}{\partial s}\left[\frac{u_\theta \omega_m \cos\Phi_m}{q_m}\right] \tag{B-13}$$

It is important to note that value of Φ_m can be determined by using the combination of the following expressions

$$\tan\theta_m = \frac{u_r}{u_z} \tag{B-14}$$

$$\tan(\theta_m + \Phi_m) = \frac{\omega_r}{\omega_z} \tag{B-15}$$

Appendix C – Additional Analytical Expression Derivation
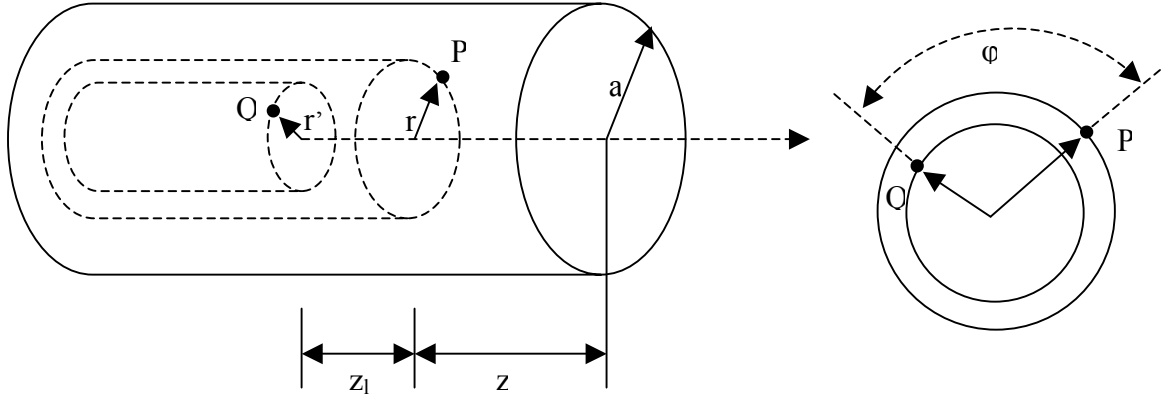
Figure C-1: Vortex tube geometry

For a vortex tube of radius a, we calculate the radial velocity inducted at point P(r, z) induced by the vorticity at the source point Q located at radius r' and separated axially from the point P by a distance z_l. The vorticity is in the axial direction and its magnitude ω_{θ_o} is constant throughout the vortex tube. Outside of the vortex tube, which is open-ended at z=0, the vorticity is either at r>a or z>0.

By applying Biot-Savart's law, the radial velocity at P, which is axisymmetric is give by

$$u_r(r,z) = -\frac{\omega_{\theta_o}}{4\pi} \int_0^a r'dr' \int_{-\pi}^{\pi} \cos\phi I_r d\phi \qquad (C-1)$$

where

$$I_r \equiv \int_{-\infty}^{-z} \frac{z_l dz_l}{(r'^2 - 2r'r\cos\phi + r^2 + z_l^2)^{\frac{3}{2}}} \qquad (C-2)$$

which may be integrated as

$$I_r \equiv \frac{1}{\sqrt{(r'^2 - 2r'r\cos\phi + r^2 + z_l^2)}} \qquad (C-3)$$

Therefore

$$u_r(r,z) = \frac{\omega_{\theta_o}}{4\pi} \int_0^a I_{rl} r' dr' \tag{C-4}$$

where

$$I_{rl} \equiv \int_{-\pi}^{\pi} \frac{\cos\phi}{\sqrt{(r'^2 - 2r'r\cos\phi + r^2 + z_l^2)}} d\phi \tag{C-5}$$

Making the change integral variable, I_{rl} may be written further as

$$I_{rl} \equiv -\frac{4}{\sqrt{(r'+r)^2 + z^2}} I_{rl}^{(1)} + 8 \frac{r'^2 + r^2 + z^2}{\left[(r'+r)^2 + z^2\right]^{3/2}} I_{rl}^{(2)} \tag{C-6}$$

where

$$I_{rl}^{(1)} = \int_0^{\pi/2} \sqrt{1 - k^2 \sin^2\psi} \, d\psi \tag{C-7}$$

$$I_{rl}^{(2)} = \int_0^{\pi/2} \frac{\sin^2\psi}{\sqrt{1 - k^2 \sin^2\psi}} \, d\psi \tag{C-8}$$

$I_{rl}^{(1)}$ and $I_{rl}^{(2)}$ may be expressed, respectively, as

$$I_{rl}^{(1)} = E(k) \tag{C-9}$$

$$I_{rl}^{(2)} = \frac{1}{k^2 \left[K(k) - E(k)\right]} \tag{C-10}$$

Substituting Equation (C-9) and (C-10) into Equation (C-6) yields

$$I_{rl} = \frac{2}{r'\sqrt{(r'+r)^2 + z^2}} \left\{ -2r'E(k) + \frac{r'^2 + r^2 + z^2}{r} \left[K(k) - E(k)\right] \right\} \tag{C-11}$$

Finally, when we substitute the above Equation (C-11) into Equation (C-4), Equation (7-2) in the main text is reached

Appendix D – Modified Vortex-Filament Method Codes

D.1   Vlinec_rad_spoke_wfj Main Code

```
//-----------------------------------------------------------------------------
// This code is a modified version of CB Cain's original vortex-filament
// method (2001).  It was modified to incorporate multiple features to
// include variable velocity ramp-up profile (temporal ramp-up) and azimuthal
// vorticity calculation at the vorticity source.  The code uses internal
// packages which are required by Borland Builder C++.  However, the code as
// been restructured to such that it can be complied and executed by other
// programs, such as Microsoft Visual C++.
//
// Update WFJ Version 9.1
// August 2003
//-----------------------------------------------------------------------------


// Internal Call Packages
//------------------------
#include <vcl.h>
#include <fstream.h>
#include <istream.h>
#include <iostream.h>
#include <conio.h>
#include <fastmath.h>
#include <time.h>
//------------------------

#pragma hdrstop

// Initialize All Required Subroutines
//-------------------------------------

int read_data ();
int init ();
void cond_out(char*);
int out(double**, double**, double**, char*, int, int);
int out2(double**, char*, int, int);
void calc_ind ();
void r_calc_ind ();
void init_ind();
void u_update();
void sym_calc();
void r_sym_calc();
void init_incase_rad_spoke(int,double**, double**, double**,double**,double,
int,int*,int,int,double*,double,double,double,double,double,
double,double,double**,double**,double**,double**,int,int,int);

//  Declare Global Variables
//-------------------------------------------------------------------------
int in_case,velvor_on,blow_on,n_fil,wall_on,wall_ax_node,wall_circ_node;
double t_final,U_inf,beta,r_tube0,r_tube1,r_tube2,r_tube3,r_tube4,r_tube5,
```

```
      r_tube6,r_tube7,r_tube8,r_tube9,r_tube10,r_tube11,r_tube12;
      double sigma_init,C,alpha,U;
      double z_on,z_init,x_init,y_init,dz,dt,t_v_out,x_cent,z_start;
      int t_index, *on_node, max_node,out_skip,t_out_start,out_count,x_nodes,
      z_nodes,end_fix,*r_fil,n_rad,r_fil_in,r_n_fil,r_max_node,r_on_fil;
      double t_real,pi,*core_con,*r_tube;
      int n_spokes,counter;
      char *r_node_out,*r_sigma_out,*gamma_out,*r_gamma_out,*node_out,*sigma_out,
      *tan_omega_out, *Utheta_out, *wz_out, *ommega_theta_out;
      double u_induced_x,u_induced_y,u_induced_z, *U_instant;
      double *Update_C, *Radius;
      double **x_n, **y_n, **z_n, **u_induced_total_x, **u_induced_total_y,
      **u_induced_total_z, **sigma;
      double **gamma,start_C_inc,stop_C_inc,C_min;
      double **r_gamma,**r_x_n, **r_y_n, **r_z_n, **r_u_induced_total_x,
      **r_u_induced_total_y, **r_u_induced_total_z, **r_sigma,**r_core_con,
      **r_seg_length;
      double **Utheta, **wz, **tan_omega, **ommega_theta;
      int main(int argc, char **argv){


      //  Define Data Output Files
      //----------------------------
      node_out = "vlinec.dat";
      sigma_out = "sigma_out.dat";
      r_node_out = "r_vlinec.dat";
      r_sigma_out = "r_sigma_out.dat";
      gamma_out = "gamma_out.dat";
      r_gamma_out = "r_gamma_out.dat";
      tan_omega_out = "tan_omega_out.dat";
      Utheta_out = "Utheta_out.dat";
      wz_out = "wz_out.dat";
      ommega_theta_out = "ommega_theta_out.dat";

      int c1 = clock();
      read_data(); //read input file

      init();

      //  Initialize Program Variables (above) and output messages to screen
      //---------------------------------------------------------------------
      cout << "USE FOR CASES THAT ARE ALWAYS SYMMETRIC ONLY!" <<endl;
      cout << "T_final: "<<t_final << endl;
      cout << "Total iterations: "<<t_final/dt << endl;
      cout << "Max nodes: " <<max_node << endl;
      cout << "U_inf: "<<U_inf << endl;
      cout << "dz: "<<dz << endl;
      cout << "Initial condition case: "<<in_case << endl;

      // Initialize Output Files. Note that the program is strcuture such that
      // the output files are continually written over
      //----------------------------------------------------------------------

      ofstream outfile(node_out, ios::trunc);
```

```
if (!outfile) {
cout <<"Error opening output file"<<endl;}
outfile.close();

ofstream sigmafile(sigma_out, ios::trunc);
if (!sigmafile) {
cout <<"Error opening output file"<<endl;}
sigmafile.close();

ofstream r_outfile(r_node_out, ios::trunc);
if (!r_outfile) {
cout <<"Error opening output file"<<endl;}
r_outfile.close();

ofstream r_sigmafile(r_sigma_out, ios::trunc);
if (!r_sigmafile) {
cout <<"Error opening output file"<<endl;}
r_sigmafile.close();

ofstream gammafile(gamma_out, ios::trunc);
if (!gammafile) {
cout <<"Error opening output file"<<endl;}
gammafile.close();

ofstream r_gammafile(r_gamma_out, ios::trunc);
if (!r_gammafile) {
cout <<"Error opening output file"<<endl;}
r_gammafile.close();

ofstream tan_omegafile(tan_omega_out, ios::trunc);
if (!tan_omegafile) {
cout <<"Error opening output file"<<endl;}
tan_omegafile.close();

ofstream Utheta_outfile(Utheta_out, ios::trunc);
if (!Utheta_outfile) {
cout <<"Error opening output file"<<endl;}
Utheta_outfile.close();

ofstream wz_outfile(wz_out, ios::app);
if (!wz_outfile) {
cout <<"Error opening output file"<<endl;}
wz_outfile.close();

ofstream ommega_theta_outfile(ommega_theta_out, ios::app);
if (!ommega_theta_outfile) {
cout <<"Error opening output file"<<endl;}
ommega_theta_outfile.close();

// Output Simulation Time to Screen
//------------------------------------
cout << "t_index: "<< t_index << "  " << "t_real: "<<t_real << endl;

// Write Program Inputs to 1st Row of Output File
```

```
//-------------------------------------------------
cond_out(node_out);
cond_out(sigma_out);
cond_out(gamma_out);

//  Write Vortex Filament Node Position to File
//-------------------------------------------------
out(x_n,y_n,z_n,node_out,max_node,n_fil); //main vortex tube
out(r_x_n,r_y_n,r_z_n,r_node_out,r_max_node,r_n_fil); //radial spokes

//  Write Vortex Filament Core Radius to File
//-------------------------------------------------
out(sigma,sigma,sigma,sigma_out,max_node,n_fil); //main vortex tube
out(r_sigma,r_sigma,r_sigma,r_sigma_out,r_max_node,r_n_fil); //radial spokes

//  Write Vortex Filament Circulation to File
//-------------------------------------------------
out(gamma,gamma,gamma,gamma_out,max_node,n_fil); //main vortex tube
out(r_gamma,r_gamma,r_gamma,r_gamma_out,r_max_node,r_n_fil); //radial spokes




//  Set-Up Velocity Profile.  Note that the Circulation Profile must also be
//  ajusted in the "in_case_rad_spoke" file which sets-up the vortex tube
//  filament/node position.
//  I realize that this method of implementation is rather old-style, but it
//  allow for quick changes in profile and allows for any possible profile.


//                  for (int m = 0; m <= 1; m++){
//                  U_instant[m] = 0.0;
//                  Update_C[m] = 0.0;
//                      }

                    for (int mm = 0; mm <= 19; mm++){
                     U_instant[mm] = 0.25 * (mm+1);
                    Update_C[mm] = (mm+1);
                    }

                    for  (int c = 20; c <= 200; c++){
                    U_instant[c] = 5.0;
                    Update_C[c] = 20.0;
                     }


                    for (int c = 0; c<=19; c++){
                    Radius[c] = (c*0.1)+0.1;
                     }

                    for (int m = 0; m <= 200; m++) {
                    for (int i = 0; i <= 19; i++){

                    Utheta[m][i] = ((Update_C[m]*(1.0-(exp(-1.0*10.9*Radius[i]*
                    Radius[i])))/ (2.0*3.1415*Radius[i]));
```

```
                }
                }

                for (int m = 0; m <= 200; m++) {
                for (int i = 0; i <= 19; i++){
                tan_omega[m][i] = Utheta[m][i] / U_instant[m];
                }
                                                            }
                 int row=201;
                int col=20;

                 for (int m = 0; m <= 200; m++){
                 for (int i = 0; i <= 19; i++){
                wz[m][i] = (Update_C[m]*10.9*(exp(-10.9*pow(Radius[i],2))))/
             (PI);
                }
                }

                for (int m = 0; m <= 200; m++){
                for (int i = 0; i <= 19; i++){
                ommega_theta[m][i] = wz[m][i]*tan_omega[m][i];
                }
                }

out2(tan_omega,tan_omega_out,row,col);
out2(Utheta,Utheta_out,row,col);
out2(wz, wz_out,row,col);
out2(ommega_theta, ommega_theta_out,row,col);

//-----------------Begin main program loop-------------------------------

while (t_real < t_final-dt) {


calc_ind();  //calculate induced velocity on vortex filament nodes

t_index = t_index + 1;
t_real = t_real + dt;
counter = counter +1;


//write current simulation time to screen
int c2 = clock();
cout << "t_index: "<< t_index<<" t_real: "<<t_real << " run time: " <<
double(c2-c1)/CLK_TCK << endl;

//write output to file
if (t_index >= t_out_start && t_index == out_count*out_skip){
     cout <<endl;
     cout<<"Writing node position to file, t_index= "<< t_index<<endl;
     cout <<endl;
     cout <<"Code Updated!"<<endl;
     cout <<endl;
```

```
            cout <<"U_instant ="<<U_instant[counter]<<endl;
            cout <<"Final WFJ Code... Updated!"<<endl;
            cout <<endl;

    //write vortex filament node position to file
    out(x_n,y_n,z_n,node_out,max_node,n_fil); //main vortex tube
    out(r_x_n,r_y_n,r_z_n,r_node_out,r_max_node,r_n_fil); //radial spokes

    //write vortex filament core radius to file
    out(sigma,sigma,sigma,sigma_out,max_node,n_fil); //main vortex tube
    out(r_sigma,r_sigma,r_sigma,r_sigma_out,r_max_node,r_n_fil); //radial spokes

    //write vortex filament circulation to file
    out(gamma,gamma,gamma,gamma_out,max_node,n_fil); //main vortex tube
    out(r_gamma,r_gamma,r_gamma,r_gamma_out,r_max_node,r_n_fil); //radial spokes

    out_count = out_count + 1;  //index for writing output to file
        }
}
int c3 = clock();
cout << endl;
cout <<"Total run time: "<< double(c3-c1)/CLK_TCK << endl;
cout << endl << "Press any key to continue...";
getch();

outfile.close();

return 0;
}
//-------------------------------------------------------------------------


//----------------Function read_data -------------------------------------
//Read data from vlinec.inp.  Input file requires '$' characters and end of line
//-------------------------------------------------------------------------
int read_data ()
{
    ifstream infile("vlinec_rad_spoke.inp", ios::in);
        if (!infile) return 0;
    infile.ignore(10000, '$');
    infile >> in_case;infile.ignore(1000, '\n');
    infile >> t_final;infile.ignore(1000, '\n');
    infile >> U_inf;infile.ignore(1000, '\n');
    infile >> dz;infile.ignore(1000, '\n');
    infile >> dt;infile.ignore(1000, '\n');
    infile >> max_node;infile.ignore(1000, '\n');
    infile >> r_fil_in;infile.ignore(1000, '\n');
    infile >> n_rad;infile.ignore(1000, '\n');
    infile >> t_out_start;infile.ignore(1000, '\n');
    infile >> out_skip;infile.ignore(1000, '\n');
    infile >> r_tube0;infile.ignore(1000, '\n');
    infile >> r_tube1;infile.ignore(1000, '\n');
    infile >> r_tube2;infile.ignore(1000, '\n');
    infile >> r_tube3;infile.ignore(1000, '\n');
```

```
        infile >> r_tube4;infile.ignore(1000, '\n');
        infile >> r_tube5;infile.ignore(1000, '\n');
        infile >> r_tube6;infile.ignore(1000, '\n');
        infile >> r_tube7;infile.ignore(1000, '\n');
        infile >> r_tube8;infile.ignore(1000, '\n');
        infile >> r_tube9;infile.ignore(1000, '\n');
        infile >> r_tube10;infile.ignore(1000, '\n');
        infile >> r_tube11;infile.ignore(1000, '\n');
        infile >> r_tube12;infile.ignore(1000, '\n');
        infile >> sigma_init;infile.ignore(1000, '\n');
        infile >> C;infile.ignore(1000, '\n');
        infile >> start_C_inc;infile.ignore(1000, '\n');
        infile >> stop_C_inc;infile.ignore(1000, '\n');
        infile >> C_min;infile.ignore(1000, '\n');
        infile >> alpha;infile.ignore(1000, '\n');
        infile >> z_on;infile.ignore(1000, '\n');
        infile >> z_init;infile.ignore(1000, '\n');
        infile >> x_init;infile.ignore(1000, '\n');
        infile >> y_init;infile.ignore(1000, '\n');
        infile.close();
        return 0;
}

//-----------------Function init -----------------------------------------
//Initialize variables
//-------------------------------------------------------------------------

int init ()
{
        r_fil = new int [n_rad];
        r_tube = new double [n_rad];
        U_instant = new double [t_final/dt];
        Update_C = new double [t_final/dt];
        Radius = new double [20];
        n_fil = 0;

        //initialize number of filaments in a given radius
        r_fil[0] = r_fil_in;
        r_fil[1] = r_fil_in;
        r_fil[2] = r_fil_in;
        r_fil[3] = r_fil_in;
        r_fil[4] = r_fil_in;
        r_fil[5] = r_fil_in;
        r_fil[6] = r_fil_in;
        r_fil[7] = r_fil_in;
        r_fil[8] = r_fil_in;
        //r_fil[9] = r_fil_in;
        //r_fil[10]= r_fil_in;
        //r_fil[11]= r_fil_in;
        //r_fil[12]= r_fil_in;

        //Initiallize vortex filament radii
        r_tube[0]=r_tube0;
        r_tube[1]=r_tube1;
```

```
r_tube[2]=r_tube2;
r_tube[3]=r_tube3;
r_tube[4]=r_tube4;
r_tube[5]=r_tube5;
r_tube[6]=r_tube6;
r_tube[7]=r_tube7;
r_tube[8]=r_tube8;
//r_tube[9]=r_tube9;
//r_tube[10]=r_tube10;
//r_tube[11]=r_tube11;
//r_tube[12]=r_tube12;

for (int j = 0; j <= n_rad-1; j++){
n_fil = r_fil[j]+n_fil;
}
n_fil = n_fil + 1; //add centerline filament
double **seg_length = new double *[max_node];
for (int i = 0;i<max_node;i++){seg_length[i]= new double [n_fil];}

//initialize simulation time
t_real = 0.0;
t_index = 0;
out_count = 1;

pi = M_PI;//define pi

z_init = z_init + dz;

//Initiallize dynamic arrays
core_con = new double [n_fil];

on_node = new int [n_fil];

Utheta = new double *[201];
for (int i = 0;i<201;i++){Utheta[i]= new double [20];}

wz = new double *[201];
for (int i = 0;i<201;i++){wz[i]= new double [20];}

tan_omega = new double *[201];
for (int i = 0;i<201;i++){tan_omega[i]= new double [20];}

ommega_theta = new double *[201];
for (int i = 0;i<201;i++){ommega_theta[i]= new double [20];}

gamma =  new double *[max_node];
for (int i = 0;i<max_node;i++){gamma[i]= new double [n_fil];}

x_n =  new double *[max_node];
for (int i = 0;i<max_node;i++){x_n[i]= new double [n_fil];}

y_n = new double *[max_node];
for (int i = 0;i<max_node;i++){y_n[i]= new double [n_fil];}
```

```
z_n = new double *[max_node];
for (int i = 0;i<max_node;i++){z_n[i]= new double [n_fil];}

u_induced_total_x = new double *[max_node];
for (int i = 0;i<max_node;i++){u_induced_total_x[i]=
new double [n_fil];}

u_induced_total_y = new double *[max_node];
for (int i = 0;i<max_node;i++){u_induced_total_y[i]=
new double [n_fil];}

u_induced_total_z = new double *[max_node];
for (int i = 0;i<max_node;i++){u_induced_total_z[i]=
new double [n_fil];}

sigma = new double *[max_node];
for (int i = 0;i<max_node;i++){sigma[i]= new double [n_fil];}

//radial spokes arrays and locations

int m_z = 10;
n_spokes = 16;
r_n_fil = 10*n_spokes;
r_max_node = 5/0.1;

r_gamma =  new double *[r_max_node];
for (int i = 0;i<r_max_node;i++){r_gamma[i]= new double [r_n_fil];}

r_x_n =  new double *[r_max_node];
for (int i = 0;i<r_max_node;i++){r_x_n[i]= new double [r_n_fil];}

r_y_n = new double *[r_max_node];
for (int i = 0;i<r_max_node;i++){r_y_n[i]= new double [r_n_fil];}

r_z_n = new double *[r_max_node];
for (int i = 0;i<r_max_node;i++){r_z_n[i]= new double [r_n_fil];}

r_u_induced_total_x = new double *[r_max_node];
for (int i = 0;i<r_max_node;i++){r_u_induced_total_x[i]=
new double [r_n_fil];}

r_u_induced_total_y = new double *[r_max_node];
for (int i = 0;i<r_max_node;i++){r_u_induced_total_y[i]=
new double [r_n_fil];}

r_u_induced_total_z = new double *[max_node];
for (int i = 0;i<r_max_node;i++){r_u_induced_total_z[i]=
new double [r_n_fil];}

r_sigma = new double *[r_max_node];
for (int i = 0;i<r_max_node;i++){r_sigma[i]= new double [r_n_fil];}

r_core_con = new double *[r_max_node];
for (int i = 0;i<r_max_node;i++){r_core_con[i]= new double [r_n_fil];}
```

```
        r_seg_length = new double *[r_max_node];
        for (int i = 0;i<r_max_node;i++){r_seg_length[i]= new double [r_n_fil];}

        //Initialize x_n, y_n, z_n
        //Note: z_n is to the right (axial direction), x_n is up,
        //y_n is out of page.  When plotting, plot z_n to the right, x_n up,
        //and y_n out of page.

//subroutine in init_incase_rad_spoke.cpp that initializes vortex filament
//node location
init_incase_rad_spoke(in_case,x_n,y_n,z_n,gamma,C,max_node,r_fil,n_fil,n_rad,
r_tube,x_init,y_init,z_init,dz,start_C_inc,stop_C_inc,C_min,
r_gamma,r_x_n,r_y_n,r_z_n,r_max_node,n_spokes,m_z);



        //Intialize sigma, find core constant to maintain constant volume in
        //vortex filament segment.  This allows simulation to handle vortex
        //stretching
        for (int n = 0; n <= n_fil-1; n++){
            for (int m = 0; m <= max_node-2; m++){

            sigma[m][n] = sigma_init;
            seg_length[m][n] = sqrt((x_n[m+1][n]-x_n[m][n])*
            (x_n[m+1][n]-x_n[m][n])+(y_n[m+1][n]-y_n[m][n])*(y_n[m+1][n]-
            y_n[m][n])+(z_n[m+1][n]-z_n[m][n])*(z_n[m+1][n]-z_n[m][n]));
            }

            core_con[n] = sigma[1][n]*sigma[1][n]*seg_length[1][n];
        }

        //intialize sigma for radial spokes
        for (int n = 0; n <= r_n_fil-1; n++){
          for (int m = 0; m <= r_max_node-2; m++){
            r_sigma[m][n] = sigma_init;

            r_seg_length[m][n] = sqrt((r_x_n[m+1][n]-r_x_n[m][n])*
            (r_x_n[m+1][n]-r_x_n[m][n])+(r_y_n[m+1][n]-r_y_n[m][n])*
            (r_y_n[m+1][n]-r_y_n[m][n])+(r_z_n[m+1][n]-r_z_n[m][n])*
            (r_z_n[m+1][n]-r_z_n[m][n]));

            r_core_con[m][n] = r_sigma[m][n]*r_sigma[m][n]*
            r_seg_length[m][n];
          }
        }

        return 0;

}


//-----------------Function cond_out---------------------------------------
// Write inputs to 1st row of output file
//-------------------------------------------------------------------------
```

```cpp
void cond_out(char *out)
{
    ofstream outfile(out, ios::app);
    //need to fill 34 columns
    //output simulation variable to top row of output file
    outfile << in_case << " "<< n_fil << " "<<max_node<< " "<<dt << " "
    << dz << " "<< U_inf << " "<< t_out_start << " "<< out_skip << " "
    << r_tube1 << " "<< r_tube2 << " "<< r_tube3 << " " <<r_tube4<< " "
    << r_tube5 << " "<< sigma_init << " "<< C << " "<< alpha << " "
    << z_on << " "<< n_rad << " "<< r_fil[0] << " "<< r_fil[1]<< " "
    << r_fil[2]<< " " <<r_fil[3]<< " "<<r_fil[4]<< " "<< r_fil[5]<< " "
    << r_fil[6]<< " " <<r_fil[7]<< " "<<r_fil[8]<< " "<< r_fil[9]<< " ";
    for (int p=29 ; p<=n_fil+1 ; p++){outfile << 0 << " ";}
    outfile<< endl;

}
//----------------Function out--------------------------------------------
// Write x_n, y_n, z_n to file
//-------------------------------------------------------------------------

int out(double**a, double**b, double**c, char*out, int m_row, int n_col)
{
    ofstream outfile(out, ios::app);
    if (!outfile) return 0;
    //output x_n
    for (int m = 0; m <= m_row-1; m++){
        for (int n = 0; n <= n_col-1; n++){
        outfile.precision(6);
        outfile << a[m][n] << " ";
        }
        outfile << t_index <<endl;
    }
    //output y_n
    for (int m = 0; m <= m_row-1; m++){
        for (int n = 0; n <= n_col-1; n++){
        outfile.precision(6);
        outfile << b[m][n] << " ";
        }
        outfile << t_index <<endl;
    }
    //output z_n
    for (int m = 0; m <= m_row-1; m++){
        for (int n = 0; n <= n_col-1; n++){
        outfile.precision(6);
        outfile << c[m][n] << " ";
        }
        outfile << t_index <<endl;
    }
    //outfile.close();
    return 0;
}

//----------------Function out--------------------------------------------
// Write tan_omega data file
```

```
//----------------------------------------------------------------------

int out2(double**a, char*out, int m_row, int n_col)
{
     ofstream outfile(out, ios::app);
     if (!outfile) return 0;
     //output x_n

     for (int m = 0; m<=m_row-1; m++){
       for (int n = 0; n <+ n_col; n++){
       outfile.precision(6);
       outfile << a[m][n] << "   ";
       }
       outfile <<endl;

   //  for (int m = 0; m <= m_row-1; m++){
   //      for (int n = 0; n <= n_col-1; n++){
   //      outfile.precision(6);
   //      outfile << a[m][n] << " ";
   //      }

    }

     //outfile.close();
     return 0;
}




//-----------------Function calc_ind----------------------------------------
// Perform induced velocity calculations
//----------------------------------------------------------------------
void calc_ind()
{
init_ind();

     //calculate induced velocity on each node from every other vortex
     //filament segment
     int n;
     for (int j1 = 0; j1 <= n_rad; j1++){

     if (j1==0){n = 0;}
     else if (j1==1){n = 1;}
     else if (j1 > 1){n = r_fil[j1-2]+ n;}

       for (int m = 0; m <= on_node[n]-1; m++){
         for (int k = 0; k <= n_fil-1; k++){
           for (int j = 0; j <= on_node[k]-2; j++){

double gam_eq;

double dlx = x_n[j+1][k]-x_n[j][k];
double dly = y_n[j+1][k]-y_n[j][k];
```

```
double dlz = z_n[j+1][k]-z_n[j][k];

double rx = x_n[m][n] - (0.5*(x_n[j+1][k] - x_n[j][k]) + x_n[j][k]);
double ry = y_n[m][n] - (0.5*(y_n[j+1][k] - y_n[j][k]) + y_n[j][k]);
double rz = z_n[m][n] - (0.5*(z_n[j+1][k] - z_n[j][k]) + z_n[j][k]);

double r_cross_dr_x = rz*dly - ry*dlz;
double r_cross_dr_y = -(rz*dlx - rx*dlz);
double r_cross_dr_z = ry*dlx - rx*dly;

double abs_rk = sqrt(rx*rx + ry*ry + rz*rz);

double s = 1/(pow(1+(alpha*(sigma[m][n]*sigma[m][n] + sigma[j][k]*sigma[j][k])/
        (2*abs_rk*abs_rk)),1.5));

    if (0.5*(z_n[j+1][k] - z_n[j][k]) + z_n[j][k] <= 0){
    gam_eq = 0.0;
    }
    else {
    gam_eq = gamma[j][k];
    }

double u_ind_dummy_x = (-gam_eq/(4.0*pi))*r_cross_dr_x*s/(pow(abs_rk,3));
double u_ind_dummy_y = (-gam_eq/(4.0*pi))*r_cross_dr_y*s/(pow(abs_rk,3));
double u_ind_dummy_z = (-gam_eq/(4.0*pi))*r_cross_dr_z*s/(pow(abs_rk,3));

    if (j == 0 && k == 0) {

    u_induced_x = u_ind_dummy_x;
    u_induced_y = u_ind_dummy_y;
    u_induced_z = u_ind_dummy_z;
    }

    else {

    u_induced_x = u_induced_x + u_ind_dummy_x;
    u_induced_y = u_induced_y + u_ind_dummy_y;
    u_induced_z = u_induced_z + u_ind_dummy_z;
    }

        }
        }
      if (z_n[m][n] < 0){
        u_induced_total_x[m][n] = 0;
        u_induced_total_y[m][n] = 0;
        u_induced_total_z[m][n] = 0;
        }

      else {
        u_induced_total_x[m][n] = u_induced_total_x[m][n] + u_induced_x;
        u_induced_total_y[m][n] = u_induced_total_y[m][n] + u_induced_y;
        u_induced_total_z[m][n] = u_induced_total_z[m][n] + u_induced_z;
        }
      }
```

```
        }

        //calculate induced velocities on and from radial spoke calculation
        r_calc_ind();

        //calculate induced velocity for all nodes, based on symmetry
        sym_calc();
        r_sym_calc();
        u_update();
}

void r_calc_ind()
{
        u_induced_x = 0;
        u_induced_y = 0;
        u_induced_z = 0;

        r_on_fil  = 0;
           for (int n = 0; n <= r_n_fil-1; n++){
                if (r_z_n[0][n] >= 0) {
                    r_on_fil = r_on_fil + 1 ;
                }
            }

           if (r_on_fil >= r_n_fil){
                r_on_fil = r_n_fil;
            }

       //calculate velocity induced on vortex tube filaments by spokes
        int n;
        for (int j1 = 0; j1 <= n_rad; j1++){

        if (j1==0){n = 0;}
        else if (j1==1){n = 1;}
        else if (j1 > 1){n = r_fil[j1-2]+ n;}

          for (int m = 0; m <= on_node[n]-1; m++){

            for (int k = 0; k <= r_on_fil-1; k++){
              for (int j = 0; j <= r_max_node-2; j++){

double gam_eq;

double dlx = r_x_n[j+1][k]-r_x_n[j][k];
double dly = r_y_n[j+1][k]-r_y_n[j][k];
double dlz = r_z_n[j+1][k]-r_z_n[j][k];

double rx = x_n[m][n] - (0.5*(r_x_n[j+1][k] - r_x_n[j][k]) + r_x_n[j][k]);
double ry = y_n[m][n] - (0.5*(r_y_n[j+1][k] - r_y_n[j][k]) + r_y_n[j][k]);
double rz = z_n[m][n] - (0.5*(r_z_n[j+1][k] - r_z_n[j][k]) + r_z_n[j][k]);

double r_cross_dr_x = rz*dly - ry*dlz;
double r_cross_dr_y = -(rz*dlx - rx*dlz);
double r_cross_dr_z = ry*dlx - rx*dly;
```

```
double abs_rk = sqrt(rx*rx + ry*ry + rz*rz);

double s = 1/(pow(1+(alpha*(sigma[m][n]*sigma[m][n] + r_sigma[j][k]*
      r_sigma[j][k])/(2*abs_rk*abs_rk)),1.5));

    if (0.5*(r_z_n[j+1][k] - r_z_n[j][k]) + r_z_n[j][k] <= 0){
    gam_eq = 0.0;
    }
    else {
    gam_eq = -r_gamma[j][k];
    }

double u_ind_dummy_x = (-gam_eq/(4.0*pi))*r_cross_dr_x*s/(pow(abs_rk,3));
double u_ind_dummy_y = (-gam_eq/(4.0*pi))*r_cross_dr_y*s/(pow(abs_rk,3));
double u_ind_dummy_z = (-gam_eq/(4.0*pi))*r_cross_dr_z*s/(pow(abs_rk,3));

    if (j == 0 && k == 0) {

    u_induced_x = u_ind_dummy_x;
    u_induced_y = u_ind_dummy_y;
    u_induced_z = u_ind_dummy_z;
    }

    else {

    u_induced_x = u_induced_x + u_ind_dummy_x;
    u_induced_y = u_induced_y + u_ind_dummy_y;
    u_induced_z = u_induced_z + u_ind_dummy_z;
    }

        }
        }
      if (z_n[m][n] < 0){
        u_induced_total_x[m][n] = 0;
        u_induced_total_y[m][n] = 0;
        u_induced_total_z[m][n] = 0;
        }

      else {
        u_induced_total_x[m][n] = u_induced_total_x[m][n] + u_induced_x;
        u_induced_total_y[m][n] = u_induced_total_y[m][n] + u_induced_y;
        u_induced_total_z[m][n] = u_induced_total_z[m][n] + u_induced_z;
        }
     }
     }

//calculate velocity induced on spokes by vortex tube filaments

    for (int n = 0; n <= r_n_fil-1; n++){
      for (int m = 0; m <= r_max_node-1; m++){
        r_u_induced_total_x[m][n] = 0;
        r_u_induced_total_y[m][n] = 0;
        r_u_induced_total_z[m][n] = 0;
```

```
      }
    }

  u_induced_x = 0;
  u_induced_y = 0;
  u_induced_z = 0;


  for (int j1 = 0; j1 <= r_on_fil/n_spokes-1; j1++){
  n = n_spokes*j1;

    for (int m = 0; m <= r_max_node-1; m++){

      for (int k = 0; k <= n_fil-1; k++){
        for (int j = 0; j <= on_node[k]-2; j++){

double gam_eq;

double dlx = x_n[j+1][k]-x_n[j][k];
double dly = y_n[j+1][k]-y_n[j][k];
double dlz = z_n[j+1][k]-z_n[j][k];

double rx = r_x_n[m][n] - (0.5*(x_n[j+1][k] - x_n[j][k]) + x_n[j][k]);
double ry = r_y_n[m][n] - (0.5*(y_n[j+1][k] - y_n[j][k]) + y_n[j][k]);
double rz = r_z_n[m][n] - (0.5*(z_n[j+1][k] - z_n[j][k]) + z_n[j][k]);

double r_cross_dr_x = rz*dly - ry*dlz;
double r_cross_dr_y = -(rz*dlx - rx*dlz);
double r_cross_dr_z = ry*dlx - rx*dly;

double abs_rk = sqrt(rx*rx + ry*ry + rz*rz);

double s = 1/(pow(1+(alpha*(r_sigma[m][n]*r_sigma[m][n] +
      sigma[j][k]*sigma[j][k])/(2*abs_rk*abs_rk)),1.5));

    if (0.5*(z_n[j+1][k] - z_n[j][k]) + z_n[j][k] <= 0){
    gam_eq = 0.0;
    }
    else {
    gam_eq = gamma[j][k];
    }

double u_ind_dummy_x = (-gam_eq/(4.0*pi))*r_cross_dr_x*s/(pow(abs_rk,3));
double u_ind_dummy_y = (-gam_eq/(4.0*pi))*r_cross_dr_y*s/(pow(abs_rk,3));
double u_ind_dummy_z = (-gam_eq/(4.0*pi))*r_cross_dr_z*s/(pow(abs_rk,3));

    if (j == 0 && k == 0) {

    u_induced_x = u_ind_dummy_x;
    u_induced_y = u_ind_dummy_y;
    u_induced_z = u_ind_dummy_z;
    }

    else {
```

```
        u_induced_x = u_induced_x + u_ind_dummy_x;
        u_induced_y = u_induced_y + u_ind_dummy_y;
        u_induced_z = u_induced_z + u_ind_dummy_z;
       }


        }
        }
     if (r_z_n[m][n] < 0){
       r_u_induced_total_x[m][n] = 0;
       r_u_induced_total_y[m][n] = 0;
       r_u_induced_total_z[m][n] = 0;
        }

     else {
       r_u_induced_total_x[m][n] = r_u_induced_total_x[m][n]+u_induced_x;
       r_u_induced_total_y[m][n] = r_u_induced_total_y[m][n]+u_induced_y;
       r_u_induced_total_z[m][n] = r_u_induced_total_z[m][n]+u_induced_z;
        }
      }
     }
}

//----------------Function init_ind----------------------------------------
// Initialize induced velocity calculations
//-------------------------------------------------------------------------
void init_ind()
{
     for (int n = 0; n <= n_fil-1; n++){
            on_node[n] = 0;
       for (int m = 0; m <= max_node-1; m++){


         u_induced_total_x[m][n] = 0;
         u_induced_total_y[m][n] = 0;
         u_induced_total_z[m][n] = 0;

            if (z_n[m][n] >= 0) {
               on_node[n] = on_node[n] + 1;
            }
         }

         if (on_node[n] >= max_node){
            on_node[n] = max_node;
         }
      }
}

//----------------Function init_ind----------------------------------------
// Update node positions and filament parameters
//-------------------------------------------------------------------------
void u_update(){

     double **seg_length = new double *[max_node];
```

```
    for (int i = 0;i<max_node;i++){seg_length[i]= new double [n_fil];}

        for (int n = 0; n <= n_fil-1; n++){
        for (int m = 0; m <= max_node-1; m++){
        x_n[m][n] = x_n[m][n] + u_induced_total_x[m][n]*dt;
        y_n[m][n] = y_n[m][n] + u_induced_total_y[m][n]*dt;
        z_n[m][n] = z_n[m][n] + (u_induced_total_z[m][n] + U_instant[t_index])*dt;
        }
        }
        for (int n = 0; n <= n_fil-1; n++){
        for (int m = 0; m <= max_node-2; m++){
          seg_length[m][n] = sqrt((x_n[m+1][n]-x_n[m][n])*
          (x_n[m+1][n]-x_n[m][n])+(y_n[m+1][n]-y_n[m][n])*(y_n[m+1][n]-
          y_n[m][n])+(z_n[m+1][n]-z_n[m][n])*(z_n[m+1][n]-z_n[m][n]));

          sigma[m][n] = sqrt((core_con[n]/seg_length[m][n]));
        }
        }

        //update radial spokes

    r_seg_length = new double *[r_max_node];
    for (int i = 0;i<r_max_node;i++){r_seg_length[i]= new double [r_n_fil];}

        for (int n = 0; n <= r_n_fil-1; n++){
        for (int m = 0; m <= r_max_node-1; m++){

        r_x_n[m][n] = r_x_n[m][n] + r_u_induced_total_x[m][n]*dt;
        r_y_n[m][n] = r_y_n[m][n] + r_u_induced_total_y[m][n]*dt;
        r_z_n[m][n] = r_z_n[m][n] + (r_u_induced_total_z[m][n] + U_instant[t_index])*dt;
        }
        }

        for (int n = 0; n <= r_n_fil-1; n++){
        for (int m = 0; m <= r_max_node-2; m++){
          r_seg_length[m][n] = sqrt((r_x_n[m+1][n]-r_x_n[m][n])*
          (r_x_n[m+1][n]-r_x_n[m][n])+(r_y_n[m+1][n]-r_y_n[m][n])*
          (r_y_n[m+1][n]-r_y_n[m][n])+(r_z_n[m+1][n]-r_z_n[m][n])*
          (r_z_n[m+1][n]-r_z_n[m][n]));

          r_sigma[m][n] = sqrt((r_core_con[m][n]/r_seg_length[m][n]));
        }
        }


        //cout <<"Umax: "<<Umax<<" Umin: "<<Umin<<endl;
delete[] seg_length;
}

void sym_calc(){

    int n;
    for (int j1 = 1; j1 <= n_rad; j1++){
```

```
    if (j1==1){n = 1;}
    else if (j1 > 1){n = r_fil[j1-2]+ n;}

      for (int k = n; k <= n+r_fil[j1-1]-1; k++){
      for (int m = 0; m <= on_node[k]-1; m++){

      double u_rad = (x_n[m][n]/sqrt(x_n[m][n]*x_n[m][n]+y_n[m][n]*
      y_n[m][n]))*u_induced_total_x[m][n]+(y_n[m][n]/sqrt(x_n[m][n]*
      x_n[m][n]+y_n[m][n]*y_n[m][n]))*u_induced_total_y[m][n];
      double u_theta = -(y_n[m][n]/sqrt(x_n[m][n]*x_n[m][n]+y_n[m][n]*
      y_n[m][n]))*u_induced_total_x[m][n]+(x_n[m][n]/sqrt(x_n[m][n]*
      x_n[m][n]+y_n[m][n]*y_n[m][n]))*u_induced_total_y[m][n];
      double u_ax = u_induced_total_z[m][n];

      u_induced_total_x[m][k]=  (x_n[m][k]/sqrt(x_n[m][k]*x_n[m][k]+
      y_n[m][k]*y_n[m][k]))*(u_rad)- (y_n[m][k]/sqrt(x_n[m][k]*
      x_n[m][k]+y_n[m][k]*y_n[m][k]))*(u_theta);
      u_induced_total_y[m][k]=  (y_n[m][k]/sqrt(x_n[m][k]*x_n[m][k]+
      y_n[m][k]*y_n[m][k]))*(u_rad)+(x_n[m][k]/sqrt(x_n[m][k]*
      x_n[m][k]+y_n[m][k]*y_n[m][k]))*(u_theta);
      u_induced_total_z[m][k]=  u_ax;
      }
      }
    }
    }

void r_sym_calc(){

    int n;
    for (int j1 = 0; j1 <= r_on_fil/n_spokes-1; j1++){
    n = n_spokes*j1;

      for (int k = n; k <= n+n_spokes-1; k++){
      for (int m = 0; m <= r_max_node-1; m++){

      double u_rad = (r_x_n[m][n]/sqrt(r_x_n[m][n]*r_x_n[m][n]+r_y_n[m][n]*
      r_y_n[m][n]))*r_u_induced_total_x[m][n]+(r_y_n[m][n]/
      sqrt(r_x_n[m][n]*r_x_n[m][n]+r_y_n[m][n]*r_y_n[m][n]))*
      r_u_induced_total_y[m][n];
      double u_theta = -(r_y_n[m][n]/sqrt(r_x_n[m][n]*r_x_n[m][n]+
      r_y_n[m][n]*r_y_n[m][n]))*r_u_induced_total_x[m][n]+(r_x_n[m][n]/
      sqrt(r_x_n[m][n]*r_x_n[m][n]+r_y_n[m][n]*r_y_n[m][n]))*
      r_u_induced_total_y[m][n];
      double u_ax = r_u_induced_total_z[m][n];

      r_u_induced_total_x[m][k]=  (r_x_n[m][k]/sqrt(r_x_n[m][k]*
      r_x_n[m][k]+r_y_n[m][k]*r_y_n[m][k]))*(u_rad)-(r_y_n[m][k]/
      sqrt(r_x_n[m][k]*r_x_n[m][k]+r_y_n[m][k]*r_y_n[m][k]))*(u_theta);
      r_u_induced_total_y[m][k]=  (r_y_n[m][k]/sqrt(r_x_n[m][k]*
      r_x_n[m][k]+r_y_n[m][k]*r_y_n[m][k]))*(u_rad)+(r_x_n[m][k]/
      sqrt(r_x_n[m][k]*r_x_n[m][k]+r_y_n[m][k]*r_y_n[m][k]))*(u_theta);
      r_u_induced_total_z[m][k]=  u_ax;
      }
      }
```

```
        }
        }
```

D.2   Vlinec_rad_spoke_wfj Input Parameter Code

```
//----------------------------------------------------------------------------
// This is the input file for vlinec.exe  Do not modify the structure.
// To change an input value, just replace the existing value
// Do not delete the dollar sign symbols below
//----------------------------------------------------------------------------
$
1          //Simulation initial condition case, see init_incase_rad_spoke.cpp
2.01       //t_final. . . final simulation time
5          //U_inf. . .freestream velocity
0.1        //dz. . . initial axial separation between vortex filament nodes
0.01       //dt. . .simulation time step
101        //max_node. . maxnumber of nodes in a filament (excluding radial spokes)
16         //numer of filaments at a given radius
9          //number of radii (excluding centerline)
0          //t_out_start. . . t_index output starts
1          //out_skip. . . number of iterations before writing data to file
0.42       //r_tube0. . . initial radial location of an axial vortex filament
0.36       //r_tube1
0.3        //r_tube2
0.24       //r_tube3
0.18       //r_tube4
0.12       //r_tube5
0.08       //r_tube6
0.06       //r_tube7
0.03       //r_tube8
0.0        //r_tube9
0.0        //r_tube10
0.0        //r_tube11
0.0        //r_tube12
0.12       //sigma_init. . . initial vortex filament radius
20.0       //Cmax. . . final value of total circulation in vortex tube
-0.01      //start_C_inc. . . axial location where linear C increase starts (assumes minor     movement)
-0.51      //stop_C_inc . . . axial location where linear C increase ends
            (avg vel of 2.5 * .2)
0.0        //C_min. . . intial value of total circulation in vortex tube
0.413      //alpha. . . parameter defining velocity near filament center
0.0        //z_on. . . axial location where self induction starts
0.0        //z_init. . . sets overvall initial location of vortex tube
0.0        //x_init. . . sets overvall initial location of vortex tube
0.0        //y_init. . . sets overvall initial location of vortex tube
```